

CFD ANALYSIS & MODELLING OF OFFSHORE STRUCTURES

By

Ahmet ÖZBAŞ

Mustafa EREN

Graduate Program in Mechanical Engineering
Marmara University

2012

ACKNOWLEDGEMENTS

We would like to thank to Assist. Prof. Mustafa YILMAZ for trusting and guiding me till the end of my study. We would like to thank to Expert Yalçın YÜKSELENDAĞ for commenting on my study and helping me when We got into trouble. Thank you for your continuing support till the last day of our study.

Further, I would like to thank my friends Ahmet ÖNGEL and Çağlar ÇAVUŞ for their help, the support and for the fun times during MSc. I wish you all success, luck and happiness.

Abstract

First of all; this report includes flow analysis of offshore structures which include velocity, pressure and wall shear stresses. We read several articles and appraisal and we try to make it utilize.

In this assay, the flow analysis of fixed type of offshore platform is looked into. To this end, three-leg fixed type rig has been chosen and it is analysed with aeraulic and fluid flow forces respectively. Wind loads on offshore structures can be evaluated using modelling approaches adopted for land-based structures but for conditions pertaining to ocean environments. The fluctuating component of the wind velocity is random in nature and is simulated for a given wind velocity. To calculate the wind forces (along the height of the tower), the mean wind velocity along the height is calculated according to the following CFD program that is Star-CCM+6.06.011.

We considered our summary consist of four section, in which is the first section historical development of offshore platforms, some of the previous studies on offshore platforms and differnt types of offshore platforms are presented. Regarding to wave, air and current flow effects.

In the second section, utilizing equations and models which is used by CFD program.

In thirth section, setting up and getting results from CFD program

In fourth section, by using the getting results from CFD program, we compare between two simulations that are symmetry and full models.

Table of Contents

ACKNOWLEDGEMENTS	1
Abstract	3
1. Introduction:.....	6
2. History of Oil-Rigs:	7
3. Types:	10
3.1. Fixed platform:	10
3.2. Compliant Tower(CT)	11
3.3. Semi-submersible.....	12
3.4. Jackup rig	14
3.5. GBS	15
3.6. ETLP.....	16
4. Typical design	18
5. Material Properties ofThe Platform	20
6. MODELLING EQUATIONS:	20
6.1. Time	20
6.1.1. Implicit unsteady:.....	20
6.2. Multiphase Flow Model	21
6.3. Viscous Regima:.....	27
6.3.1. Turbulent:	27
6.4. Reynold-Averaged Turbulance Model.....	29
6.4.1. Standard k-epsilon model	31
6.4.2. Realisable k-epsilon model.....	32
7. CFD Results	34
7.1. Symetry plane:	36
7.1.1. Velocity results.....	36
7.1.2. Pressure Results.....	46
7.1.3. Wall shear stresses.....	56
7.2. Full Model.....	66
7.2.1. Velocity	66
7.2.2. Pressure	76
7.2.3. Wall Shear Stresses:	86
8. Comparing Results	97
8.1. Velocity	97

8.2. Pressure.....	98
8.3. Wall Shear Stresses	99
9. Conclusion.....	100
10. REFERENCES	101

1. Introduction:

An oil platform, also referred to as an offshore platform or, somewhat incorrectly, oil rig, is a large structure with facilities to drill wells, to extract and process oil and natural gas, and to temporarily store product until it can be brought to shore for refining and marketing. In many cases, the platform contains facilities to house the workforce as well.

Depending on the circumstances, the platform may be fixed to the ocean floor, may consist of an artificial island, or may float.

Remote subsea wells may also be connected to a platform by flow lines and by umbilical connections; these subsea solutions may consist of single wells or of a manifold centre for multiple wells.

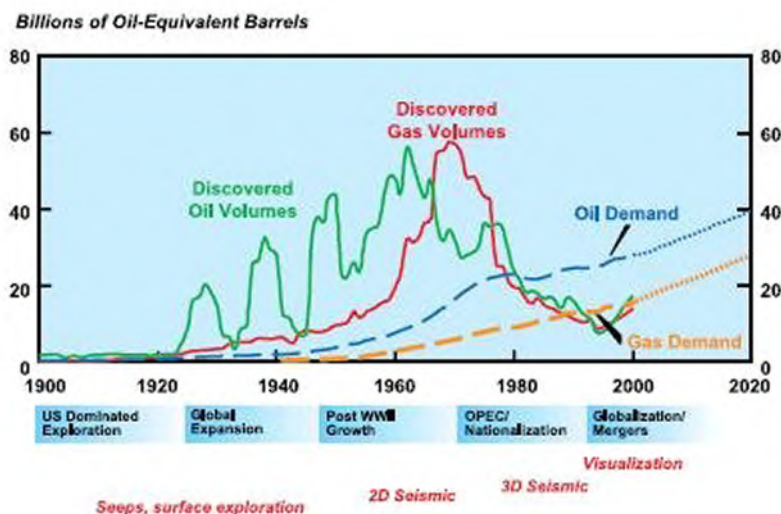


Figure 1. Change in Supply and Demand over Time by Longwell (2002)

As seen in figure 1, the demand for both gas and oil started to increase in the early 1950's and by the 1980's the capacity of the oil and gas reserves being discovered in the world started to decrease. In order to bridge the gap between growing demand and reducing supply, oil companies began to focus on finding new reserves and getting the maximum output from previously discovered reserves which are generally found offshore. As previously stated, the

offshore industry is a smaller market than the construction industry in terms of the number of planned projects and delivered projects per year, which makes the market more competitive for the offshore petroleum platform fabrication companies.

2. History of Oil-Rigs:

Around 1891 the first submerged oil wells were drilled from platforms built on piles in the fresh waters of the Grand Lake St. Marys (a.k.a. Mercer County Reservoir) in Ohio. The wide but shallow reservoir was built from 1837 to 1845 to provide water to the Miami and Erie Canal.



Figure2: Photograph: courtesy of Joyce L. Alig. From "Our Post Card Past; Grand Lake St. Marys Ohio," Passport to History Series, Book VIII, Mercer County Historical Society, Inc., Celina, Ohio, 2001

Around 1896 the first submerged oil wells in salt water were drilled in the portion of the Summerland field extending under the Santa Barbara Channel in California. The wells were drilled from piers extending from land out into the channel.

Other notable early submerged drilling activities occurred on the Canadian side of Lake Erie in the 1900s and Caddo Lake in Louisiana in the 1910s. Shortly thereafter, wells were drilled in tidal zones along the Gulf Coast of Texas and Louisiana. The Goose Creek field near Baytown, Texas is one such example. In the 1920s drilling was done from concrete platforms in Lake Maracaibo, Venezuela.

The oldest subsea well recorded in Infield's offshore database is the Bibi Eibat well which came on stream in 1923 in Azerbaijan. Landfill was used to raise shallow portions of the Caspian Sea.



Figure3:Bibi Eibat by Konstantin Bogayevsky

In the early 1930s the Texas Company developed the first mobile steel barges for drilling in the brackish coastal areas of the gulf.

In 1937 Pure Oil Company (now part of Chevron Corporation) and its partner Superior Oil Company (now part of ExxonMobil Corporation) used a fixed platform to develop a field in 14 feet (4.3 m) of water, one mile (1.6 km) offshore of Calcasieu Parish, Louisiana.

In 1946, Magnolia Petroleum Company (now part of ExxonMobil) erected a drilling platform in 18 ft (5.5 m) of water, 18 miles off the coast of St. Mary Parish, Louisiana.

In early 1947 Superior Oil erected a drilling/production platform in 20 ft (6.1 m) of water some 18 miles off Vermilion Parish, Louisiana. But it was Kerr-McGee Oil Industries (now Anadarko Petroleum Corporation), as operator for partners Phillips Petroleum (ConocoPhillips) and Stanolind Oil & Gas (BP), that completed its historic Ship Shoal Block 32 well in October 1947, months before Superior actually drilled a discovery from their Vermilion platform farther offshore. In any case, that made Kerr-McGee's well the first oil discovery drilled out of sight of land.



Figure4: Ship Shoal Block October 1947

The Thames Sea Forts of World War II are considered the direct predecessors of modern offshore platforms. Having been pre-constructed in a very short time, they were then floated to their location and placed on the shallow bottom of the Thames estuary.

The Gulf of Mexico	400
Asia	950
Middle East	700
The North Sea and Atlantic	490
The WestCoast ofAfrica	380
North America	340

Table1:Number of the offshore rigs by regions

3. Types:

3.1. Fixed platform:

A fixed platform is a type of offshore platform used for the production of oil or gas. These platforms are built on concrete and/or steel legs anchored directly onto the seabed, supporting a deck with space for drilling rigs, production facilities and crew quarters. Such platforms are, by virtue of their immobility, designed for very long term use (for instance the Hibernia platform). Various types of structure are used, steel jacket, concrete caisson, floating steel and even floating concrete. Steel jackets are vertical sections made of tubular steel members, and are usually piled into the seabed. Concrete caisson structures, pioneered by the Condeep concept, often have in-built oil storage in tanks below the sea surface and these tanks were often used as a flotation capability, allowing them to be built close to shore (Norwegianfjords and Scottishfirths are popular because they are sheltered and deep enough) and then floated to their final position where they are sunk to the seabed. Fixed platforms are economically feasible for installation in water depths up to about 1,700 feet (520 m).



Figure5: schematic representation of the fixed platform

3.2. Compliant Tower(CT)

A compliant tower (CT) is a fixed rig structure normally used for the offshore production of oil or gas. The rig consists of narrow, flexible (compliant) towers and a piled foundation supporting a conventional deck for drilling and production operations. Compliant towers are designed to sustain significant lateral deflections and forces, and are typically used in water depths ranging from 1,500 and 3,000 feet (450 and 900 m). At present the deepest is the TexacoPetronius tower in waters 623m deep.

With the use of flex elements such as flex legs or axial tubes, resonance is reduced and wave forces are de-amplified. This type of rig structure can be configured to adapt to existing fabrication and installation equipment. Compared with floating systems, such as Tension-leg

platforms and SPARs, the production risers are conventional and are subjected to less structural demands and flexing.^[1] This flexibility allows it to operate in much deeper water, as it can 'absorb' much of the pressure exerted on it by the wind and sea. Despite its flexibility, the compliant tower system is strong enough to withstand hurricane conditions.

The first tower emerged in the early 1980s with the installation of Exxon's Lena oil platform.

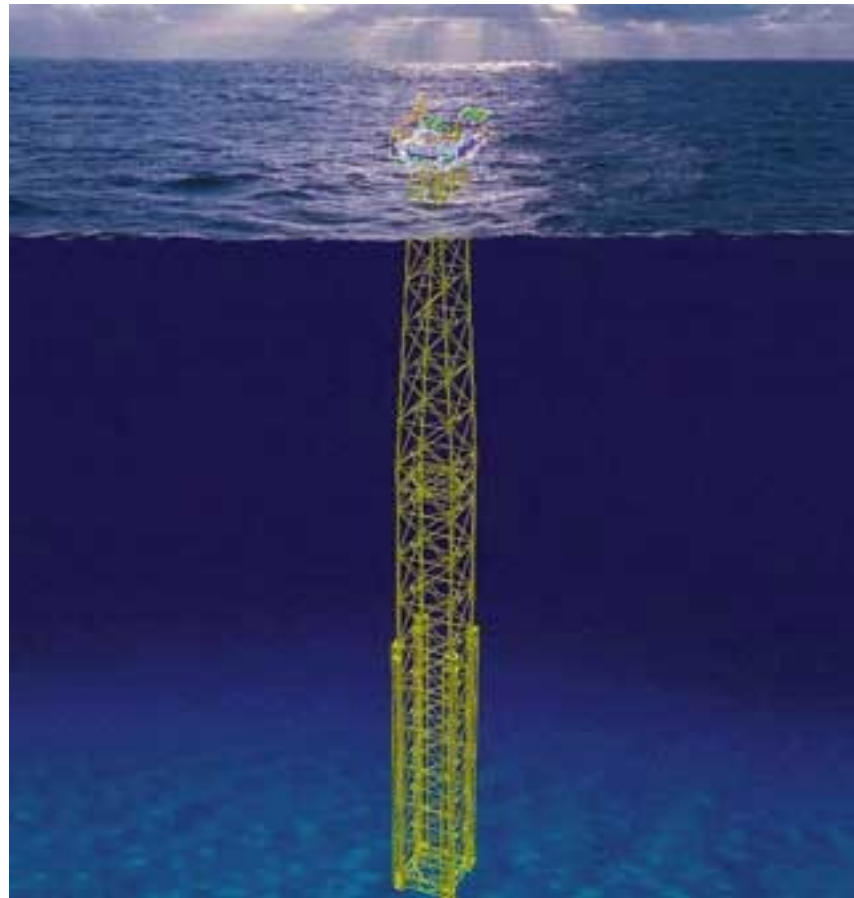


Figure6: CT

3.3. Semi-submersible

A semi-submersible is a specialised marine vessel with good stability and seakeeping characteristics. The semi-submersible vessel design is commonly used in a number of specific offshore roles such as for offshore drilling rigs, safety vessels, oil production platforms and heavy lift cranes.

The terms semisubmersible, semi-sub or just *semi* are also generally used for this vessel design.

Offshore drilling in water depth greater than around 120 meters requires that operations be carried out from a floating vessel, as fixed structures are not practical. Initially in the early 1950s monohull ships were used like CUSS I, but these were found to have significant heave, pitch and yaw motions in large waves, and the industry needed more stable drilling platforms.

A semi-submersible obtains its buoyancy from ballasted, watertight pontoons located below the ocean surface and wave action. The operating deck can be located high above the sea level due to the good stability of the concept, and therefore the operating deck is kept well away from the waves. Structural columns connect the pontoons and operating deck.

With its hull structure submerged at a deep draft, the semi-submersible is less affected by wave loadings than a normal ship. With a small water-plane area, however, the semi-submersible is sensitive to load changes, and therefore must be carefully trimmed to maintain stability. Unlike a submarine or submersible, during normal operations, a semi-submersible vessel is never entirely underwater.

A semi-submersible vessel is able to transform from a deep to a shallow draft by deballasting (removing ballast water from the hull), and thereby become a surface vessel. The heavy lift vessels use this capability to submerge the majority of their structure, locate beneath another floating vessel, and then deballast to pick up the other vessel as a cargo.



Courtesy of Husky

Figure 7: The West Hercules deepwater semi-submersible drilling rig can run parallel drilling operations and is designed with a dynamic positioning system. It can operate in waters up to 3,000m deep.

3.4. Jackup rig

A jackup is a floating barge fitted with long support legs that can be raised or lowered. The jackup is maneuvered (self-propelled or by towing) into location with its legs up and the hull floating on the water. Upon arrival at the work location, the legs are jacked down onto the seafloor. Then "preloading" takes place, where the weight of the barge and additional ballast water are used to drive the legs securely into the seabottom so they will not penetrate further while operations are carried out. After preloading, the jacking system is used to raise the entire barge above the water to a predetermined height or "air gap", so that wave, tidal and current loading acts only on the relatively slender legs and not on the barge hull.

Modern jacking systems use a rack and pinion gear arrangement where the pinion gears are driven by hydraulic or electric motors and the rack is affixed to the legs.

Jackup rigs can only be placed in relatively shallow waters, generally less than 400 feet (120 m) of water. However, a specialized class of jackup rigs known as premium or ultra-premium jackups are known to have operational capability in water depths ranging from 500 to 625 feet.



Figure8: The Galaxy II jack-up rig, prior to deployment on the Sable field

3.5. GBS

Gravity-based structure (GBS) is a support structure held in place by gravity. A common application for a GBS is an offshore oil platform. These structures are often constructed in fjords since their protected area and sufficient depth are very desirable for construction. A GBS intended for use as an offshore oil platform is constructed of steel reinforced concrete, often with tanks or cells which can be used to control the buoyancy of the finished GBS. When completed, a GBS is towed to its intended location and sunk. The platform structure which a GBS supports is called the topsides.

Gravity-based structures are also widely used for offshore wind power plants. By the end of 2010, 14 of the world's offshore wind farms were supported by Gravity-based structures. The GBS are suited for water depths up to 20 meters. The deepest registered offshore wind farm with Gravity-based structures is Thornton Bank 1, Belgium, with a depth up to 27.5 meters. However, as offshore wind power plants are growing in size and moving towards deeper waters, the GBS is not considered competitive in comparison with other support structures.



Figure9: Hibernia a concrete gravity-based structure built specifically to develop the Hibernia field off the coast of Newfoundland, Canada. 1997

3.6. ETLP

A Tension-leg platform or Extended Tension Leg Platform (ETLP) is a vertically moored floating structure normally used for the offshore production of oil or gas, and is particularly suited for water depths greater than 300 metres (about 1000 ft) and less than 1500 meters (about 4900 ft). Use of tension-leg platforms has also been proposed for wind turbines.

The platform is permanently moored by means of tethers or tendons grouped at each of the structure's corners. A group of tethers is called a tension leg. A feature of the design of the tethers is that they have relatively high axial stiffness (low elasticity), such that virtually all vertical motion of the platform is eliminated. This allows the platform to have the production wellheads on deck (connected directly to the subsea wells by rigid risers), instead of on the

seafloor. This allows a simpler well completion and gives better control over the production from the oil or gas reservoir, and easier access for downhole intervention operations.

TLP's have been in use since the early 1980s. The first Tension Leg Platform was built for Conoco's Hutton field in the North Sea in the early 1980s. The hull was built in the dry-dock at Highland Fabricator's Nigg yard in the north of Scotland, with the deck section built nearby at McDermott's yard at Ardersier. The two parts were mated in the Moray Firth in 1984.

Larger TLP's will normally have a full drilling rig on the platform with which to drill and intervene on the wells. The smaller TLPs may have a workover rig, or in a few cases no production wellheads located on the platform at all.

The deepest (E)TLPs measured from the sea floor to the surface are:

1,425 m Magnolia ETLP. Its total height is some 1,500 m.

1,300 m Marco Polo TLP

1,300 m Neptune TLP

1,177 m Kizomba A TLP

1,200 m Ursa TLP. Its height above surface is 148 m making a total height of 1,306 m

1,020 m Allegheny TLP

1,000 m W. Seno A TLP

The steel jacket type platform on a pile foundation is by far the most common kind of offshore structure and they exist worldwide. The "substructure" or "jacket" is fabricated from steel welded pipes and is pinned to the sea floor with steel piles, which are driven through piles guides on the outer members of the jacket.

The piles are thick steel pipes of 1 to 2 metres diameter and can penetrate as much as 100 m into the sea bed. The jacket can weigh up to 20,000 tonnes.

To ensure that the installation will last for the required service life, maintenance must be carried out including the cathodic protection used to prevent corrosion.



Figure 10: Mars Tensioned-Leg Platform (TLP), Image by Garve Scott-Lodge

4. Typical design

Many parameters influence the design of the jacket, such as required strength, fatigue, load and life cycle. The pile design results in a balanced combination of diameter, penetration, pile wall thickness, and spacing.

The design of the pile is very important in the design of the jacket structure itself and the cost of pile foundation and installation could be as much as 40 % of the total cost of the platform structure. For example, the typical design requirements for a steel jacket of 150 m would be as described below.

At the seabed the dimensions of the structure are 70 x 65 m and at the top 56 x 30 m (the top is about 15 m above sea level).

Such a structure weights about 18,500 tonnes and would support topsides of up to 21,000 tonnes. The jacket can resist forces of up to 50 MN in compression and 10 MN in tension as well as having large resistance to lateral loads.

Maximum design forces for steel jacket platform may be as follow:

Vertical load: around 50 MN

Horizontal load: around 5 MN

Oversetting moment: around 10 GN.m

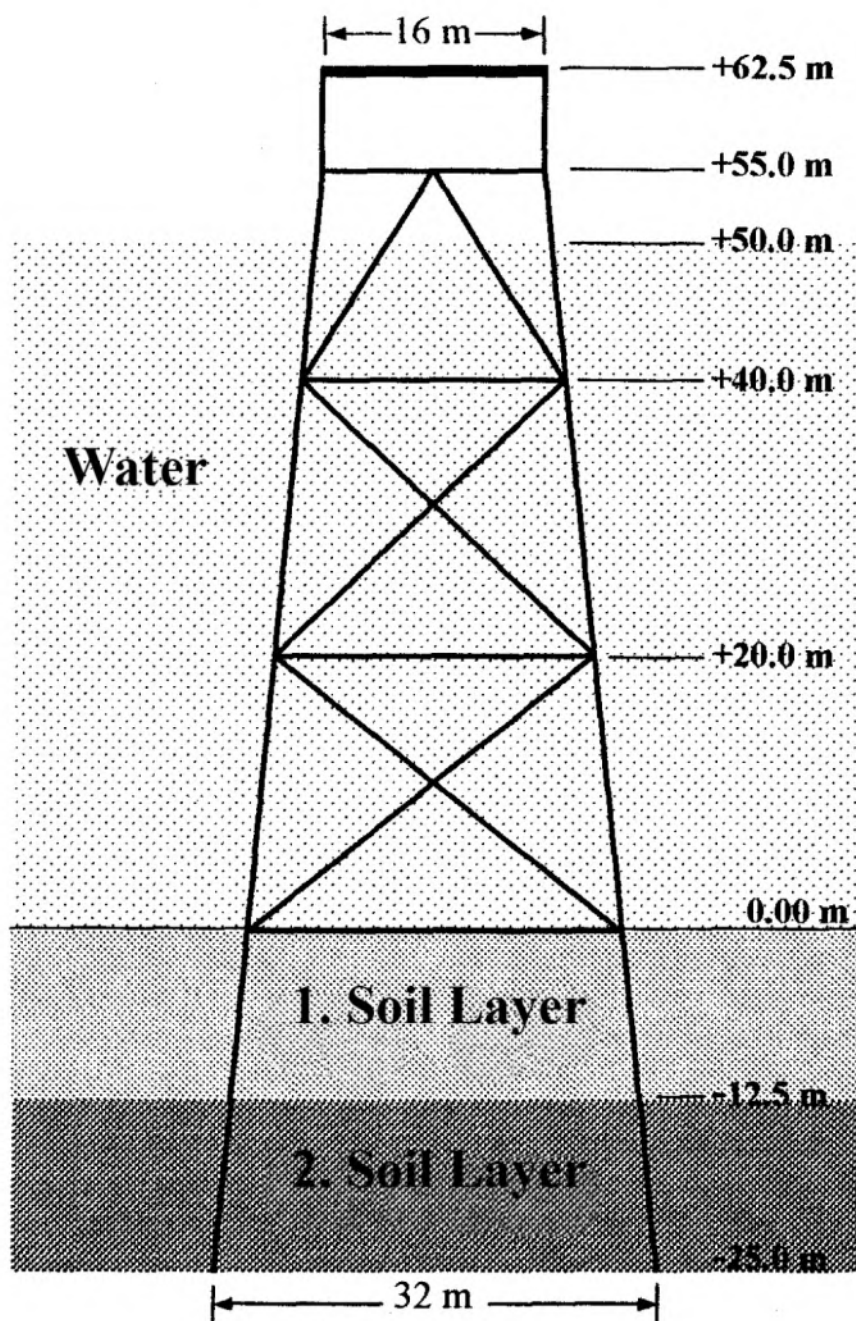


Figure11: Typical Jacket Structure

5. Material Properties of The Platform

Jacket-type platform consists of steel girders and superstructure elements that make up part of the deck weighs ten thousand tons. This weight jacket in the form of mass equal to the highest level seen from the point of the four corners. As can be seen in Figure 12, two layers of the platform sat the ground are occurring and average values for the soft sandy soil. Modulus of elasticity of all the elements that make up Platform $20.5 * 10^10 \text{ N} / \text{m}^2$, and Poisson's ratio as 0.25 taken into account.

6. MODELLING EQUATIONS:

At the begining of simulation we have to select and examine some equations, constant and turbulence modelling, many equations familiar to you that can be modelled.

6.1. Time

6.1.1. Implicit unsteady:

The implicit unsteady approach is appropriate if the time scales of the phenomena of interest are of the same order as the convection and/or diffusion processes (for example, vortex shedding) or are due to some relatively low frequency external excitation (for example, time-varying boundary conditions or boundary motion)

In the implicit unsteady approach each physical time-step involves some number of inner iterations to converge the solution for that given instant of time. These inner iterations may be accomplished using the same implicit integration or explicit integration schemes used for steady analysis. The physical time-step size used in the outer loop is specified by you, whereas the inner iterations are marched by the integration scheme using optimal local steps as determined by the Courant number.

With implicit unsteady approach you are required to set the physical time-step size, the Courant number, and the number of inner iterations to be performed at each physical time-step.

The physical time-step size will generally be governed by the transient phenomena being modeled. The time-step should at least satisfy the Nyquist sampling criterion; more than two time-steps per period are required.

In general the same Courant number setting guidelines as for the steady-state integration schemes apply.

The number of inner iterations per physical time-step is harder to quantify. Generally, this will need to be determined experimentally. You should select a certain number of inner iterations (the default is 20) and then see if the results are affected by increasing or decreasing this number.

Smaller physical time-steps generally mean the solution is changing less from one time-step to the next, so that fewer inner iterations are required. There will be an optimal balance of time-step size and number of inner iterations for a given problem and desired transient accuracy.

6.2. Multiphase Flow Model

The general procedure to relate the MFM to the MMM is to sum each equation over all of the phases. The introductions of the mass-averaged density and velocity, as well as the relative mobility, are given where appropriate. The MMM was initially developed by Wang and Cheng (1996) and was applied to model multiphase flow in fuel cells.

The continuity equation summed over two phases, k and j, is:

$$\frac{\partial}{\partial t} [\varepsilon (s_k \rho_k + s_j \rho_j)] + \nabla \cdot \left[\varepsilon \left(s_k \rho_k \langle \mathbf{V}_k \rangle^k + s_j \rho_j \langle \mathbf{V}_j \rangle^j \right) \right] = 0 \quad (1)$$

Defining mixture density and the mixture velocity

$$\bar{\rho} = s_k \rho_k + s_j \rho_j \quad (2)$$

$$\bar{\rho} \bar{\mathbf{V}} = \varepsilon s_k \rho_k \langle \mathbf{V}_k \rangle^k + \varepsilon s_j \rho_j \langle \mathbf{V}_j \rangle^j \quad (3)$$

the continuity equation can be rewritten as

$$\frac{\partial}{\partial t} (\varepsilon \bar{\rho}) + \nabla \cdot (\bar{\rho} \bar{\mathbf{V}}) = 0 \quad (4)$$

The momentum equation can be summed over both phases.

$$\varepsilon s_k \rho_k \langle \mathbf{V}_k \rangle^k + \varepsilon s_j \rho_j \langle \mathbf{V}_j \rangle^j = -K \left[\frac{K_{rk}}{\nu_k} (\nabla p_k - \rho_k \mathbf{g}) + \frac{K_{rj}}{\nu_j} (\nabla p_j - \rho_j \mathbf{g}) \right] \quad (5)$$

A capillary pressure that relates the pressure in phase k to the pressure in phase j is introduced:

$$p_c = p_j - p_k \quad (6)$$

The capillary pressure is often expressed as the Leverette function (Leverette, 1940). This function relates the capillary pressure to the wetting phase saturation, s_w . A phase is said to wet the porous material if the contact angle that phase makes with it is less than 90° . Therefore, if $\theta_k < 90^\circ$, the wetting phase is phase k, $s_w = s_k$

If

$\theta_j < 90^\circ$, then phase j is the wetting phase, $s_w = s_j$

$$p_c = \sigma \cos \theta \left(\frac{\varepsilon}{K} \right)^{1/2} \left[1.417(1 - s_w) - 2.120(1 - s_w)^2 + 1.263(1 - s_w)^3 \right] \quad (7)$$

This function was developed to describe the capillary pressure in soils engineering; however, its use has been extended to other technology such as fuel cells. The reason for the over usage of the Leverette function is the lack of functions to describe the capillary pressure for other types of porous media. With the definition of the mixture velocity and the capillary pressure, the mixture momentum equation can be rewritten as:

$$\bar{\rho} \bar{\mathbf{V}} = -K \left[\left(\frac{K_{rk}}{\nu_k} + \frac{K_{rj}}{\nu_j} \right) \nabla p_j - \frac{K_{rk}}{\nu_k} \nabla p_c - \left(\frac{\rho_k K_{rk}}{\nu_k} + \frac{\rho_j K_{rj}}{\nu_j} \right) \mathbf{g} \right] \quad (8)$$

Note that the capillary pressure gradient can be reduced into its relative components.

$$\nabla p_c = \frac{\partial p_c}{\partial s_k} \nabla s_k + \frac{\partial p_c}{\partial \sigma_{jk}} \sum_{i=1}^{N-1} \frac{\partial \sigma_{jk}}{\partial \langle \omega_{k,i} \rangle^k} \nabla \langle \omega_{k,i} \rangle^k + \frac{\partial p_c}{\partial \sigma_{jk}} \frac{\partial \sigma_{jk}}{\partial T} \nabla T \quad (9)$$

Now the mixture kinematic viscosity, $\bar{\nu}$, and relative mobility, λ_k , are introduced.

$$\bar{\nu} = \left(\frac{K_{rk}}{\nu_k} + \frac{K_{rj}}{\nu_j} \right)^{-1} \quad (10)$$

$$\lambda_k = \frac{K_{rk}}{\nu_k} \bar{\nu} \quad (11)$$

The momentum equation, eq. (8), can be rewritten as:

$$\bar{\rho}\bar{\mathbf{V}} = -\frac{K}{\bar{\nu}} [\nabla p_j - \lambda_k \nabla p_c - (\lambda_k \rho_k + \lambda_j \rho_j) \mathbf{g}] \quad (12)$$

A definition of the mixture pressure is introduced so that:

$$\nabla \bar{p} = \nabla p_j - \lambda_k \nabla p_c \quad (13)$$

A density correction factor, γ_ρ , is also introduced.

$$\gamma_\rho = \frac{1}{\bar{\rho}} (\rho_k \lambda_k + \rho_j \lambda_j) \quad (14)$$

The momentum equation (12) can be written in the form

$$\bar{\rho}\bar{\mathbf{V}} = -\frac{K}{\bar{\nu}} [\nabla \bar{p} - \gamma_\rho \rho \mathbf{g}] \quad (15)$$

In order to simplify the MMM derivation for the species and energy equations, a diffusive phase-mass flux is introduced. This term is analogous to the diffusion mass flux in multicomponent mixtures, but refers to each phase, rather than each component in a phase. This value relates the actual mass flux of phase k to the mixture mass flux.

$$\mathbf{j}_k = \varepsilon s_k \rho_k \langle \mathbf{V}_k \rangle^k - \lambda_k \bar{\rho} \bar{\mathbf{V}} \quad (16)$$

From this relation, it can be shown that the diffusive phase-mass flux is:

$$\mathbf{j}_k = -\mathbf{j}_j = \frac{\lambda_k \lambda_j}{\bar{\nu}} [K \nabla p_c + (\rho_k - \rho_j) \mathbf{g}] \quad (17)$$

This relation will be useful, and will be used henceforth. The mixture species equation for species i is obtained by adding the species i equation for phase k and phase j.

$$\begin{aligned} & \frac{\partial}{\partial t} \left(\varepsilon s_k \rho_k \langle \omega_{k,i} \rangle^k + \varepsilon s_j \rho_j \langle \omega_{j,i} \rangle^j \right) + \nabla \cdot \left(\varepsilon s_k \rho_k \langle \mathbf{V}_k \rangle^k \langle \omega_{k,i} \rangle^k + \varepsilon s_j \rho_j \langle \mathbf{V}_j \rangle^j \langle \omega_{j,i} \rangle^j \right) \\ &= -\nabla \cdot \langle \mathbf{J}_{k,i} + \mathbf{J}_{j,i} \rangle + \dot{m}_{k,i}''' + \dot{m}_{j,i}''' \end{aligned} \quad (18)$$

,

From eq. (18) from Multi-Fluid Model

$$\sum_{k=1}^{\Pi} \dot{m}_{k,i}''' = \dot{m}_i'''$$

the summation of the species production over all the phases is the species production due to chemical reaction. The mixture mass fraction is:

$$\bar{\rho} \bar{\omega}_i = s_k \rho_k \langle \omega_{k,i} \rangle^k + s_j \rho_j \langle \omega_{j,i} \rangle^j \quad (19)$$

The correction factor for species advection, γ_i , is introduced.

$$\gamma_i = \frac{1}{\bar{\omega}_i} \left(\lambda_k \langle \omega_{k,i} \rangle^k + \lambda_j \langle \omega_{j,i} \rangle^j \right) \quad (20)$$

The mixture species equation is:

$$\begin{aligned} & \frac{\partial}{\partial t} (\varepsilon \bar{\rho} \bar{\omega}_i) + \nabla \cdot (\gamma_i \bar{\rho} \bar{\mathbf{V}} \bar{\omega}_i) \\ &= -\nabla \cdot \langle \mathbf{J}_{k,i} + \mathbf{J}_{j,i} \rangle - \nabla \cdot \left(\mathbf{j}_k \left(\langle \omega_{k,i} \rangle^k - \langle \omega_{j,i} \rangle^j \right) \right) + \dot{m}_i''' \end{aligned} \quad (21)$$

It should be noted that eqs. (4), (15), and (21) are also applicable to multiphase and not necessary to two-phase as developed here.

It is important to point out that the mixture species equation still contains the species mass fraction of each phase. Therefore, the species mass fraction in phase k and phase j must be related to the mixture mass fraction through thermodynamic equilibrium. Expanding all the terms in eq. (4.297) yields:

$$(s_k \rho_k + s_j \rho_j) \bar{\omega}_i = s_k \rho_k \langle \omega_{k,i} \rangle^k + s_j \rho_j \langle \omega_{j,i} \rangle^j \quad (22)$$

Since there are two phases presented, the phase saturations add to unity. Therefore, the phase saturation of phase k can be calculated by:

$$s_k = \frac{\rho_j (\bar{\omega}_i - \langle \omega_{j,i} \rangle^j)}{\rho_k (\bar{\omega}_i - \langle \omega_{k,i} \rangle^k) + \rho_j (\langle \omega_{j,i} \rangle^k - \bar{\omega}_i)} \quad (23)$$

It is important to note that when the saturation of phase k is calculated in this manner, one phase continuity equation is not solved; instead, all N species equations are solved. For more discussion on this approach to the calculation of the phase saturation, refer to the comparison of MFM and MMM models below.

The last transport equation that must be examined is the energy equation. The energy equation of both phases are added together plus an unsteady and heat conduction term represents the influence of the solid matrix on the energy equation.

$$\begin{aligned} \frac{\partial}{\partial t} ((1 - \varepsilon) \rho_{sm} \langle h_{sm} \rangle^{sm} + \varepsilon [s_k \rho_k \langle h_k \rangle^k + s_j \rho_j \langle h_j \rangle^j]) + \\ \nabla \cdot (\varepsilon [s_k \rho_k \langle \mathbf{V}_k \rangle^k \langle h_k \rangle^k + s_j \rho_j \langle \mathbf{V}_j \rangle^j \langle h_j \rangle^j]) = -\nabla \cdot \langle \mathbf{q}''_{k,i} + \mathbf{q}''_{j,i} + \mathbf{q}''_{sm,i} \rangle + \dot{q}_E''' \end{aligned} \quad (24)$$

The external heat generation is represented by \dot{q}_E''' , and it is the summation of the external heat generation over all of the phases. The mixture enthalpy is

$$\bar{h} = s_k \rho_k \langle h_k \rangle^k + s_j \rho_j \langle h_j \rangle^j \quad (25)$$

The correction factor for energy advection, γ_h , is also introduced:

$$\gamma_h = \frac{1}{\bar{h}} (\lambda_k \langle h_k \rangle^k + \lambda_j \langle h_j \rangle^j) \quad (26)$$

An assumption that corresponds with the mixture enthalpy is that each phase is in thermodynamic equilibrium, . If Fourier's law governs the heat conduction and effective thermal conductivity can be used, the energy equation can be rewritten using an effective thermal conductivity and the diffusive phase-mass flux as:

$$\begin{aligned} \frac{\partial}{\partial t} ((1 - \varepsilon) \rho_{sm} \langle h_{sm} \rangle^{sm} + \varepsilon \bar{\rho} \bar{h}) + \nabla \cdot (\gamma_h \bar{\rho} \bar{\mathbf{V}} \bar{h}) = \\ \nabla \cdot (k_{eff} \nabla T) - \nabla \cdot (\mathbf{j}_k (\langle h_k \rangle^k - \langle h_j \rangle^j)) + \dot{q}_E''' \end{aligned} \quad (27)$$

where the effective thermal conductivity is related to the phase saturation, porosity, geometry of the porous medium (tortuosity, \mathfrak{T}) and the conductivity of the porous media and both phases, . $k_{eff} = f(k_{sm}, k_k, k_j, \varepsilon, s_k, \mathfrak{T})$

It is important to note that the heat generation and consumption of chemical reactions and latent heat are all embedded in this governing equation.

6.2.1. Volume of Fluid

The method is based on the idea of so-called fraction function.

$$\frac{\partial C}{\partial t} + \mathbf{v} \cdot \nabla C = 0.$$

6.3. Viscous Regima:

6.3.1. Turbulent:

In fluid dynamics, turbulence or turbulent flow is a flow regime characterized by chaotic and stochastic property changes. This includes low momentum diffusion, high momentum convection, and rapid variation of pressure and velocity in space and time. Nobel Laureate Richard Feynman described turbulence as "the most important unsolved problem of classical physics." Flow in which the kinetic energy dies out due to the action of fluid molecular viscosity is called laminar flow. While there is no theorem relating the non-dimensional Reynolds number (Re) to turbulence, flows at Reynolds numbers larger than 100000 are typically (but not necessarily) turbulent, while those at low Reynolds numbers usually remain laminar. In Poiseuille flow, for example, turbulence can first be sustained if the Reynolds number is larger than a critical value of about 2040; moreover, the turbulence is generally interspersed with laminar flow until a larger Reynolds number of about 3000. In turbulent flow, unsteady vortices appear on many scales and interact with each other. Drag due to boundary layer skin friction increases. The structure and location of boundary layer separation often changes, sometimes resulting in a reduction of overall drag. Although laminar-turbulent transition is not governed by Reynolds number, the same transition occurs if the size of the object is gradually increased, or the viscosity of the fluid is decreased, or if the density of the fluid is increased.

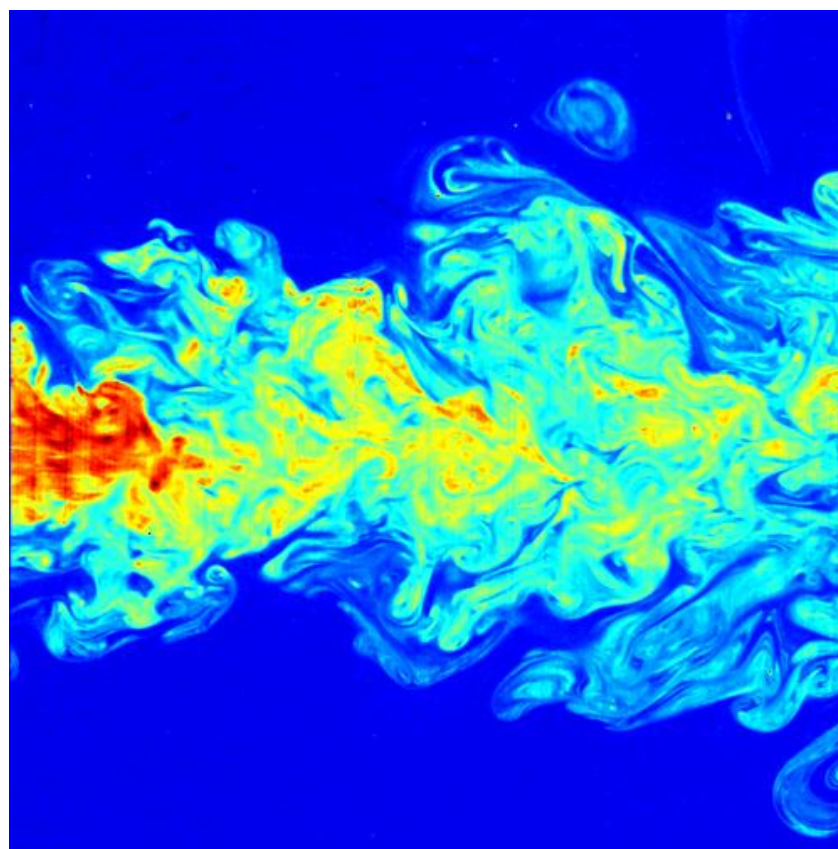


Figure 12: This picture is a false-color image of the far-field of a submerged turbulent jet, made visible by means of laser induced fluorescence (LIF). C. Fukushima and J. Westerweel, Technical University of Delft, The Netherlands

6.4. Reynold-Averaged Turbulance Model

The Reynolds-averaged Navier–Stokes equations (or RANS equations) are time-averaged equations of motion for fluid flow. The idea behind the equations is Reynolds decomposition, whereby an instantaneous quantity is decomposed into its time-averaged and fluctuating quantities, an idea first proposed by Osborne Reynolds. The RANS equations are primarily used to describe turbulent flows. These equations can be used with approximations based on knowledge of the properties of flow turbulence to give approximate time-averaged solutions to the Navier–Stokes equations. For a stationary, incompressible Newtonian fluid, these equations can be written in Einstein notation as:

$$\rho \bar{u}_j \frac{\partial \bar{u}_i}{\partial x_j} = \rho \bar{f}_i + \frac{\partial}{\partial x_j} \left[-\bar{p} \delta_{ij} + \mu \left(\frac{\partial \bar{u}_i}{\partial x_j} + \frac{\partial \bar{u}_j}{\partial x_i} \right) - \rho \bar{u}'_i \bar{u}'_j \right].$$

The left hand side of this equation represents the change in mean momentum of fluid element owing to the unsteadiness in the mean flow and the convection by the mean flow. This change is balanced by the mean body force, the isotropic stress owing to the mean pressure field, the viscous stresses, and apparent stress $(-\rho \bar{u}'_i \bar{u}'_j)$ owing to the fluctuating velocity field, generally referred to as the Reynolds stress. This nonlinear Reynolds stress term requires additional modeling to close the RANS equation for solving, and has led to the creation of many different turbulence models. The time-average operator $\bar{\cdot}$ is a Reynolds operator.

Derivation of RANS equations

The basic tool required for the derivation of the RANS equations from the instantaneous Navier–Stokes equations is the Reynolds decomposition. Reynolds decomposition refers to separation of the flow variable (like velocity u) into the mean (time-averaged) component (\bar{u}) and the fluctuating component (u'). Because the mean operator is a Reynolds operator, it has a set of properties. One of these properties is that the mean of the fluctuating quantity being equal to zero ($\bar{u}' = 0$). Thus,

$$u(\mathbf{x}, t) = \bar{u}(\mathbf{x}) + u'(\mathbf{x}, t),$$

where $\mathbf{x} = (x, y, z)$ is the position vector. Some author prefer using U instead of \bar{u} for the mean term (since an overbar is sometimes used to represent a vector). In this case, the fluctuating term u' is represented instead by u . This is possible because the two terms do not appear simultaneously in the same equation. To avoid confusion, the notation u , \bar{u} , and u' will be used to represent the instantaneous, mean, and fluctuating terms, respectively. The properties of Reynolds operators are useful in the derivation of the RANS equations. Using these properties, the Navier–Stokes equations of motion, expressed in tensor notation, are (for an incompressible Newtonian fluid):

$$\frac{\partial u_i}{\partial x_i} = 0$$

$$\frac{\partial u_i}{\partial t} + u_j \frac{\partial u_i}{\partial x_j} = f_i - \frac{1}{\rho} \frac{\partial p}{\partial x_i} + \nu \frac{\partial^2 u_i}{\partial x_j \partial x_j}$$

where f_i is a vector representing external forces. Next, each instantaneous quantity can be split into time-averaged and fluctuating components, and the resulting equation time-averaged, to yield:

$$\frac{\partial \bar{u}_i}{\partial x_i} = 0$$

$$\frac{\partial \bar{u}_i}{\partial t} + \bar{u}_j \frac{\partial \bar{u}_i}{\partial x_j} + \overline{u'_j \frac{\partial u'_i}{\partial x_j}} = \bar{f}_i - \frac{1}{\rho} \frac{\partial \bar{p}}{\partial x_i} + \nu \frac{\partial^2 \bar{u}_i}{\partial x_j \partial x_j}.$$

The momentum equation can also be written as,^[4]

$$\frac{\partial \bar{u}_i}{\partial t} + \bar{u}_j \frac{\partial \bar{u}_i}{\partial x_j} = \bar{f}_i - \frac{1}{\rho} \frac{\partial \bar{p}}{\partial x_i} + \nu \frac{\partial^2 \bar{u}_i}{\partial x_j \partial x_j} - \frac{\partial \overline{u'_i u'_j}}{\partial x_j}.$$

On further manipulations this yields,

$$\rho \frac{\partial \bar{u}_i}{\partial t} + \rho \bar{u}_j \frac{\partial \bar{u}_i}{\partial x_j} = \rho \bar{f}_i + \frac{\partial}{\partial x_j} \left[-\bar{p} \delta_{ij} + 2\mu \bar{S}_{ij} - \rho \overline{u'_i u'_j} \right]$$

$$\bar{S}_{ij} = \frac{1}{2} \left(\frac{\partial \bar{u}_i}{\partial x_j} + \frac{\partial \bar{u}_j}{\partial x_i} \right)$$

where, \bar{S}_{ij} is the mean rate of strain tensor.

Finally, since integration in time removes the time dependence of the resultant terms, the time derivative must be eliminated, leaving:

$$\rho \bar{u}_j \frac{\partial \bar{u}_i}{\partial x_j} = \rho \bar{f}_i + \frac{\partial}{\partial x_j} \left[-\bar{p} \delta_{ij} + 2\mu \bar{S}_{ij} - \rho \overline{u'_i u'_j} \right].$$

6.4.1. Standard k-epsilon model

Transport equations for standard k-epsilon model

For turbulent kinetic energy k

$$\frac{\partial}{\partial t}(\rho k) + \frac{\partial}{\partial x_i}(\rho k u_i) = \frac{\partial}{\partial x_j} \left[\left(\mu + \frac{\mu_t}{\sigma_k} \right) \frac{\partial k}{\partial x_j} \right] + P_k + P_b - \rho \epsilon - Y_M + S_k$$

For dissipation ϵ

$$\frac{\partial}{\partial t}(\rho \epsilon) + \frac{\partial}{\partial x_i}(\rho \epsilon u_i) = \frac{\partial}{\partial x_j} \left[\left(\mu + \frac{\mu_t}{\sigma_\epsilon} \right) \frac{\partial \epsilon}{\partial x_j} \right] + C_{1\epsilon} \frac{\epsilon}{k} (P_k + C_{3\epsilon} P_b) - C_{2\epsilon} \rho \frac{\epsilon^2}{k} + S_\epsilon$$

Modeling turbulent viscosity

Turbulent viscosity is modelled as:

$$\mu_t = \rho C_\mu \frac{k^2}{\epsilon}$$

Production of k

$$P_k = -\rho \overline{u'_i u'_j} \frac{\partial u_j}{\partial x_i}$$

$$P_k = \mu_t S^2$$

Where S is the modulus of the mean rate-of-strain tensor, defined as :

$$S \equiv \sqrt{2S_{ij}S_{ij}}$$

Effect of buoyancy

$$P_b = \beta g_i \frac{\mu_t}{\text{Pr}_t} \frac{\partial T}{\partial x_i}$$

where Pr_t is the turbulent Prandtl number for energy and g_i is the component of the gravitational vector in the i th direction. For the standard and realizable - models, the default value of Pr_t is 0.85.

The coefficient of thermal expansion, β , is defined as

$$\beta = -\frac{1}{\rho} \left(\frac{\partial \rho}{\partial T} \right)_p$$

Model constants

$$C_{1\epsilon} = 1.44, \quad C_{2\epsilon} = 1.92, \quad C_\mu = 0.09, \quad \sigma_k = 1.0, \quad \sigma_\epsilon = 1.3$$

6.4.2. Realisable k-epsilon model

Transport Equations

$$\frac{\partial}{\partial t}(\rho k) + \frac{\partial}{\partial x_j}(\rho k u_j) = \frac{\partial}{\partial x_j} \left[\left(\mu + \frac{\mu_t}{\sigma_k} \right) \frac{\partial k}{\partial x_j} \right] + P_k + P_b - \rho \epsilon - Y_M + S_k$$

$$\frac{\partial}{\partial t}(\rho\epsilon) + \frac{\partial}{\partial x_j}(\rho\epsilon u_j) = \frac{\partial}{\partial x_j} \left[\left(\mu + \frac{\mu_t}{\sigma_\epsilon} \right) \frac{\partial \epsilon}{\partial x_j} \right] + \rho C_1 S \epsilon - \rho C_2 \frac{\epsilon^2}{k + \sqrt{\nu \epsilon}} + C_{1\epsilon} \frac{\epsilon}{k} C_{3\epsilon} P_b + S_\epsilon$$

Where

$$C_1 = \max \left[0.43, \frac{\eta}{\eta + 5} \right], \quad \eta = S \frac{k}{\epsilon}, \quad S = \sqrt{2S_{ij}S_{ij}}$$

In these equations, P_k represents the generation of turbulence kinetic energy due to the mean velocity gradients, calculated in same manner as standard k-epsilon model. P_b is the generation of turbulence kinetic energy due to buoyancy, calculated in same way as standard k-epsilon model.

Modelling Turbulent Viscosity

$$\mu_t = \rho C_\mu \frac{k^2}{\epsilon}$$

where

$$C_\mu = \frac{1}{A_0 + A_s \frac{kU^*}{\epsilon}}$$

$$U^* \equiv \sqrt{S_{ij}S_{ij} + \tilde{\Omega}_{ij}\tilde{\Omega}_{ij}},$$

$$\tilde{\Omega}_{ij} = \Omega_{ij} - 2\epsilon_{ijk}\omega_k;$$

$$\Omega_{ij} = \overline{\Omega_{ij}} - \epsilon_{ijk}\omega_k$$

where $\overline{\Omega_{ij}}$ is the mean rate-of-rotation tensor viewed in a rotating reference frame with the angular velocity ω_k . The model constants A_0 and A_s are given by:
 $A_0 = 4.04$, $A_s = \sqrt{6} \cos \phi$

$$\phi = \frac{1}{3} \cos^{-1}(\sqrt{6}W), \quad W = \frac{S_{ij}S_{jk}S_{ki}}{\tilde{S}^3}, \quad \tilde{S} = \sqrt{S_{ij}S_{ij}}, \quad S_{ij} = \frac{1}{2} \left(\frac{\partial u_j}{\partial x_i} + \frac{\partial u_i}{\partial x_j} \right)$$

Model Constants

$$C_{1\epsilon} = 1.44, \quad C_2 = 1.9, \quad \sigma_k = 1.0, \quad \sigma_\epsilon = 1.2$$

7. CFD Results

By using these equations; we're going to create 2 simulations are symmetry and full. First of all; we wanted to show how we can combine the equations in CFD program.

Firstly, we need a cad program to draw our model of platform that is 3-leg and connected gravity based concrete.in act, you can see the dimensions of platform in this slide. However, height of boundary is 431 meters, water level 119.5 meters. Width of boundary is 400 meters. The last one is the length that is 810 meters. Basicly,8 meters is base size of the mesh.and then prism layer is selected as 2.minimum relative Surface size percent is 20 and realtive target size percent is 75 for all regions.

However, we need to calculate specificly platform therefore surface growth rate very slow, prism layer is 10, minimum surface siz percent 10 and target size percent is 20 for the region of platform.

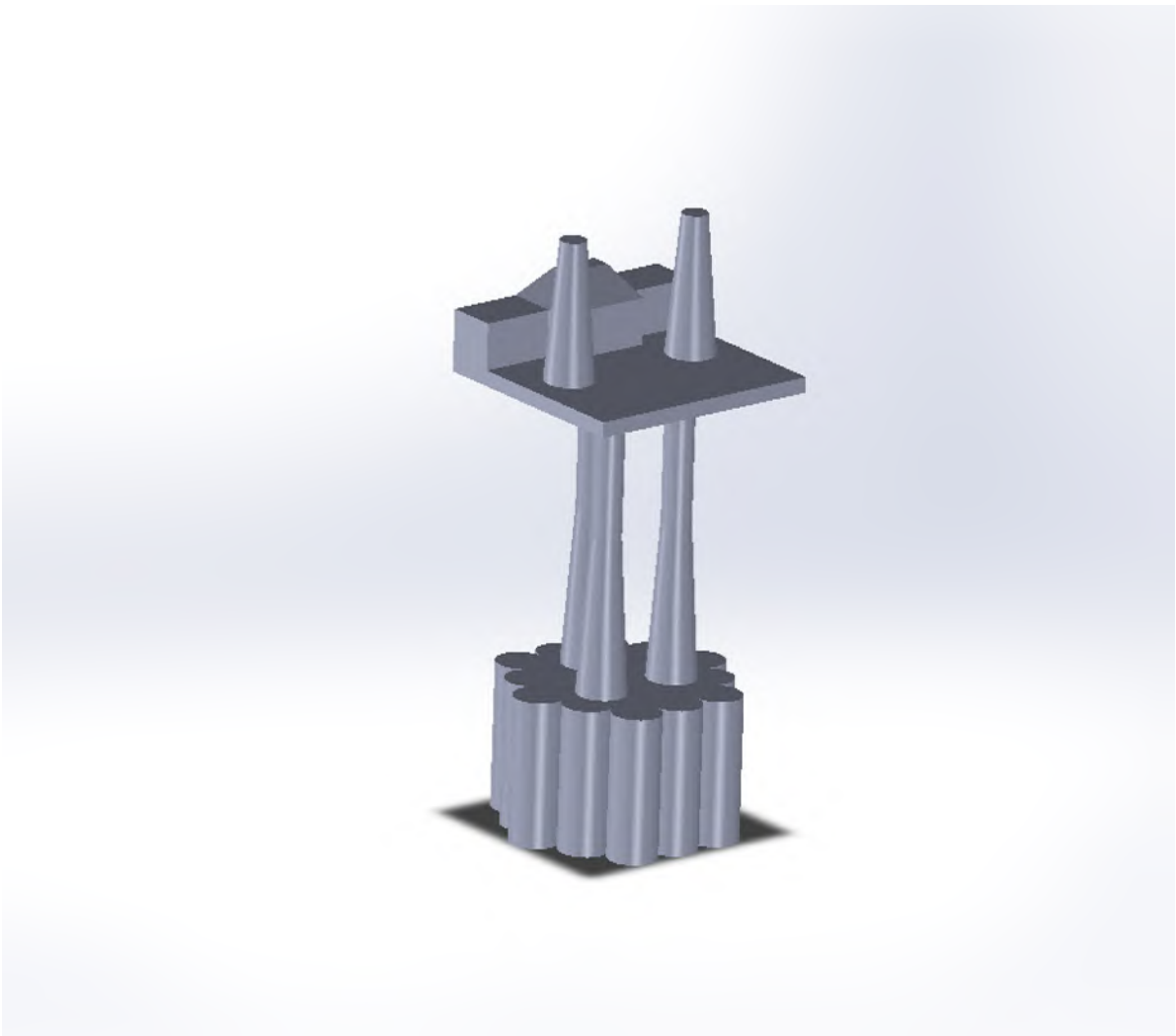


Figure13: 3D model drawn by a cad program

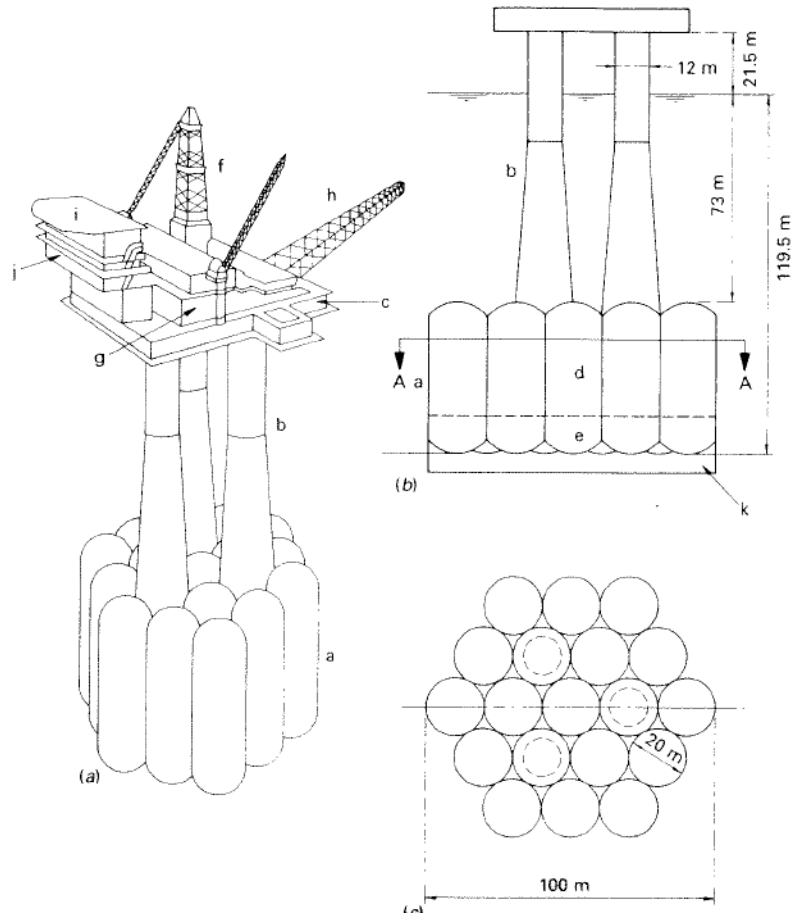


Figure14: Technical Drawing of Platform

While creating simulation, we've used over natural datas as velocity of air and current as you can see the datas in this slide. Then we had to enter initial conditions for simulations because of water level, current and air velocity. Also Cfd program has calculated 2000 iterations for each simulations.

There are 3 main results "velocity, pressure and wall shear stress".

7.1. Symetry plane:

7.1.1. Velocity results.

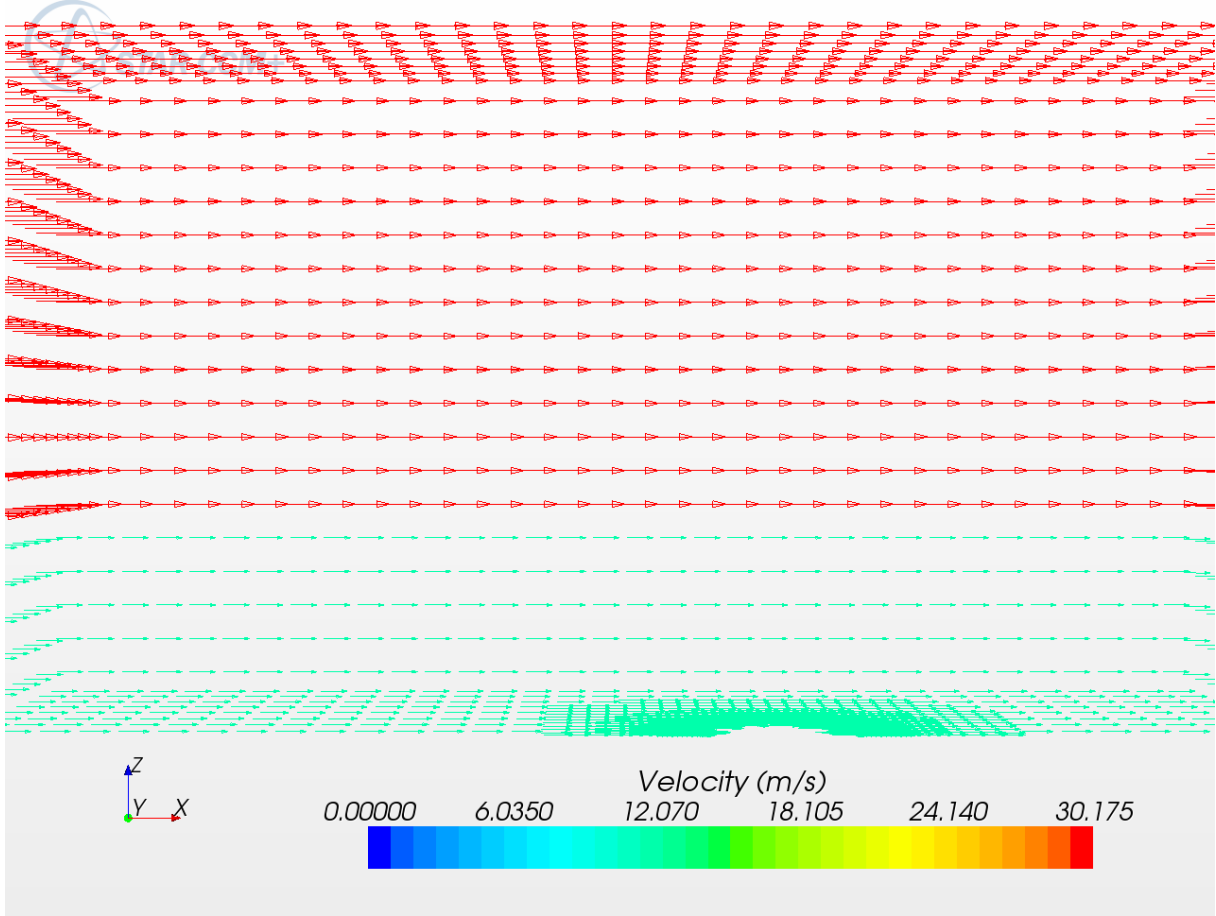


Figure15:Velocity results on 1st second

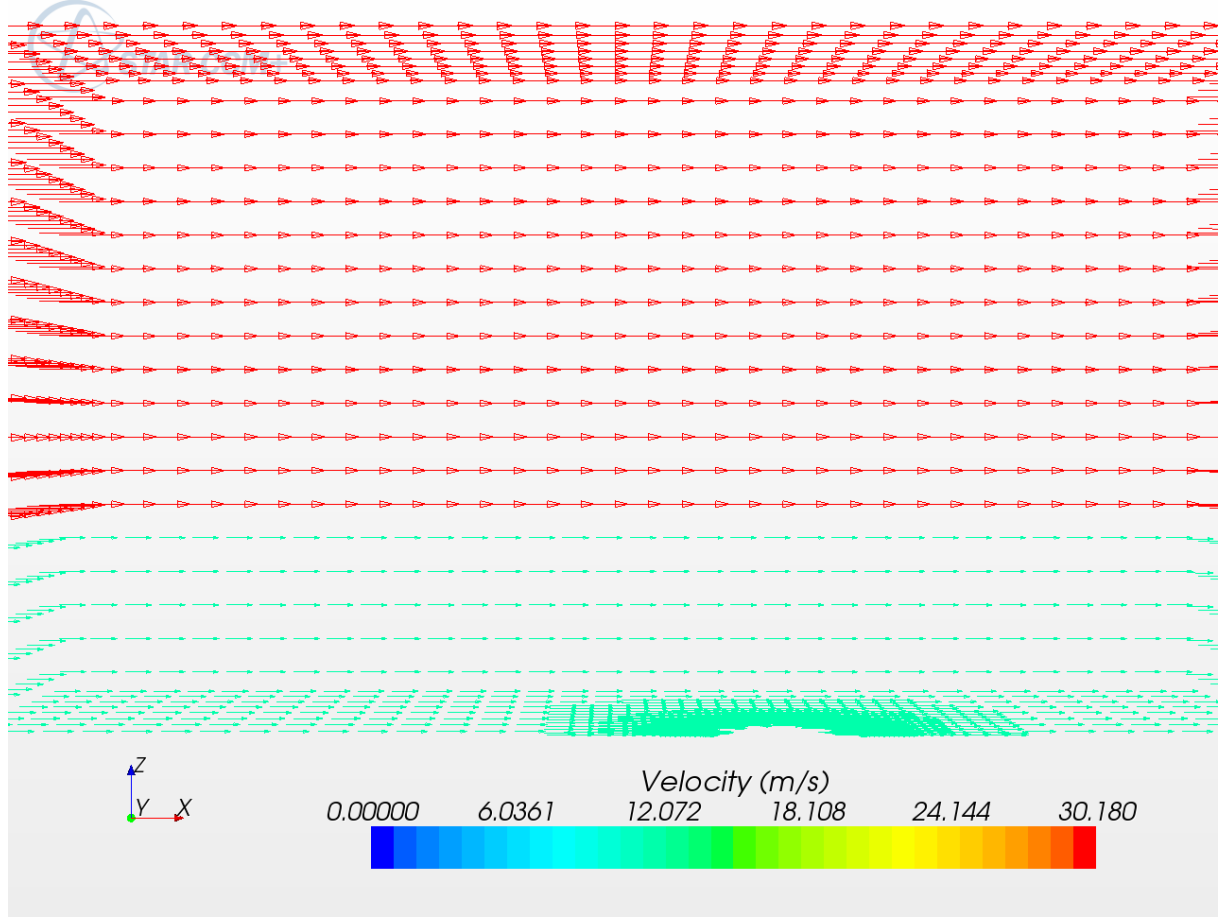


Figure16: Velocity Result on 2nd second

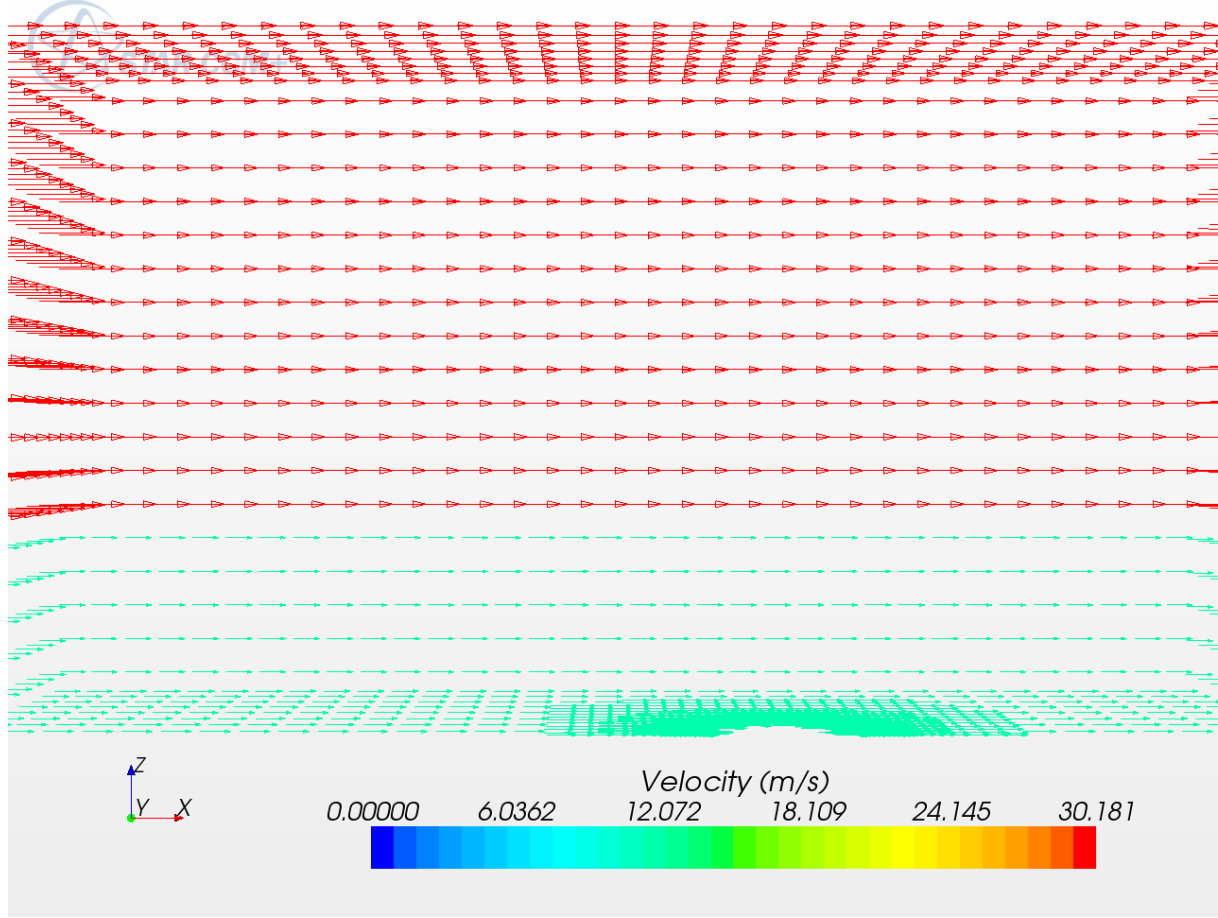


Figure17: Velocity Result on 3rd second

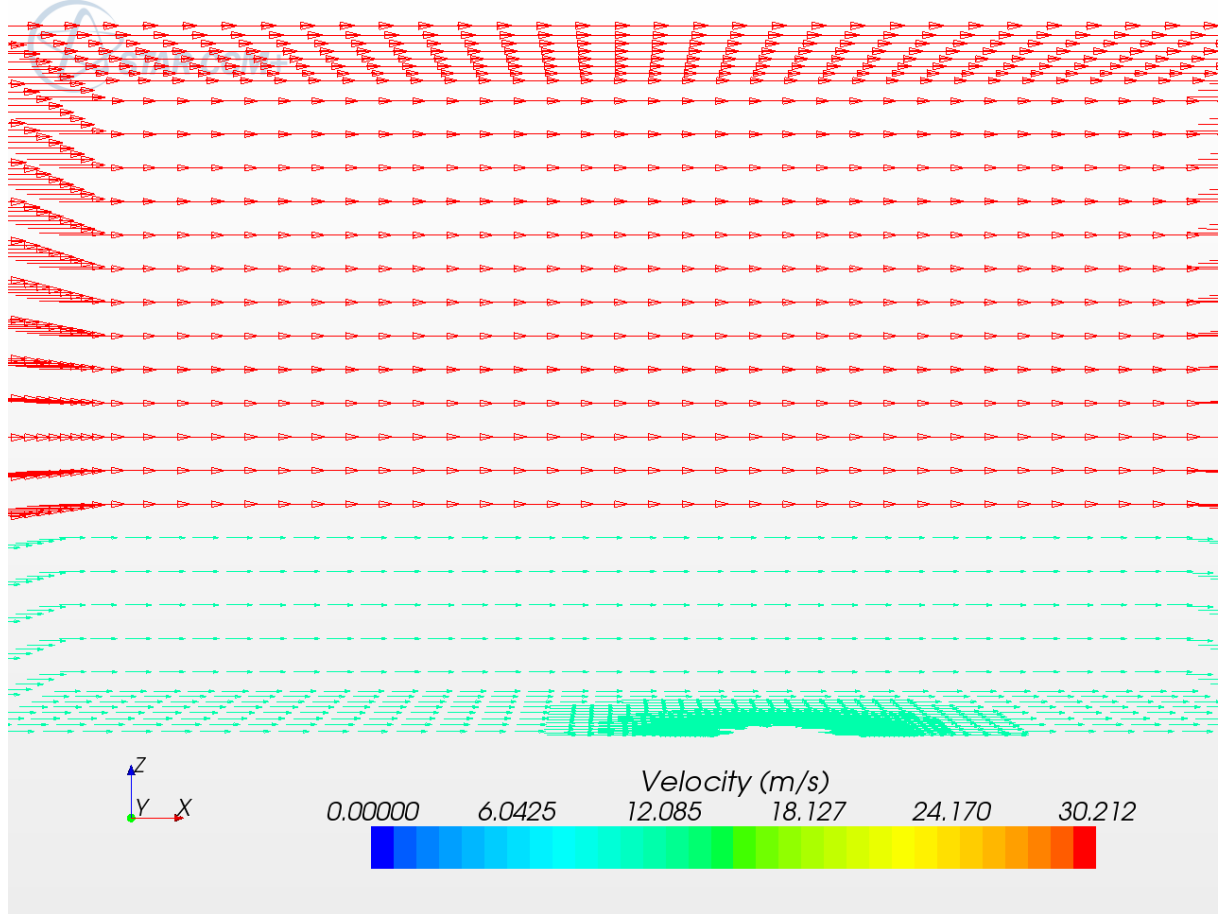


Figure18: Velocity Result on 4th second

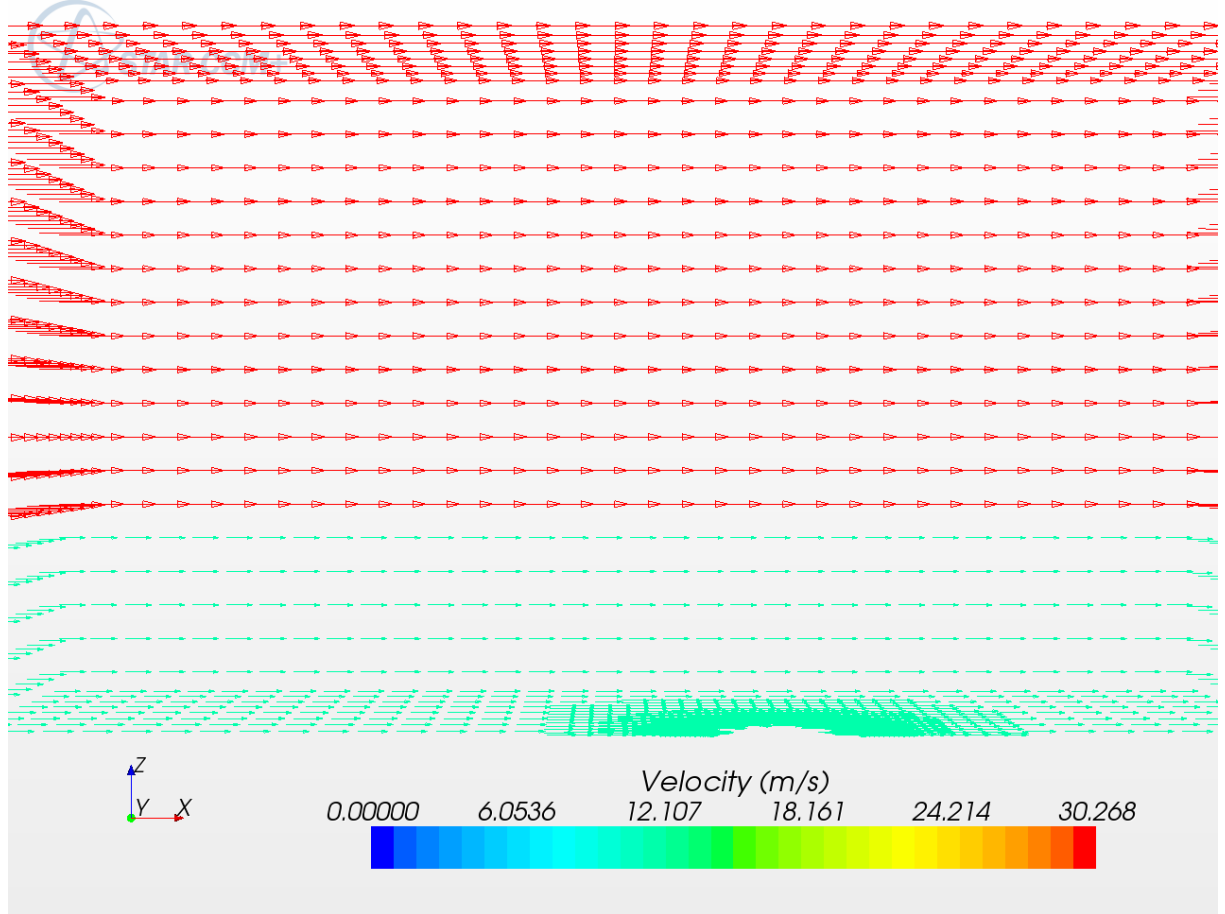


Figure19: Velocity Result on 5th second

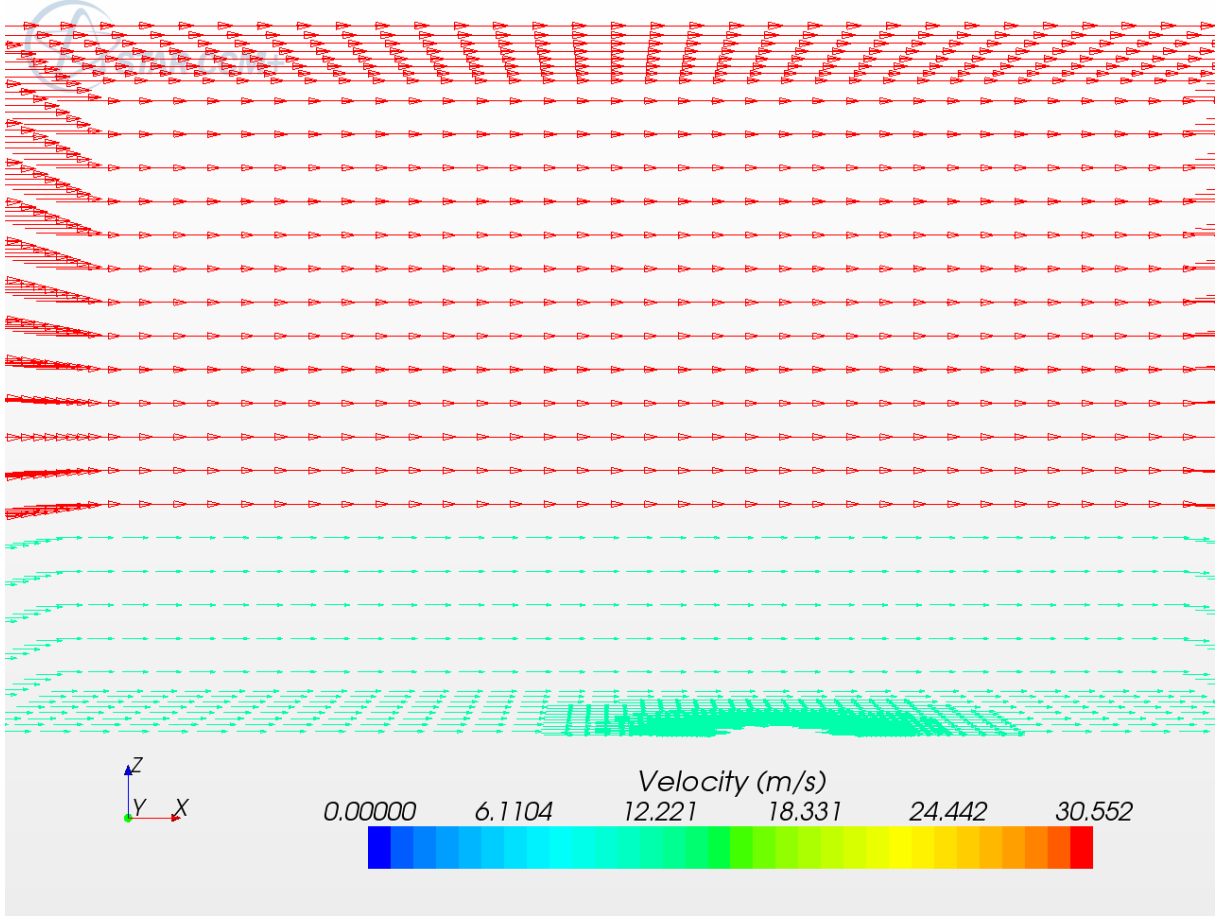


Figure20: Velocity Result on 6th second

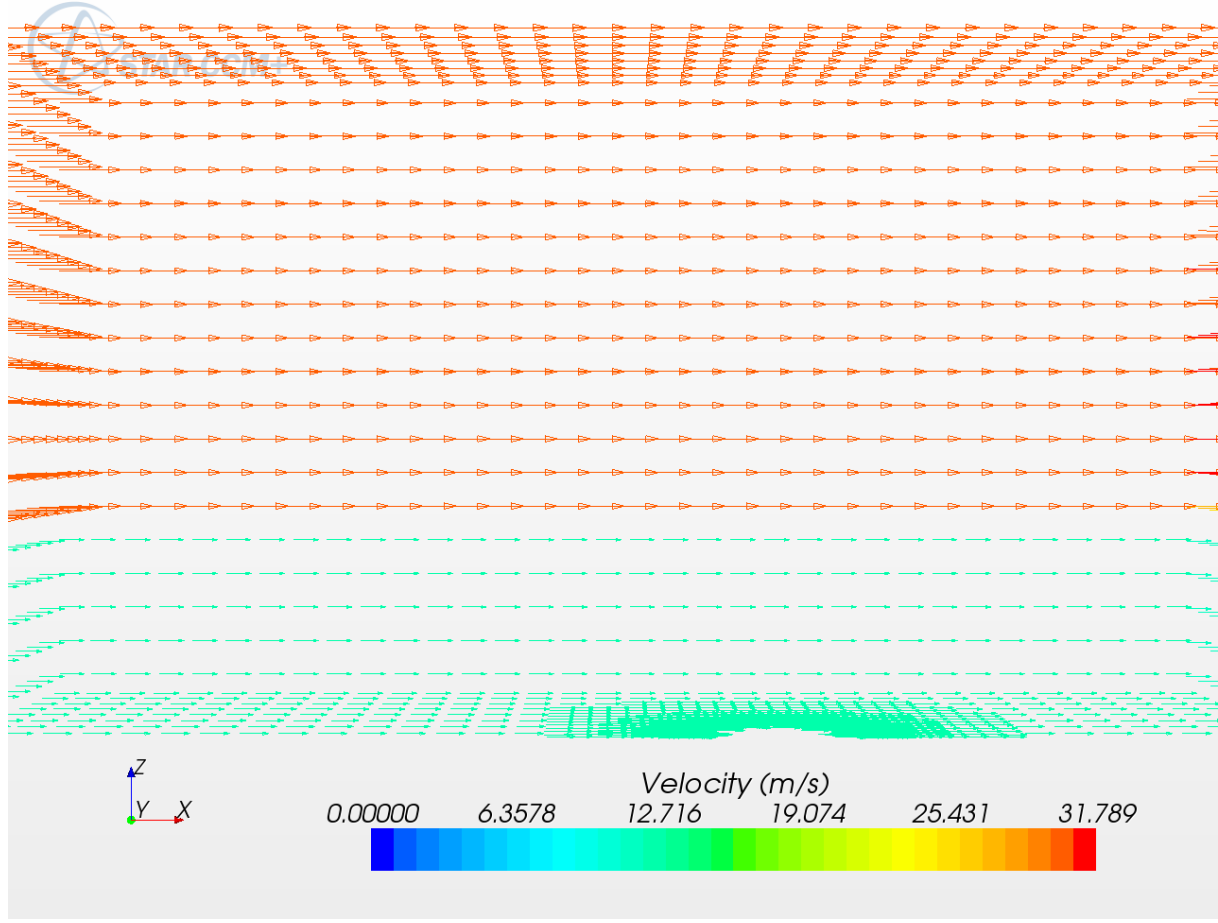


Figure21: Velocity Result on 7th second

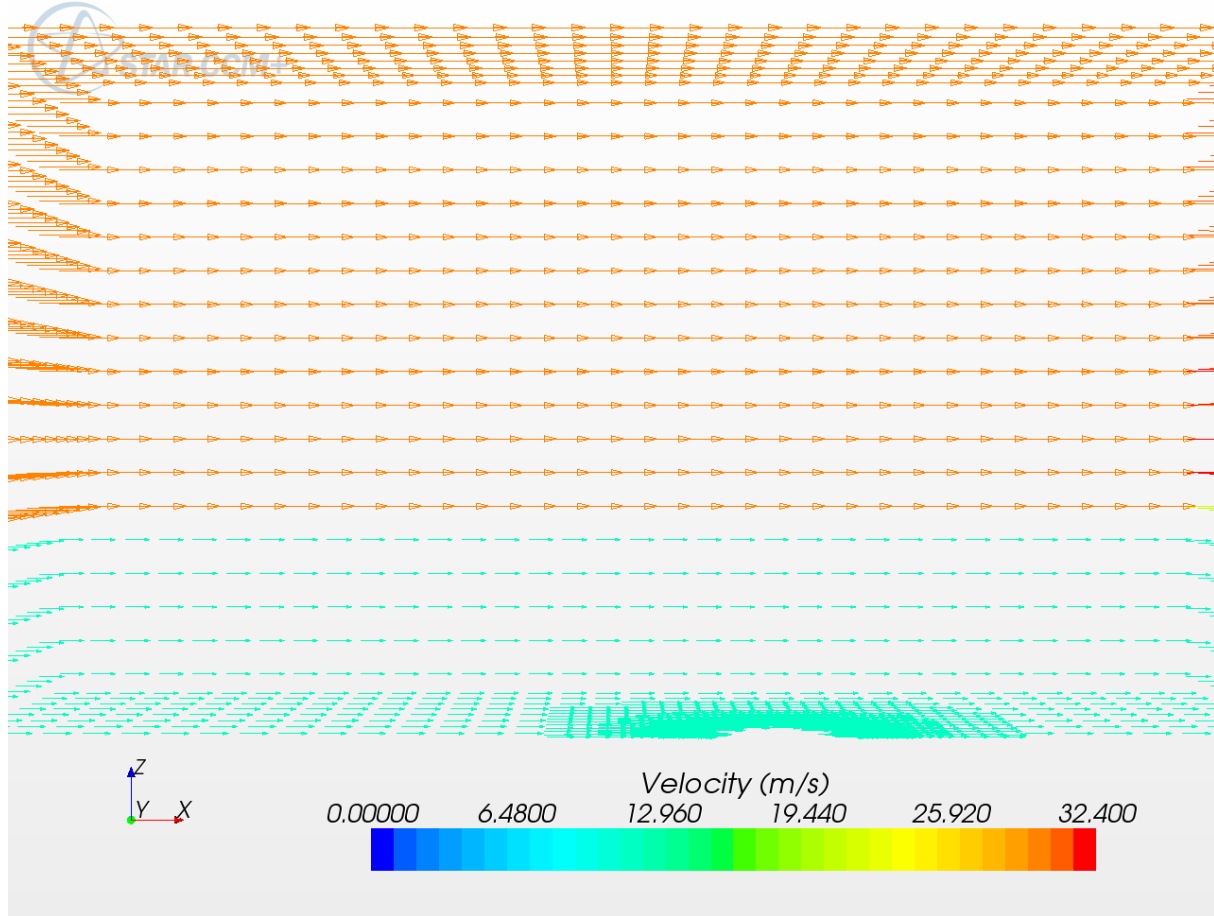


Figure22: Velocity Result on 8th second

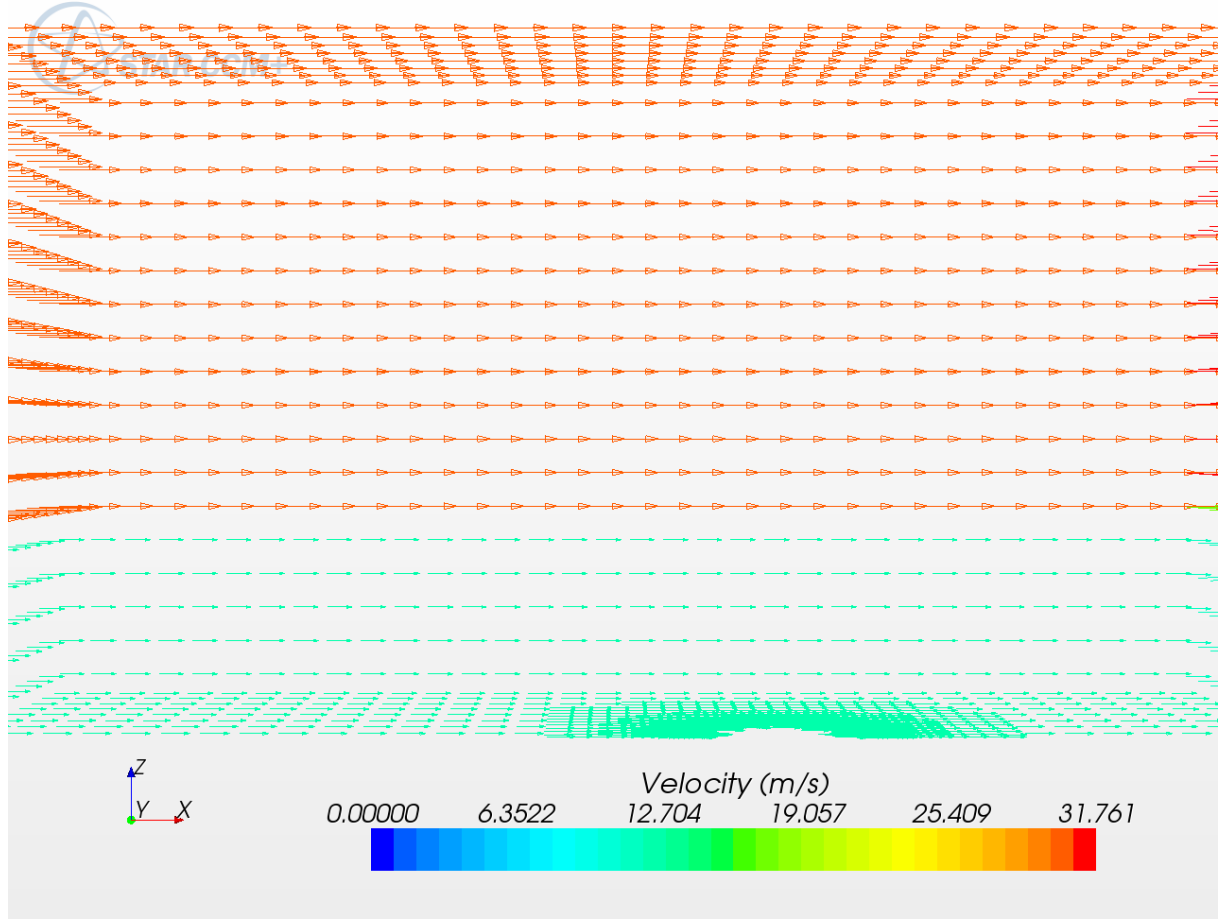


Figure23: Velocity Result on 9th second

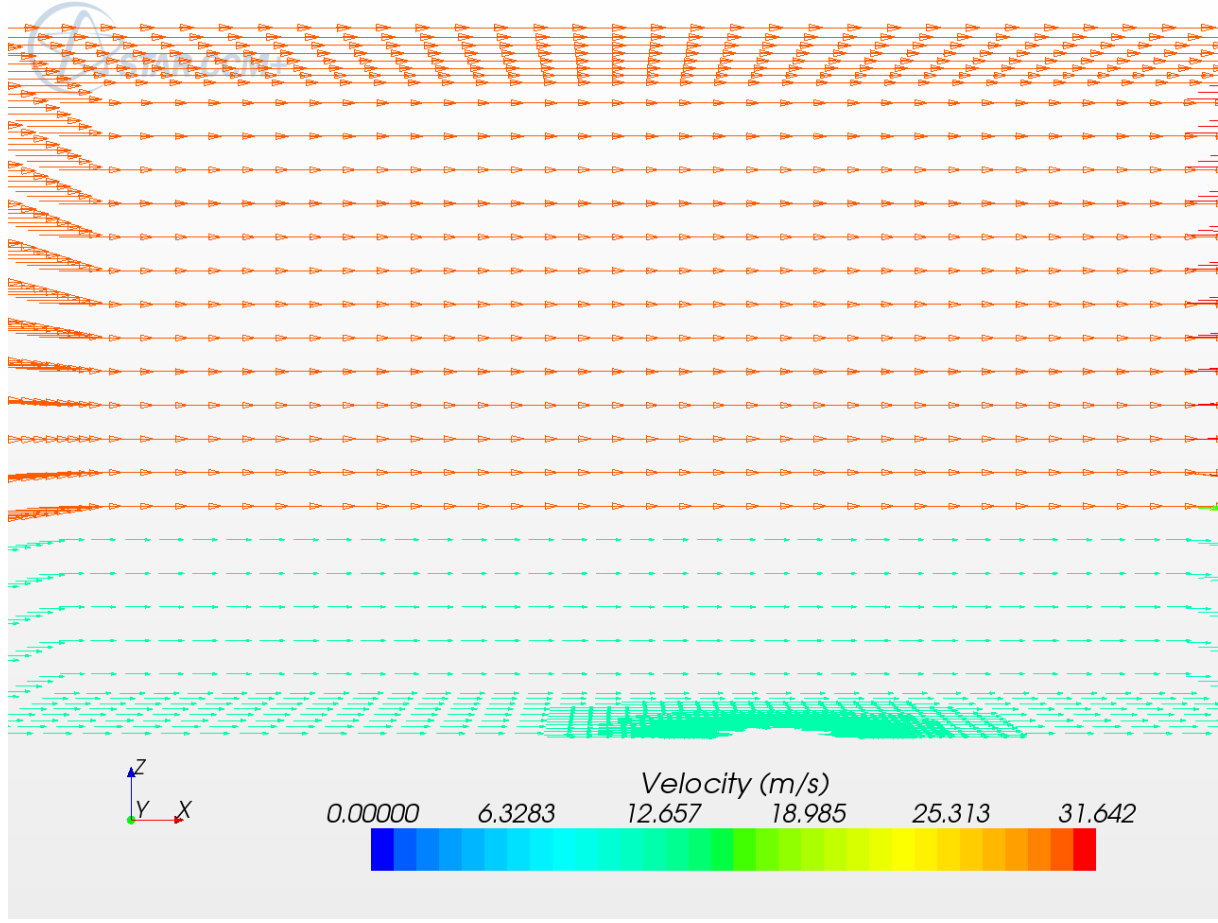


Figure24: Velocity Result on 10th second

7.1.2. Pressure Results

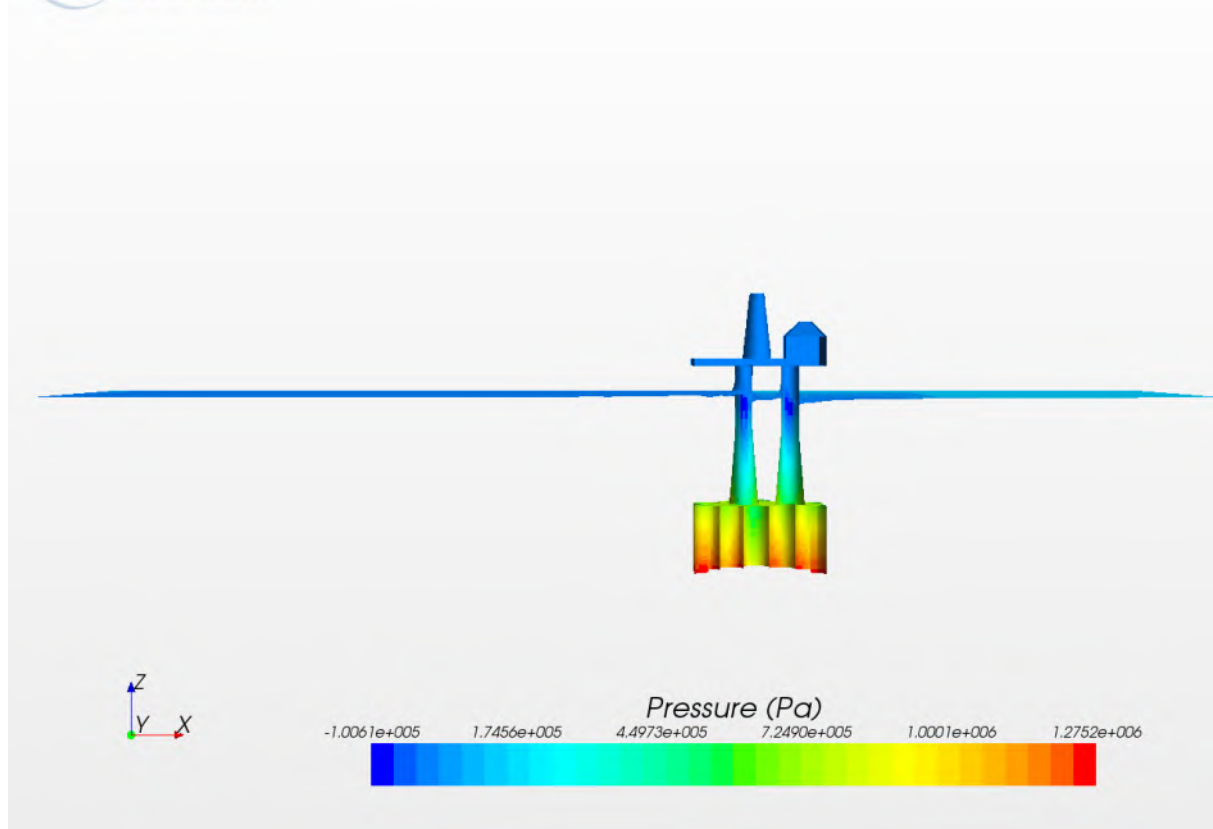


Figure25:Pressure Results in 1st second

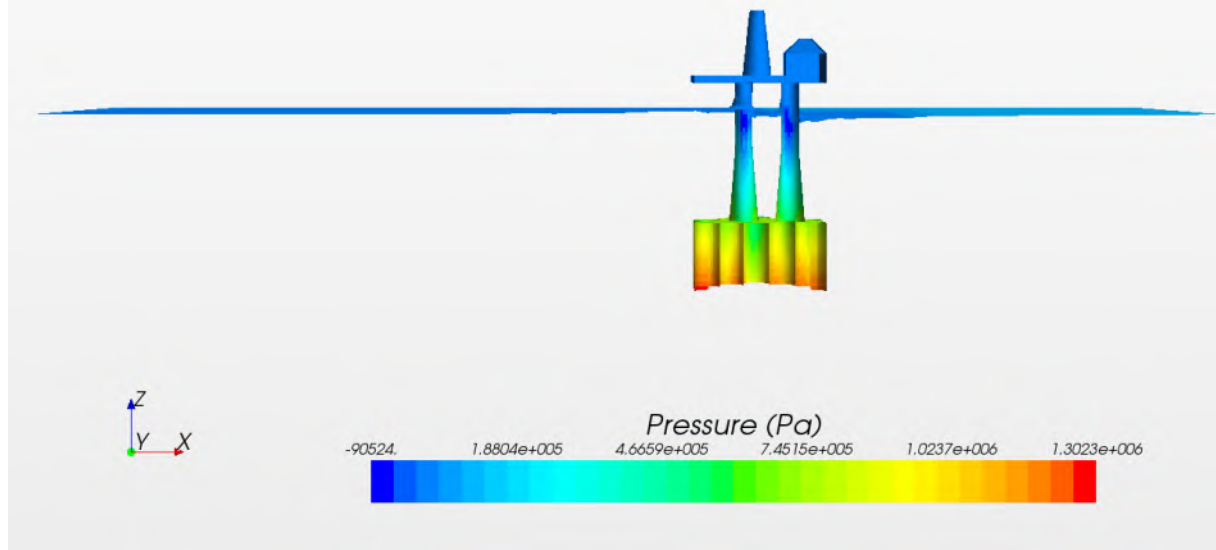


Figure26:Pressure Results in 2nd second

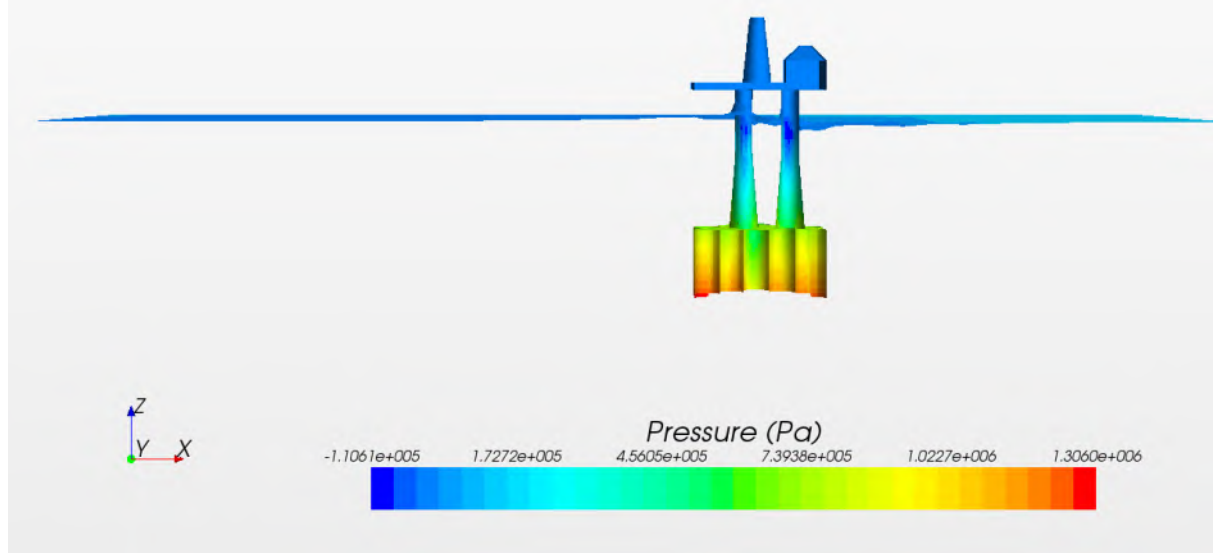


Figure27:Pressure Results in 3rd second

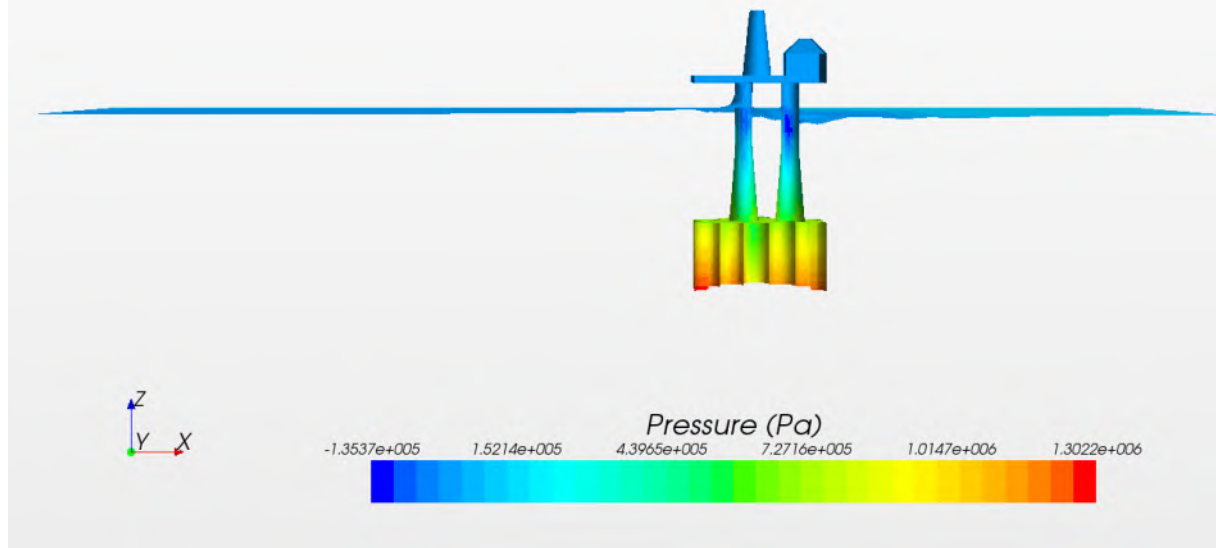


Figure28:Pressure Results in 4th second

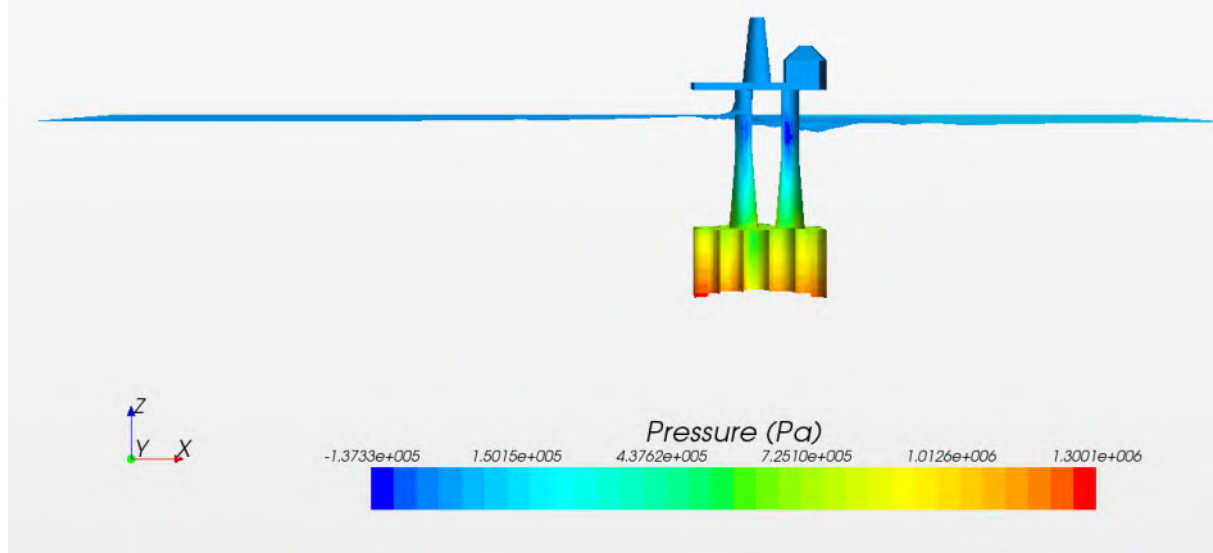


Figure29:Pressure Results in 5th second

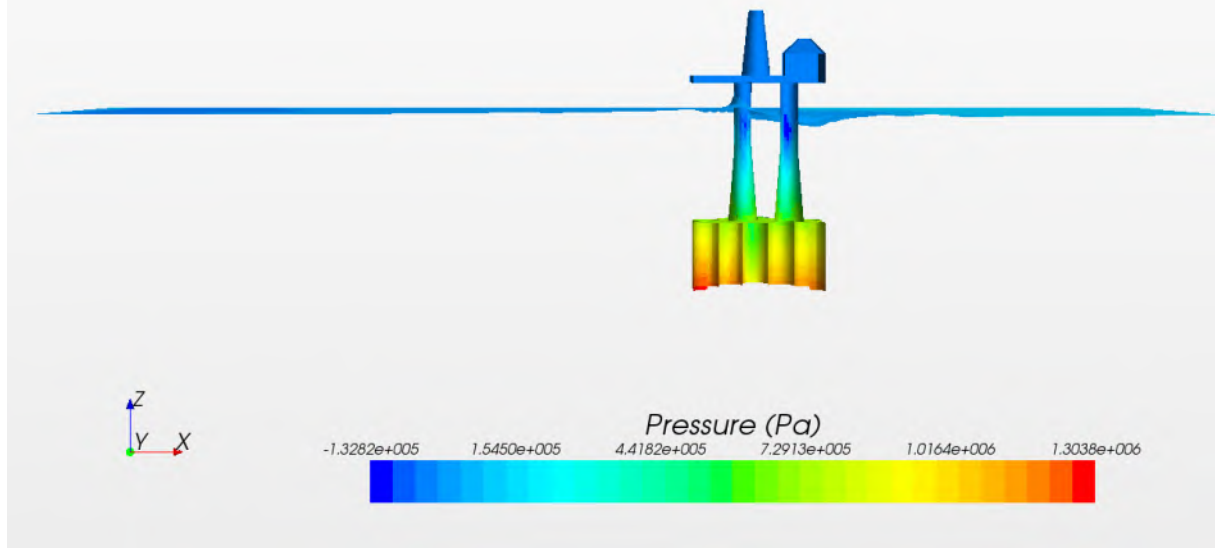


Figure30:Pressure Results in 6th second

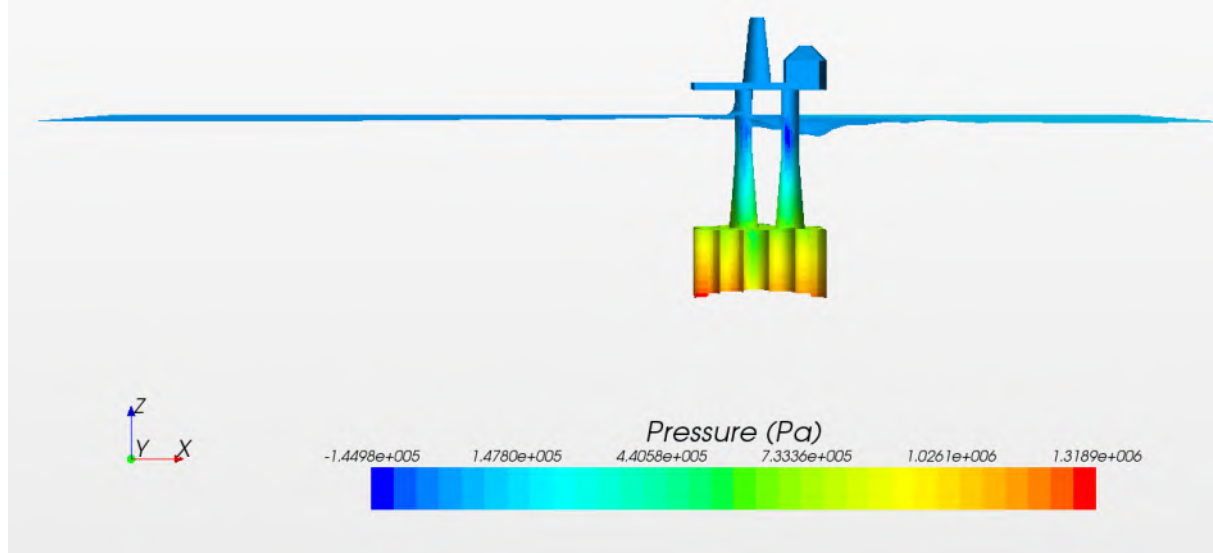


Figure31:Pressure Results in 7th second

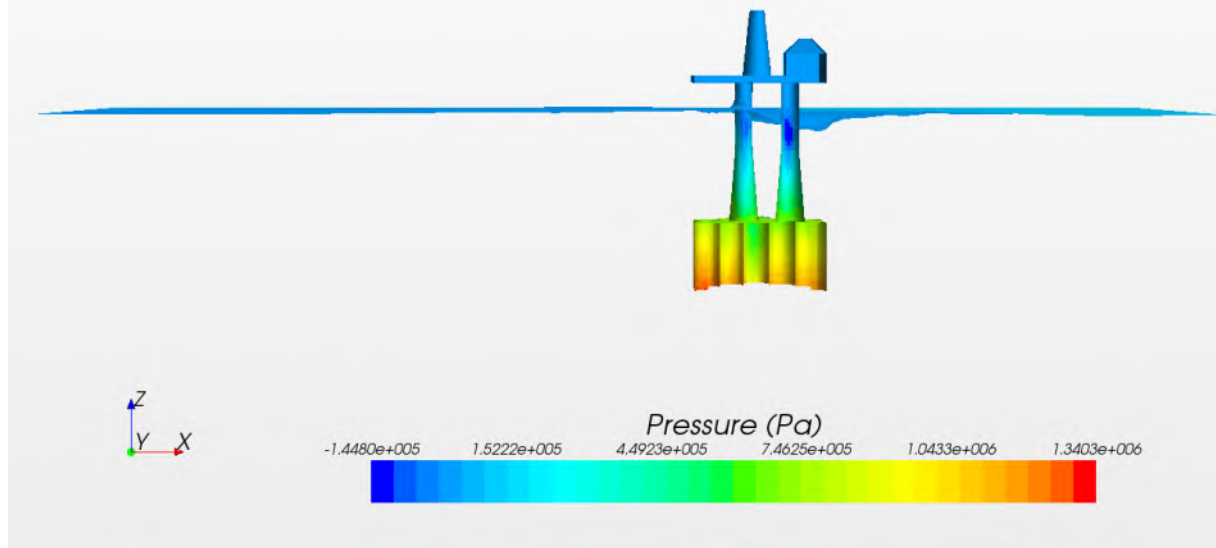


Figure32:Pressure Results in 8th second

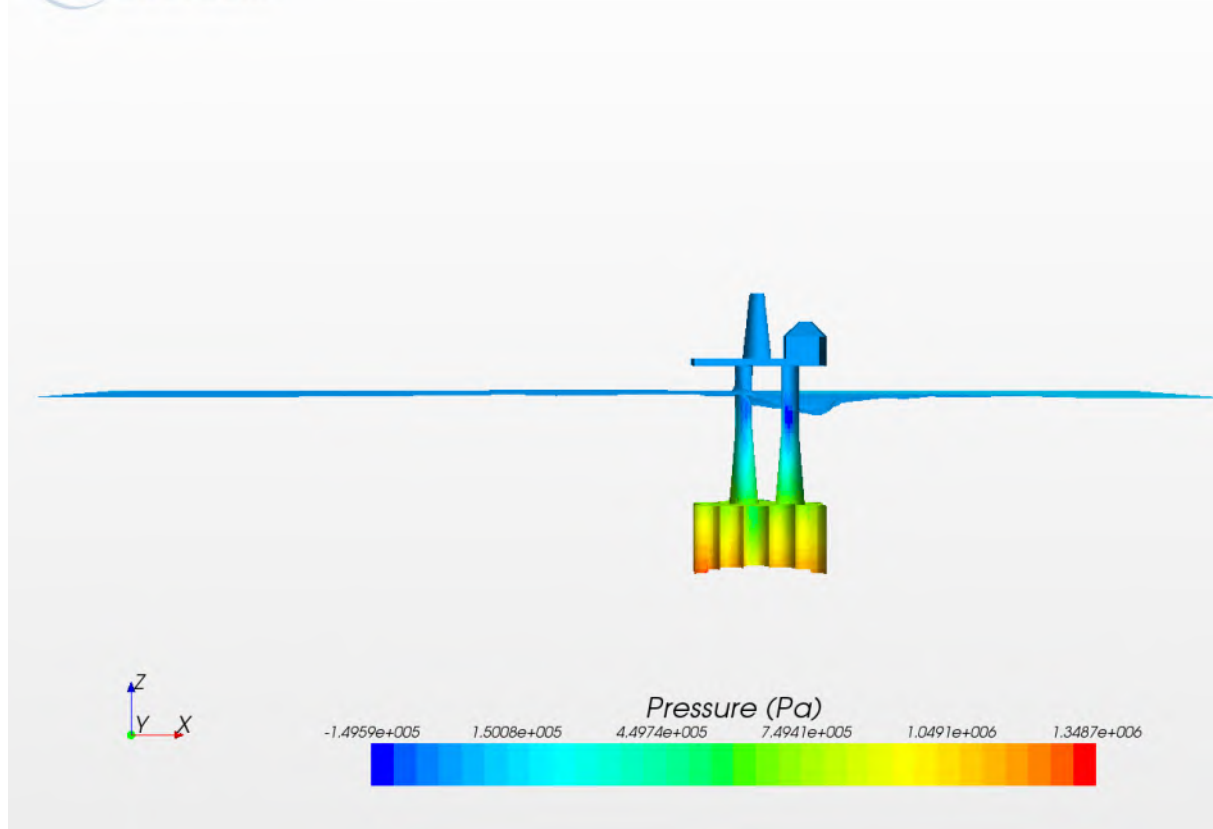


Figure33:Pressure Results in 9th second

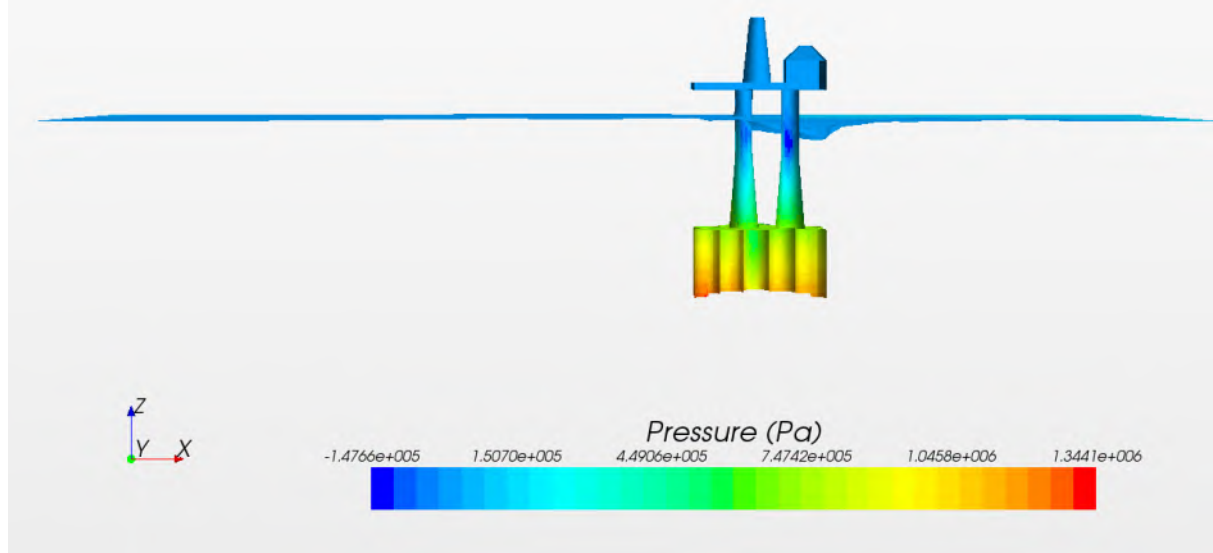


Figure34:Pressure Results in 10th second

7.1.3. Wall shear stresses

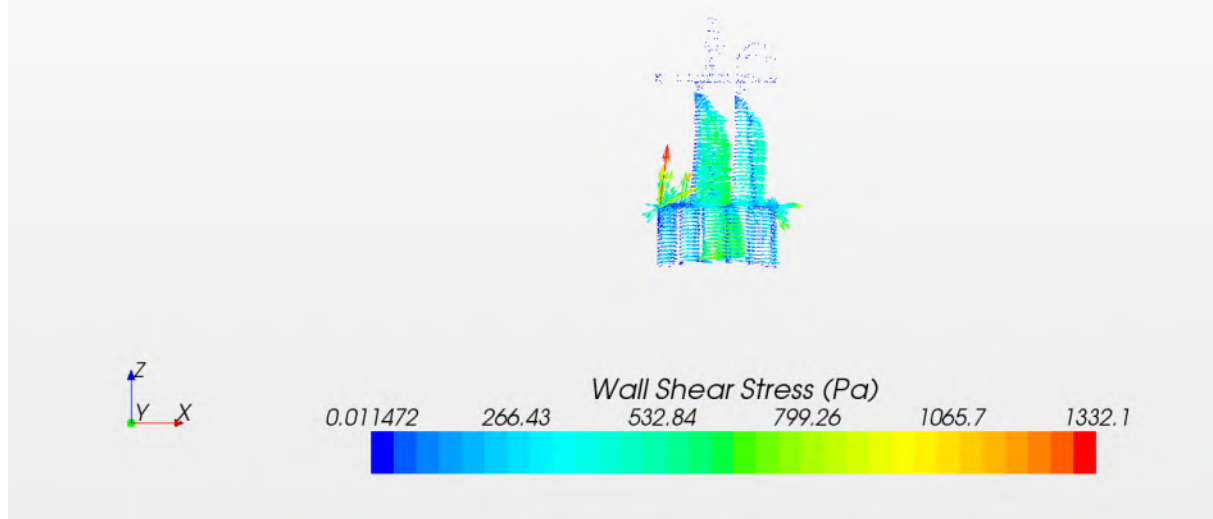


Figure35:Wall Shear Stress Results in 1st second

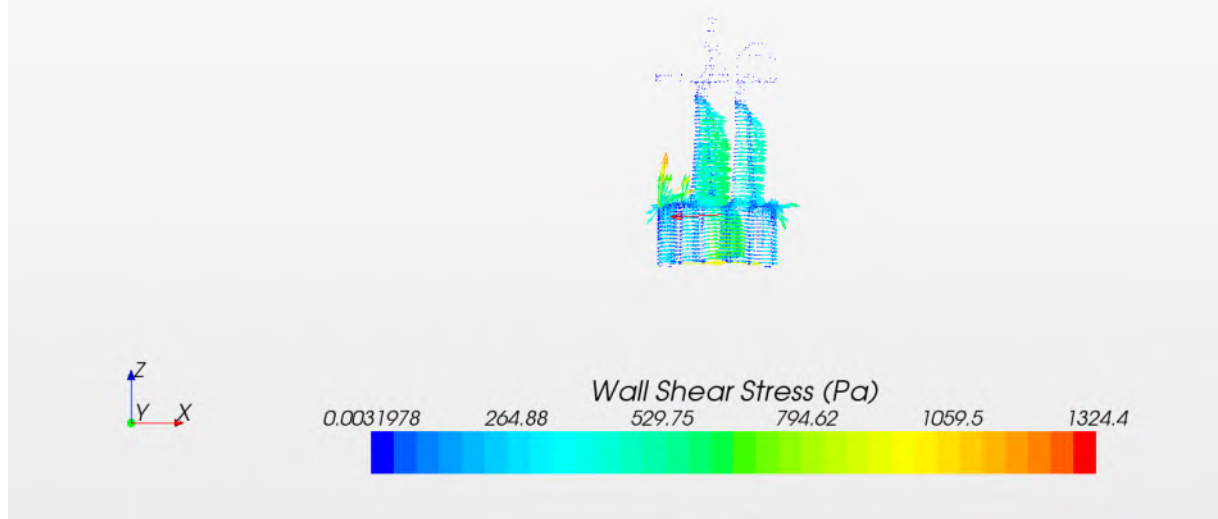


Figure36:Wall Shear Stress Results in 2nd second

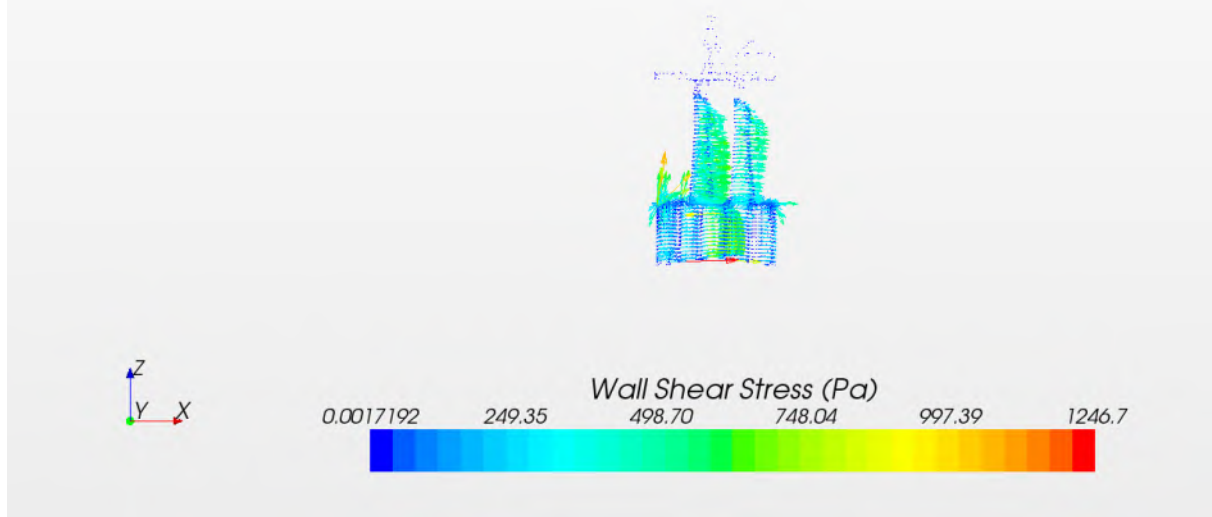


Figure37:Wall Shear Stress Results in 3rd second

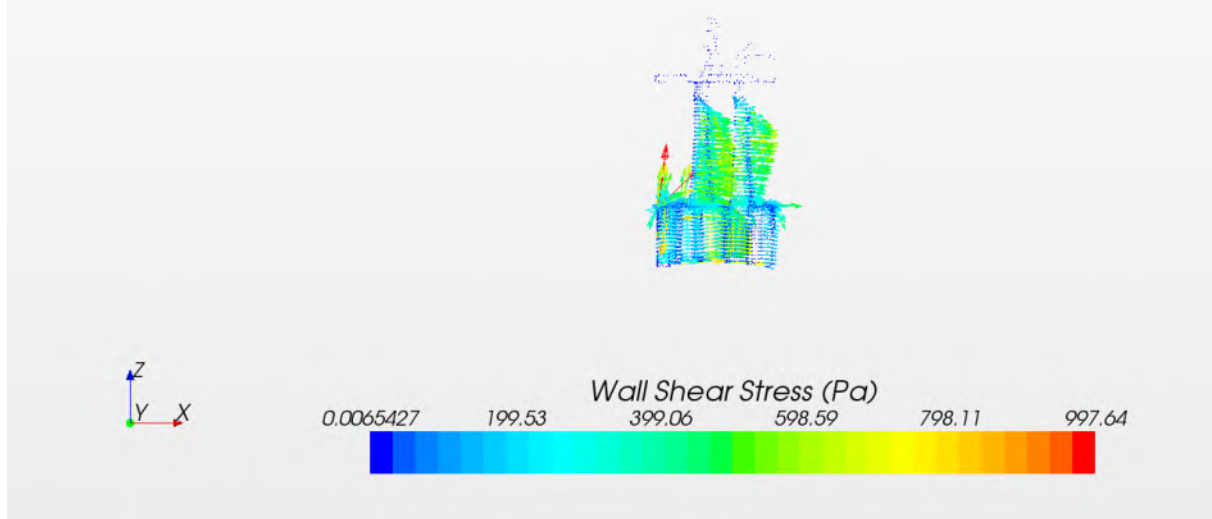


Figure38:Wall Shear Stress Results in 4th second

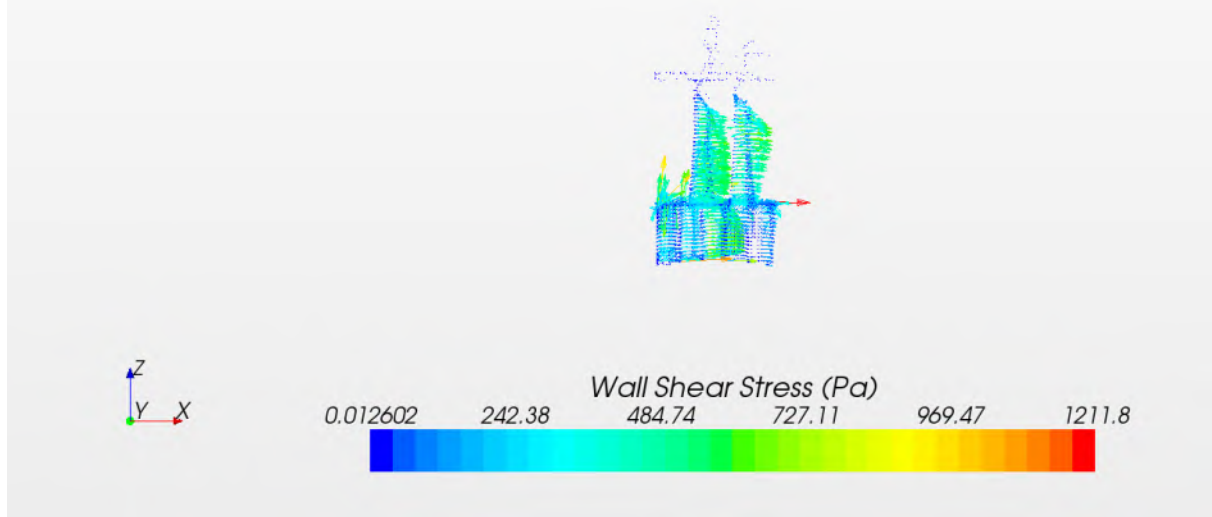


Figure39:Wall Shear Stress Results in 5th second

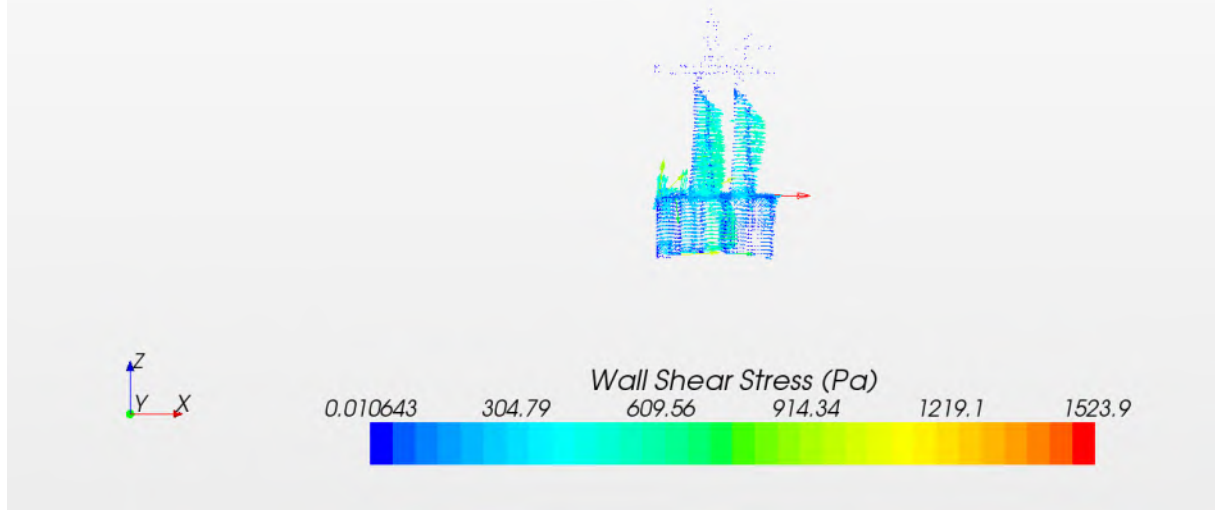


Figure40:Wall Shear Stress Results in 6th second

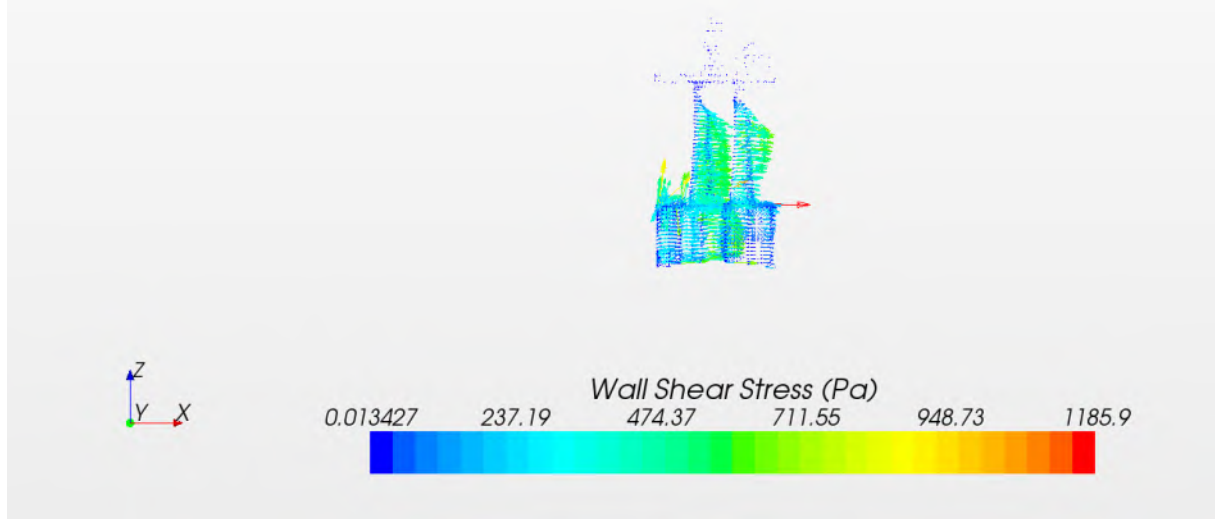


Figure41:Wall Shear Stress Results in 7th second

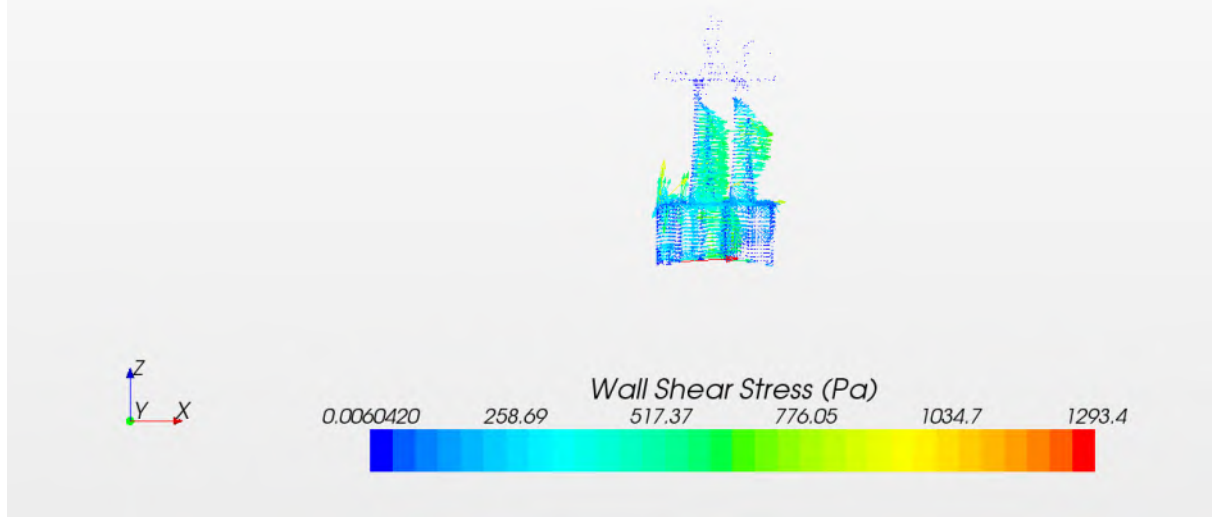


Figure42:Wall Shear Stress Results in 8th second

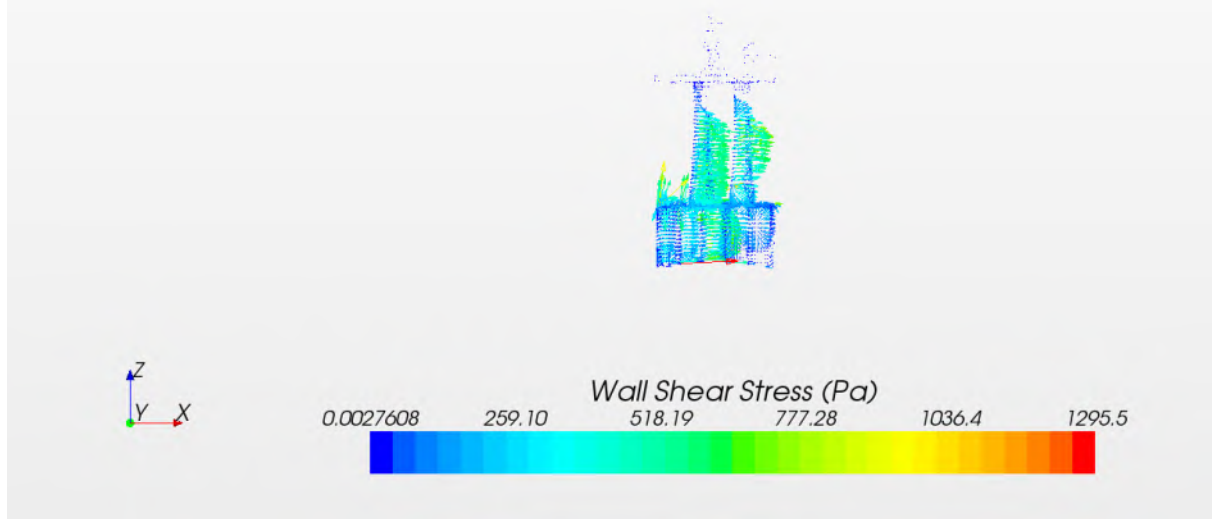


Figure43:Wall Shear Stress Results in 9th second

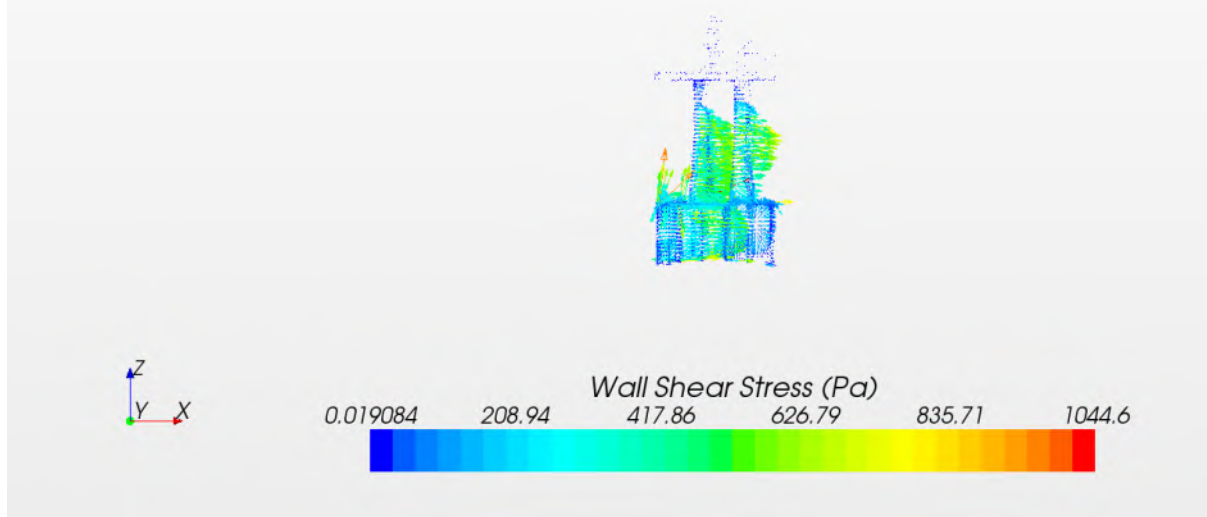


Figure44:Wall Shear Stress Results in 10th second

7.2. Full Model

7.2.1. Velocity

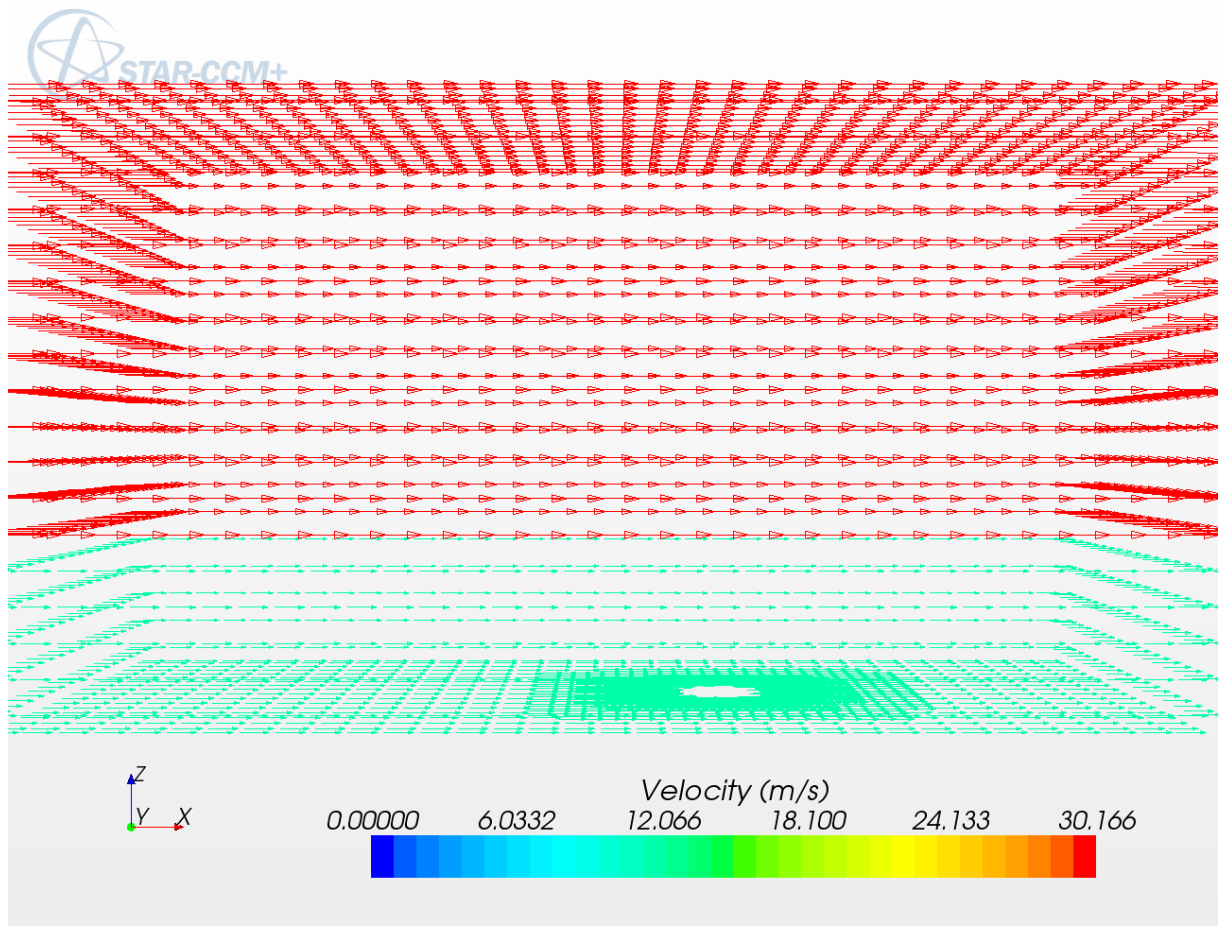


Figure45:Velocity Results in 1st second

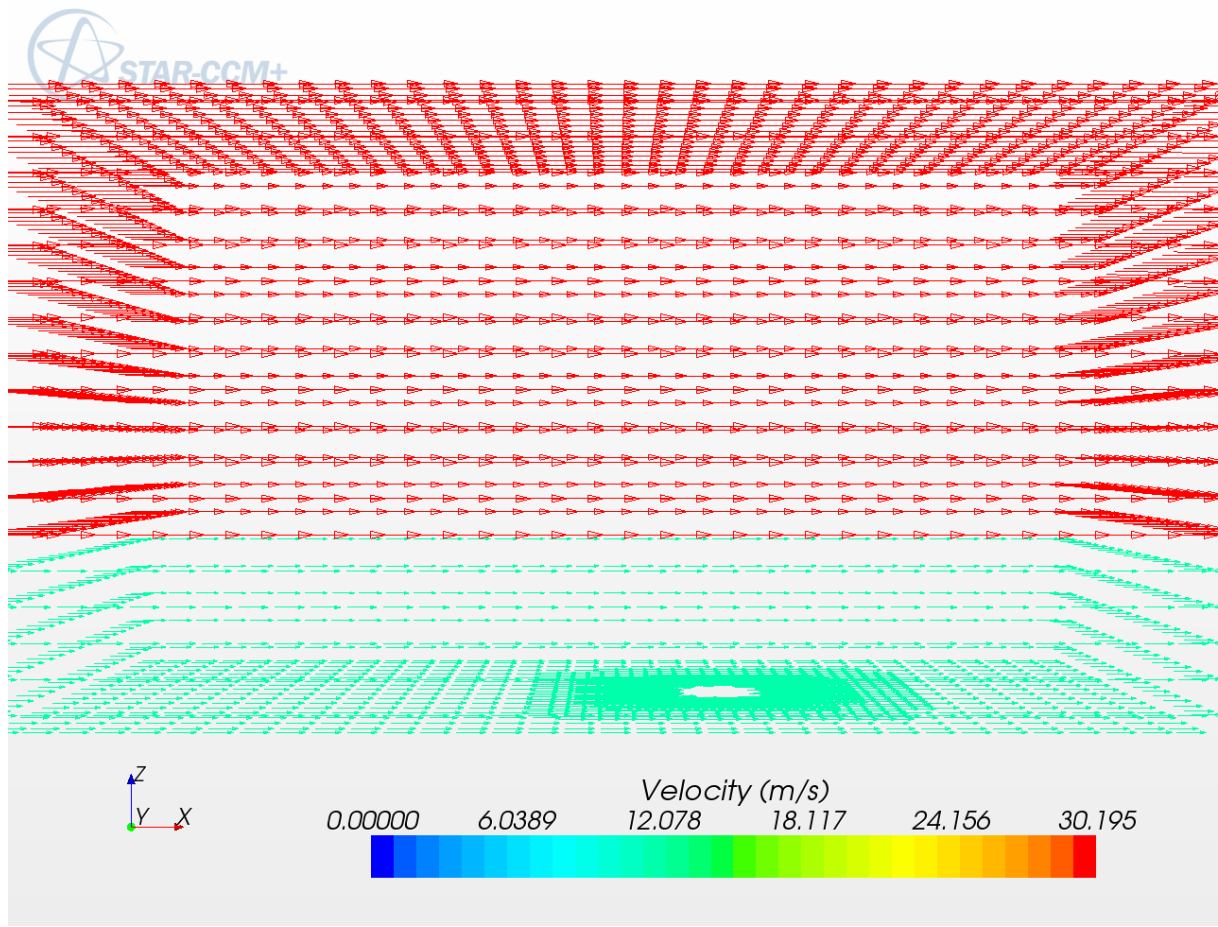


Figure46:Velocity Results in 2nd second

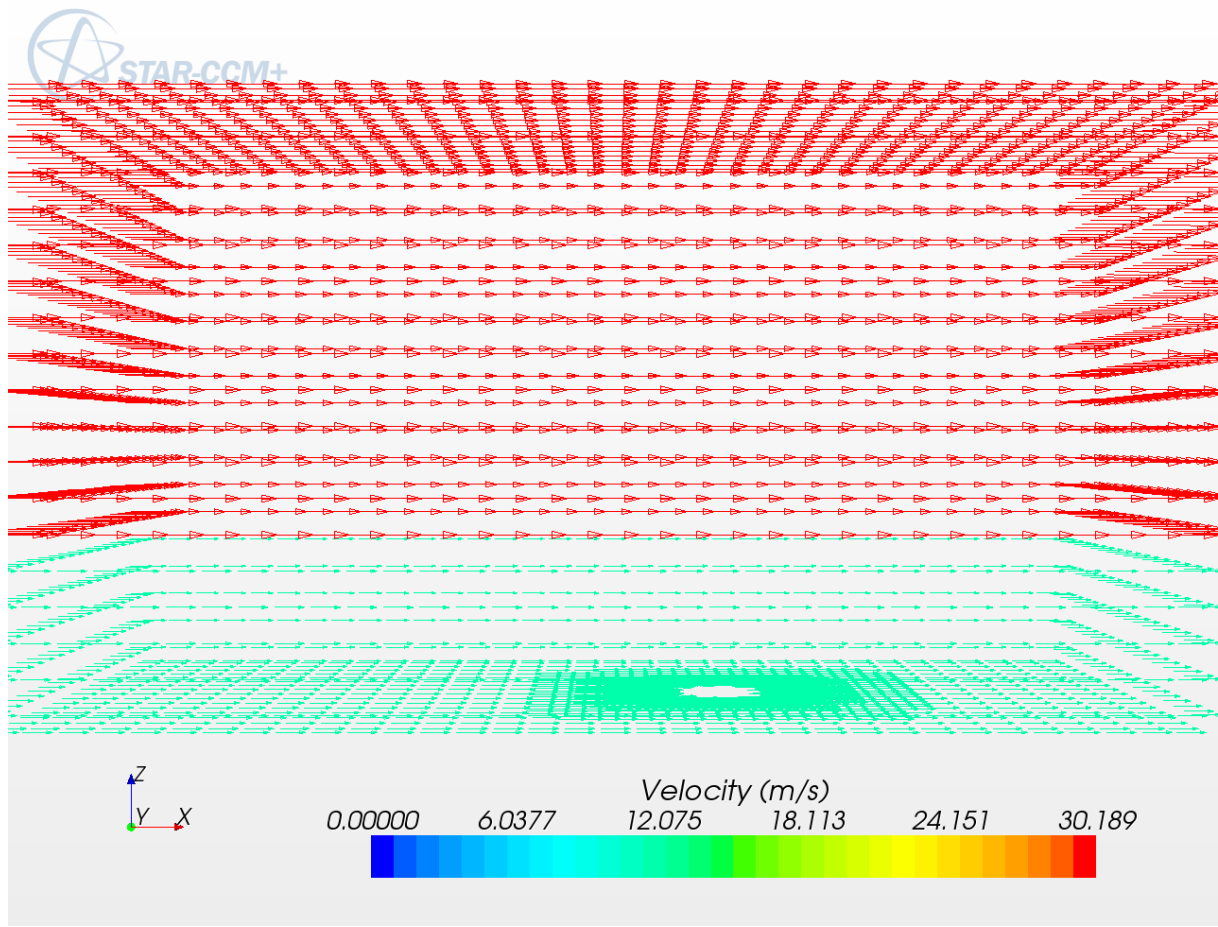


Figure47:Velocity Results in 3nd second

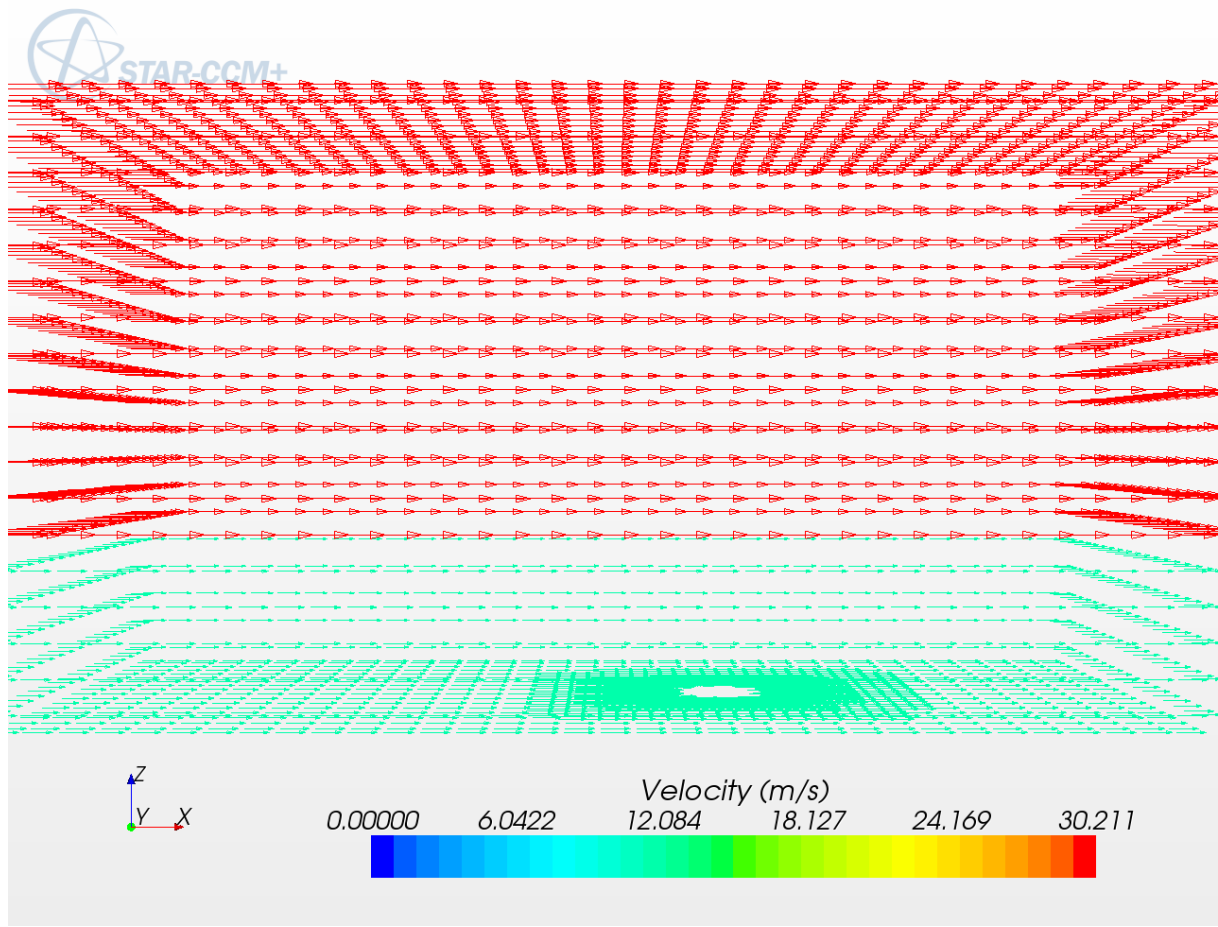


Figure47:Velocity Results in 4th second

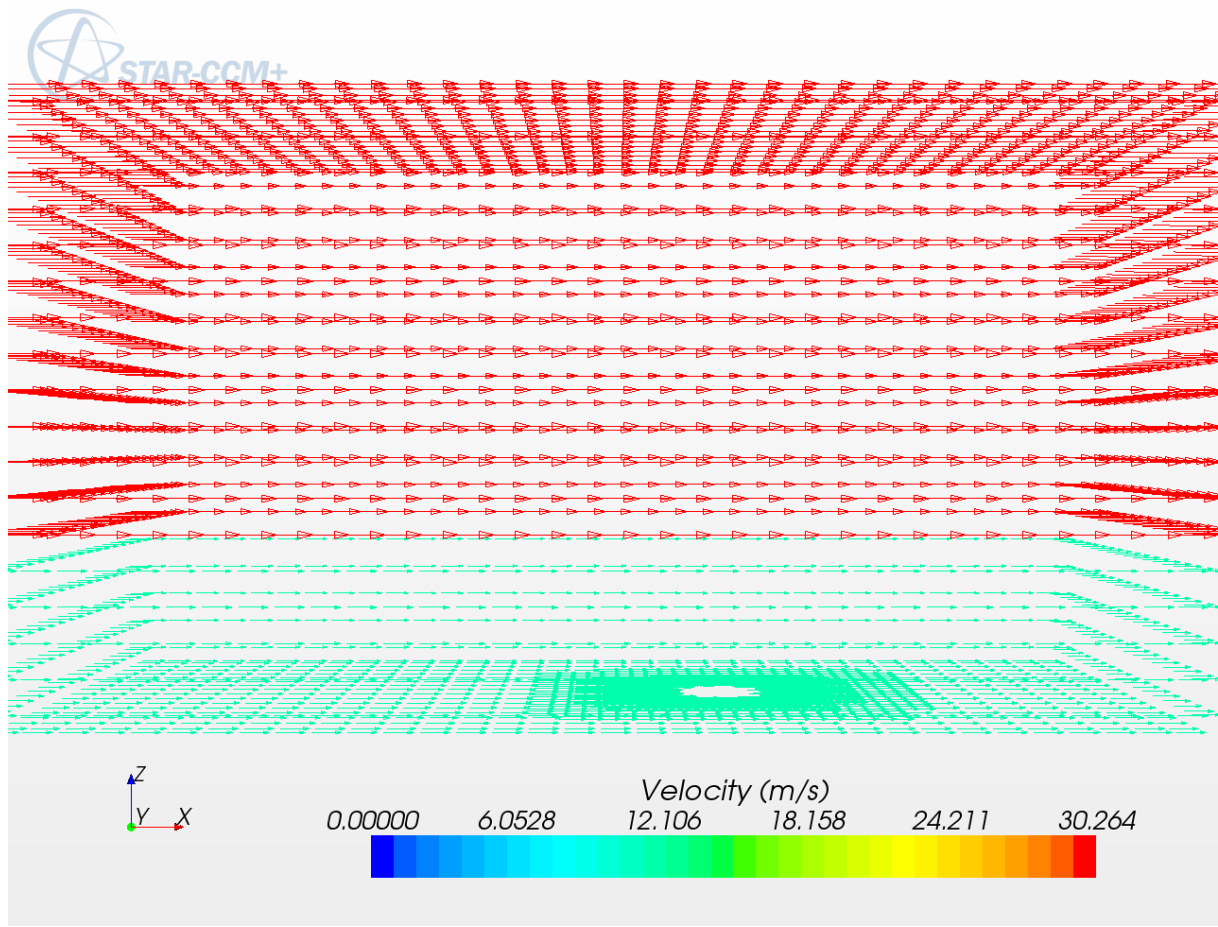


Figure48:Velocity Results in 5th second

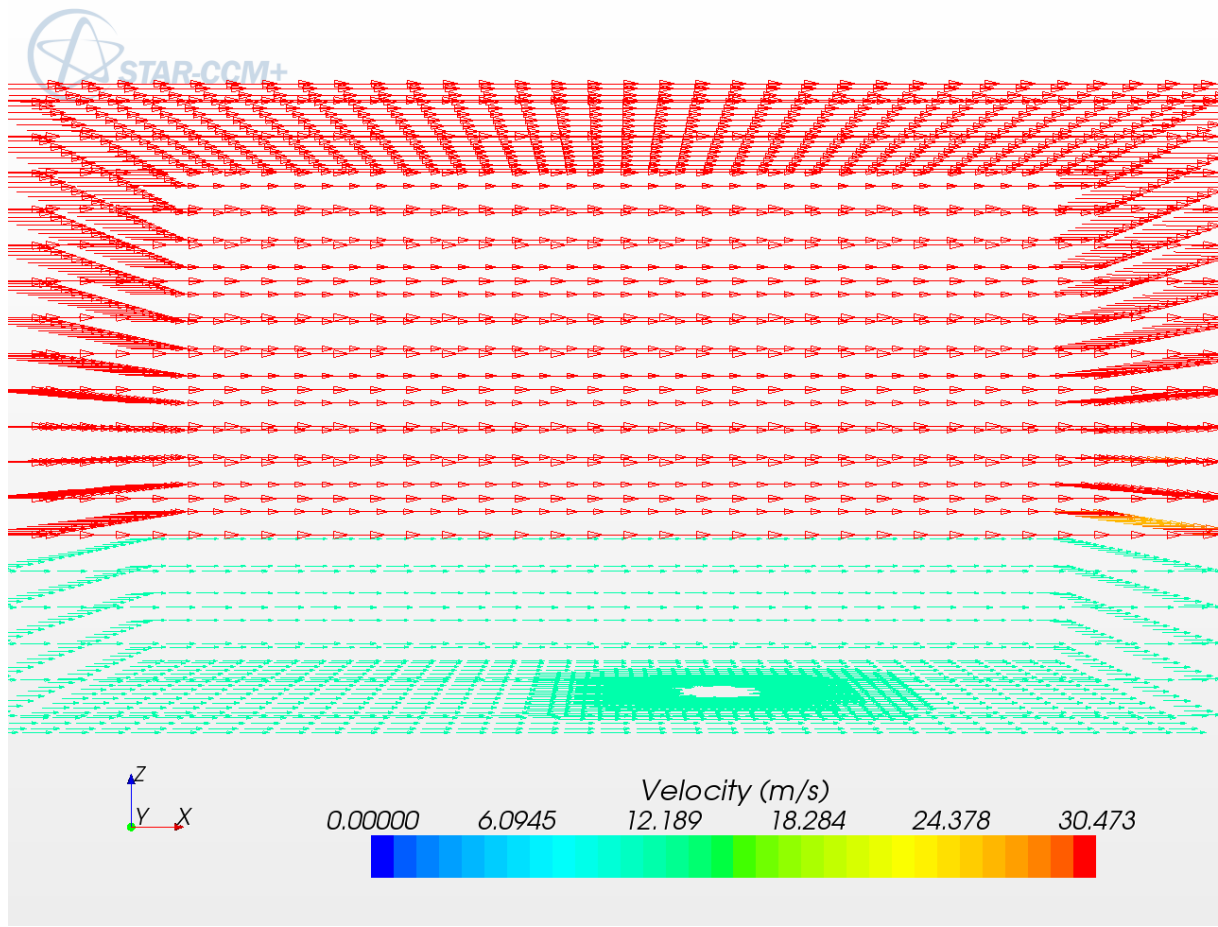


Figure49:Velocity Results in 6th second

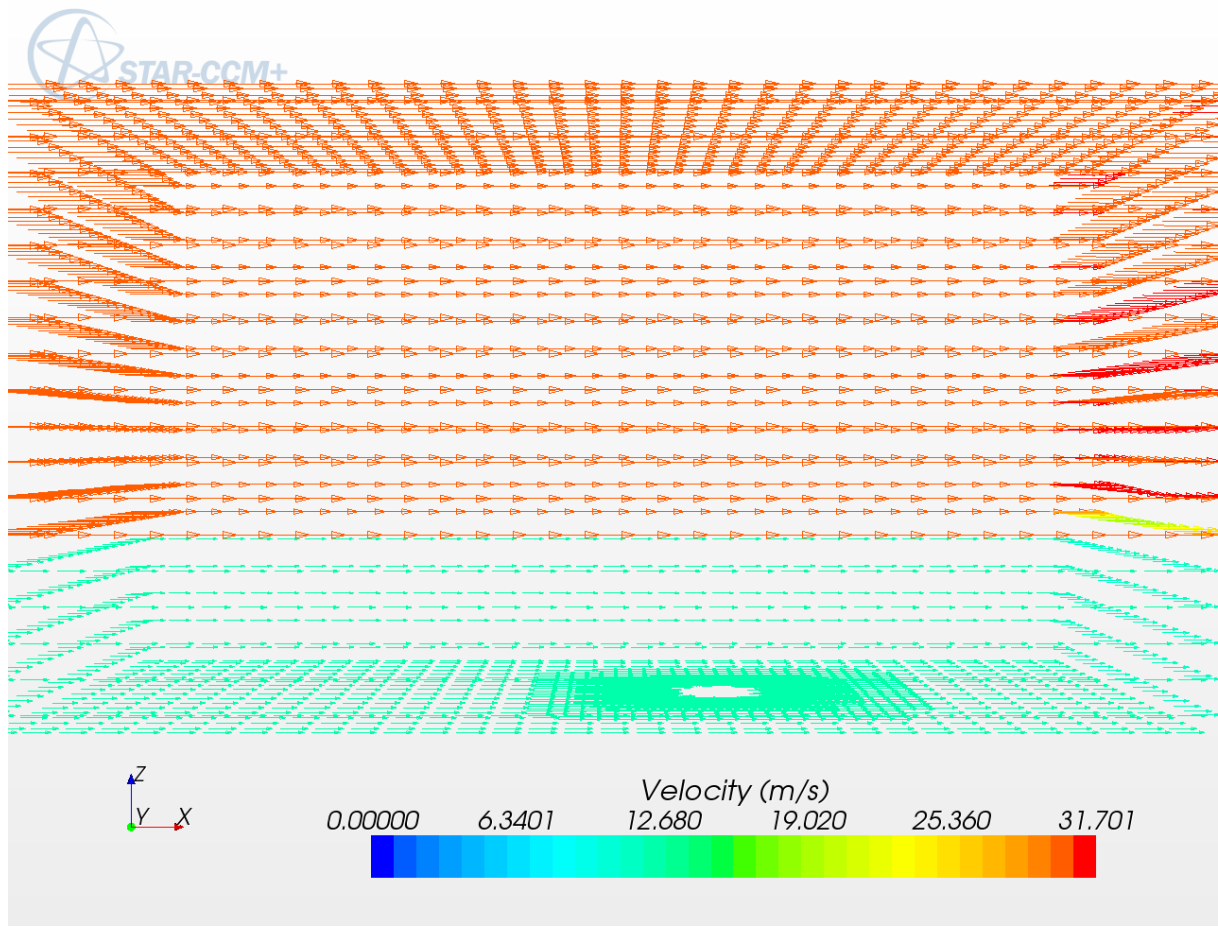


Figure50:Velocity Results in 7th second

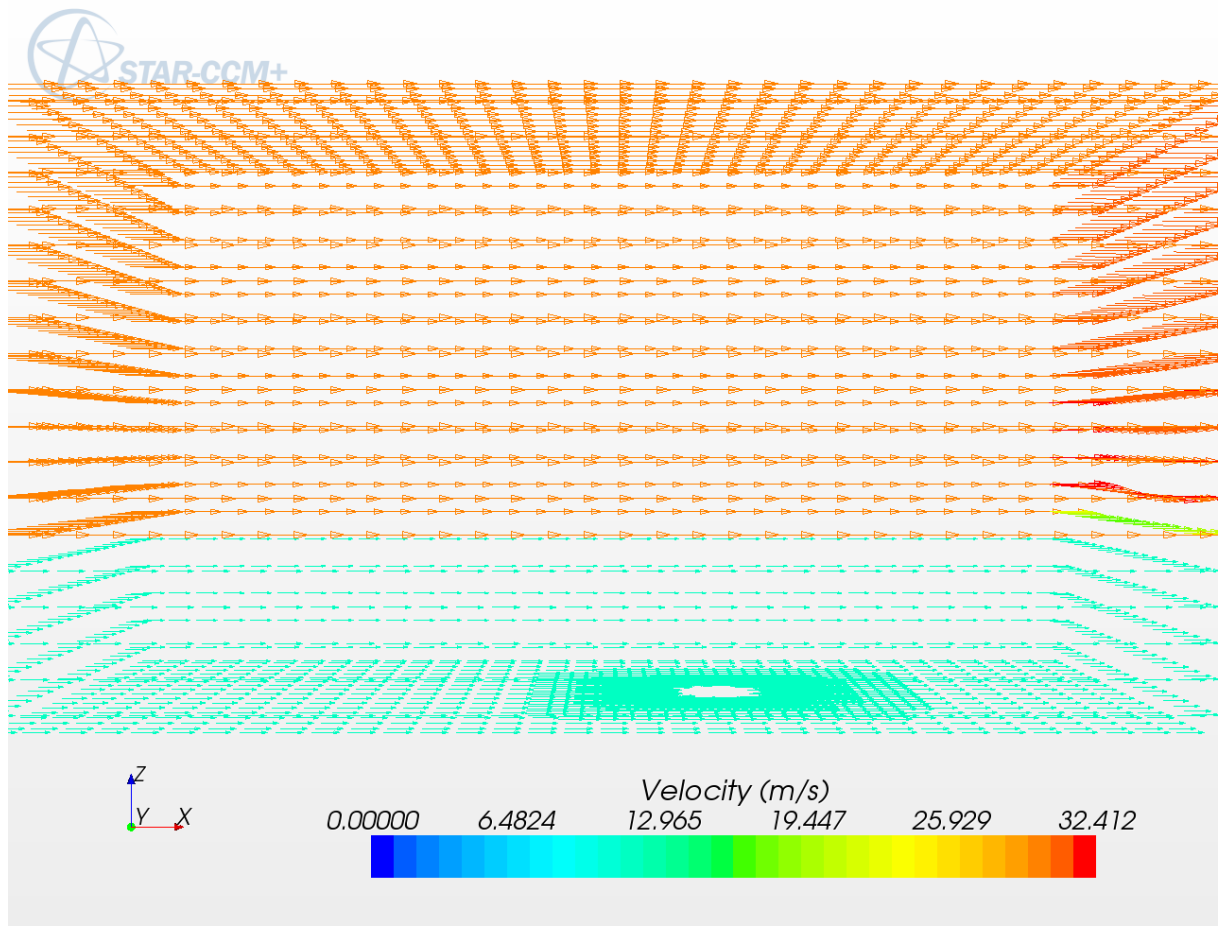


Figure51:Velocity Results in 8th second

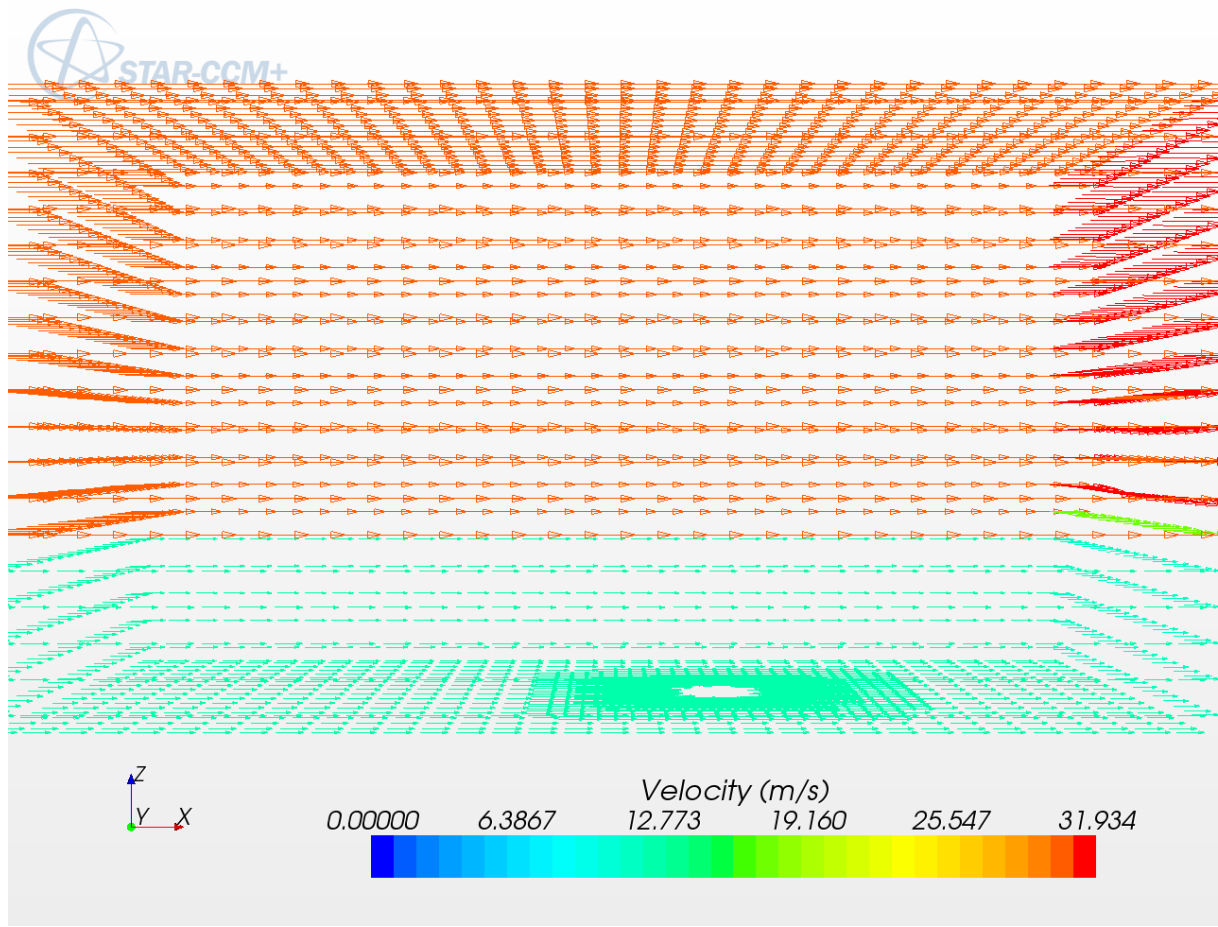


Figure52:Velocity Results in 9th second

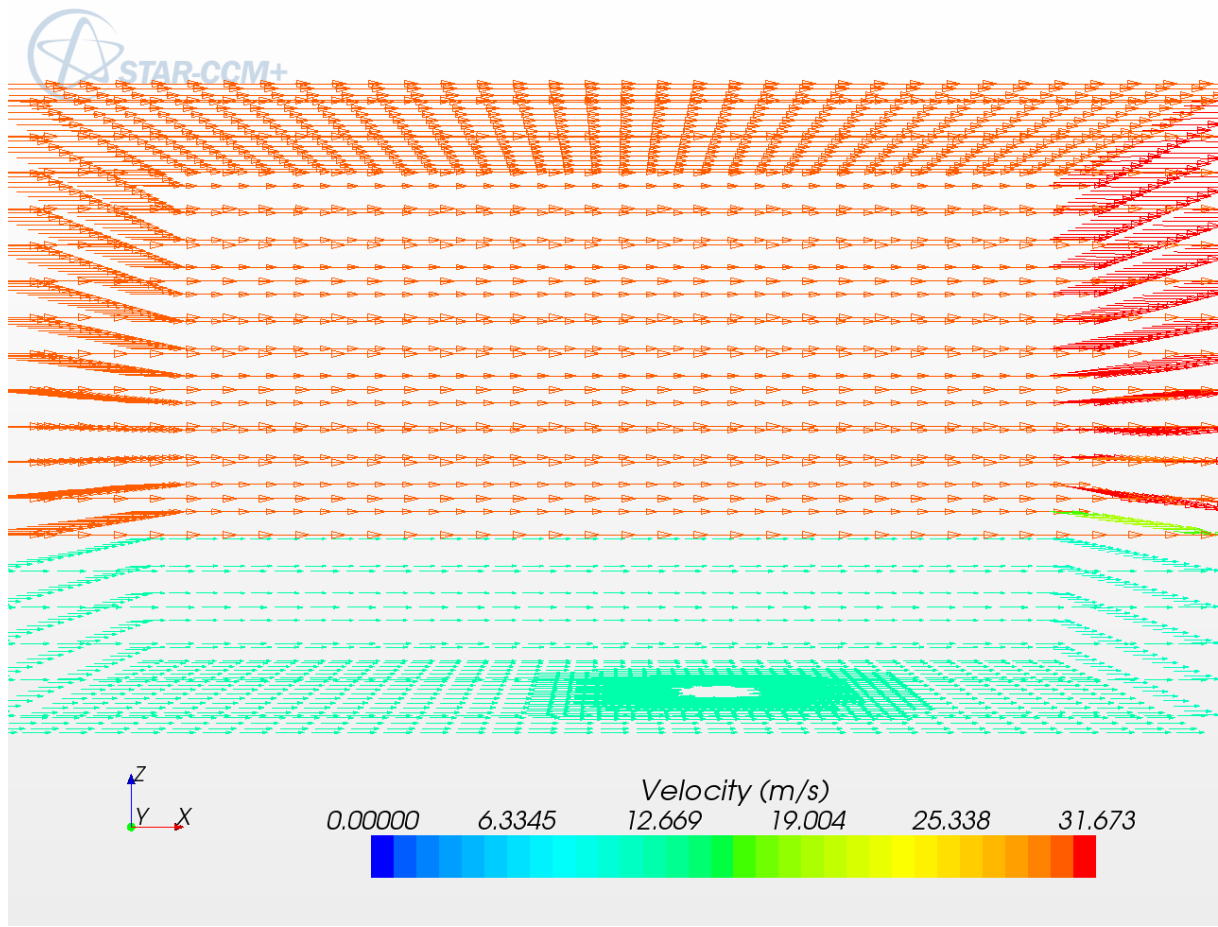


Figure53:Velocity Results in 10th second

7.2.2. Pressure

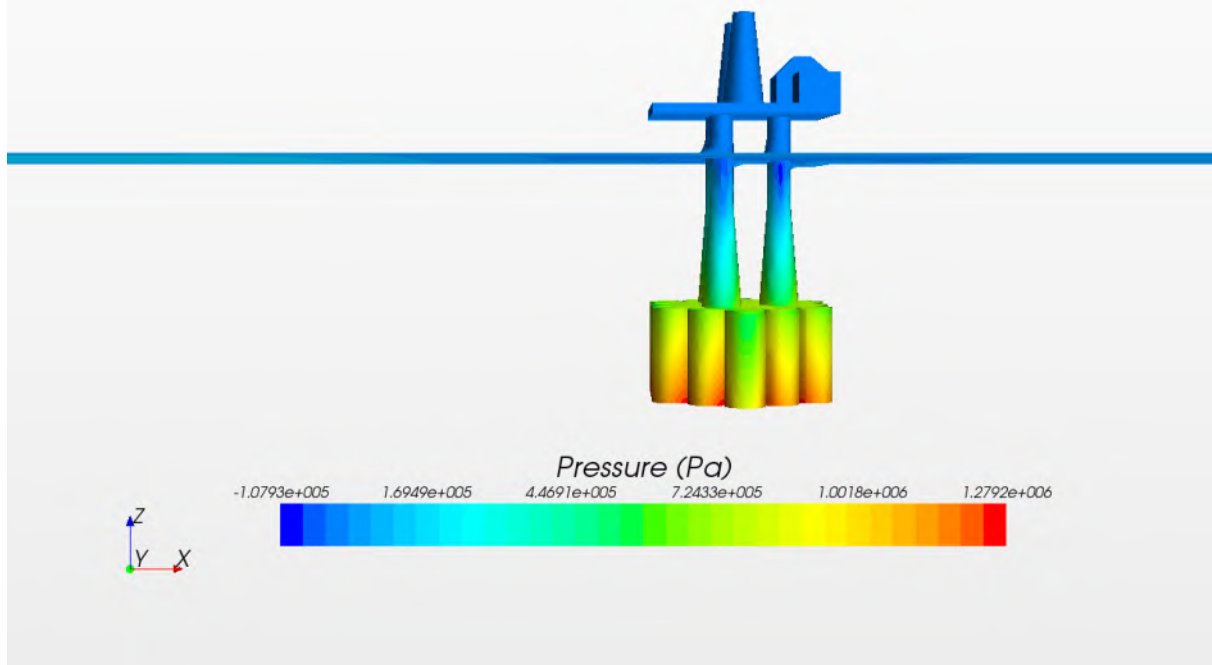


Figure54:Pressure Results in 1st second

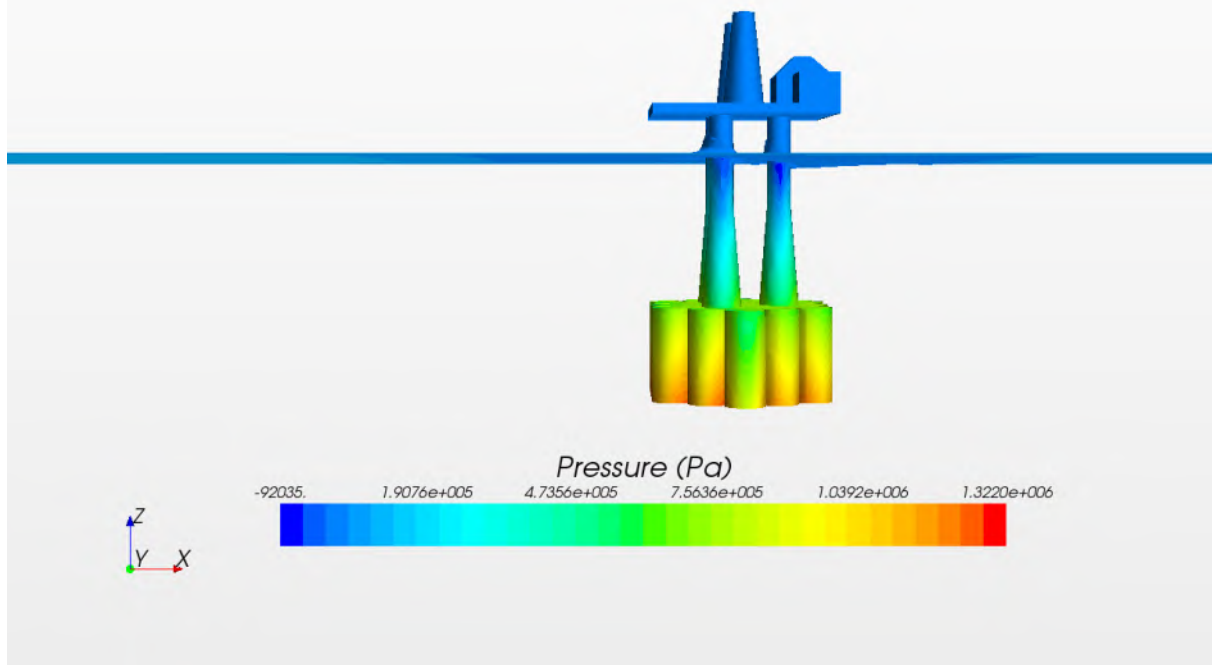


Figure55:Pressure Results in 2nd second

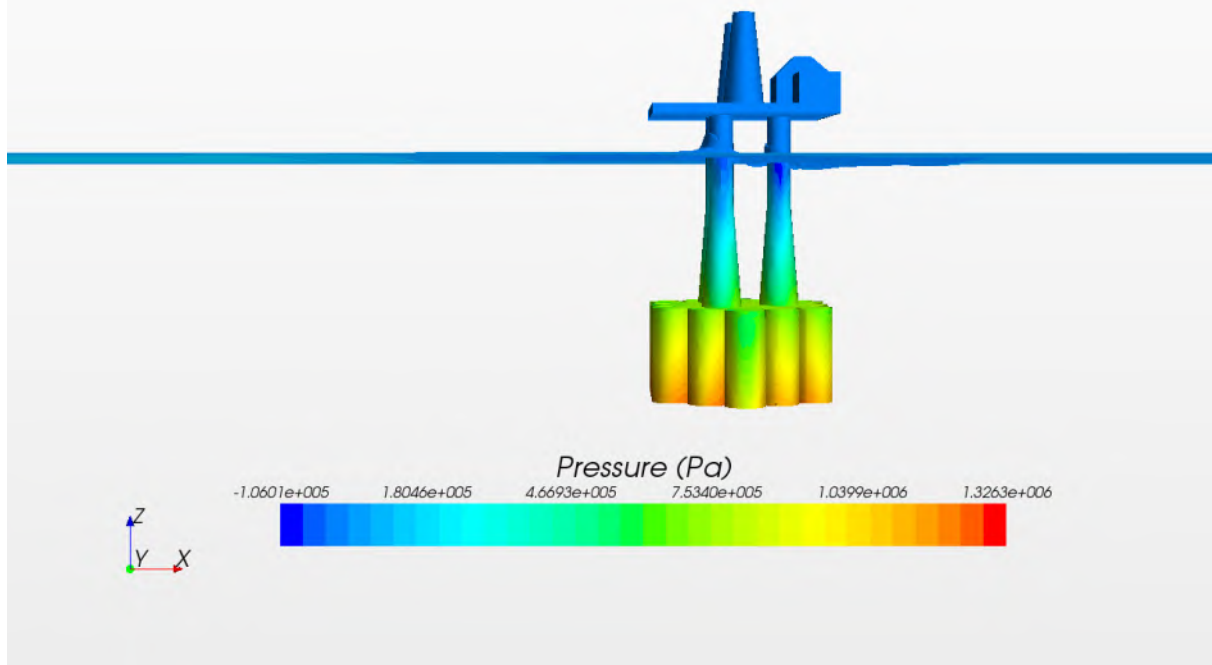


Figure56:Pressure Results in 3rd second

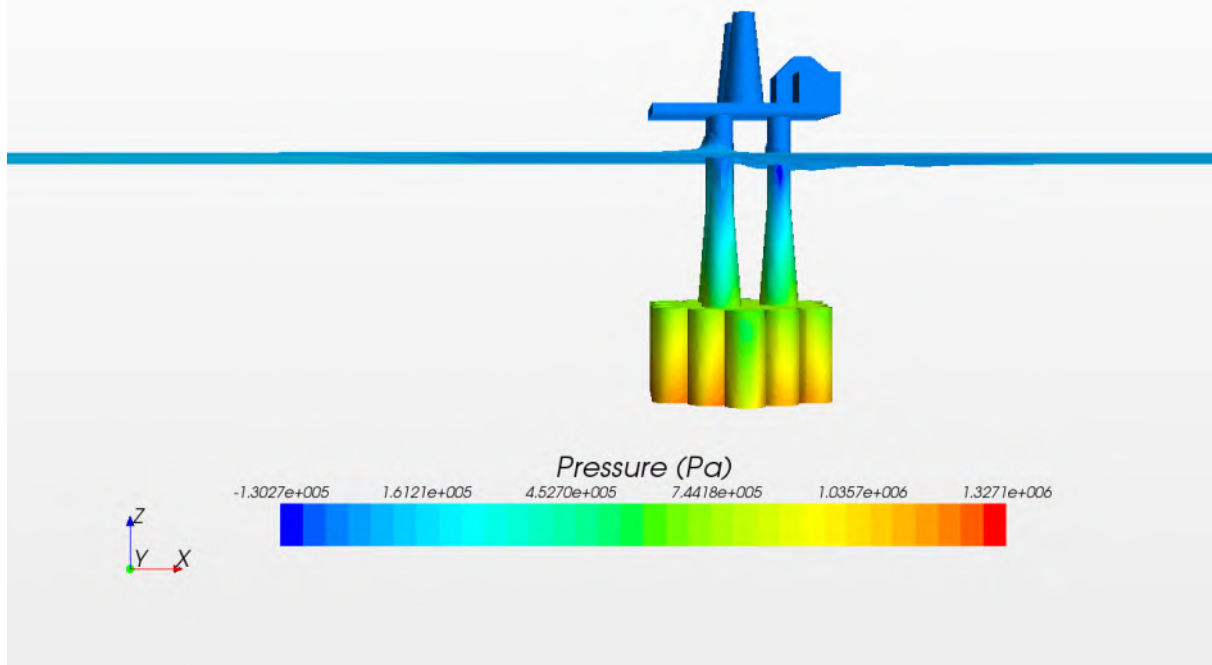


Figure57:Pressure Results in 4th second

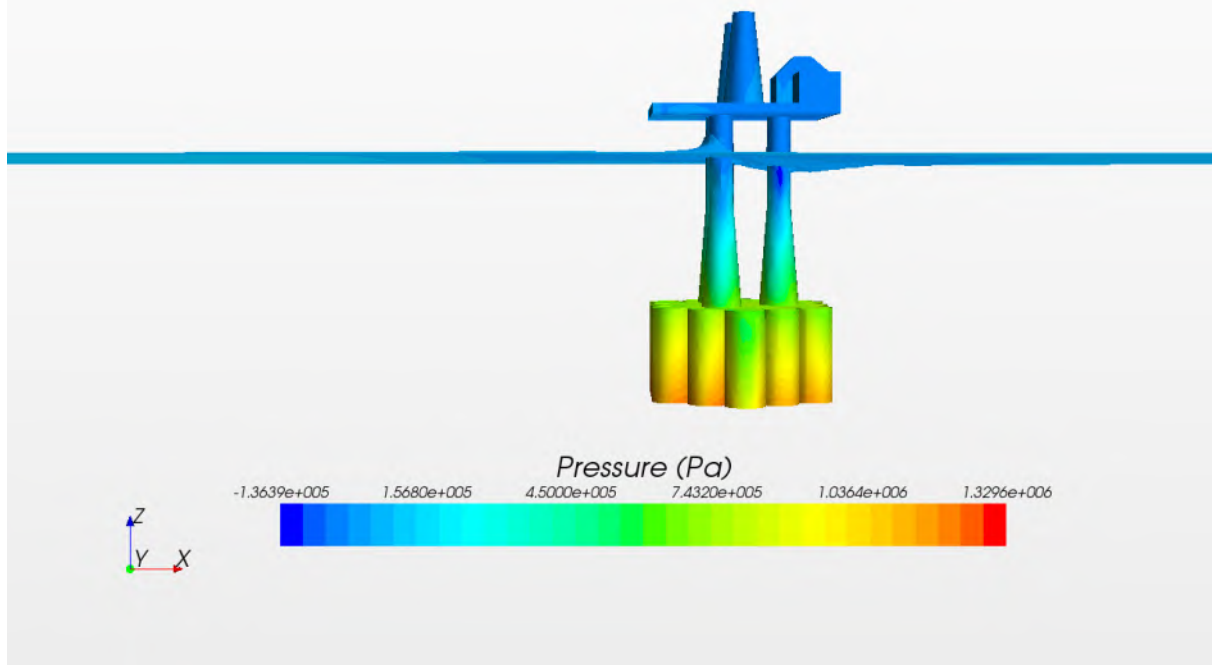


Figure58:Pressure Results in 5th second

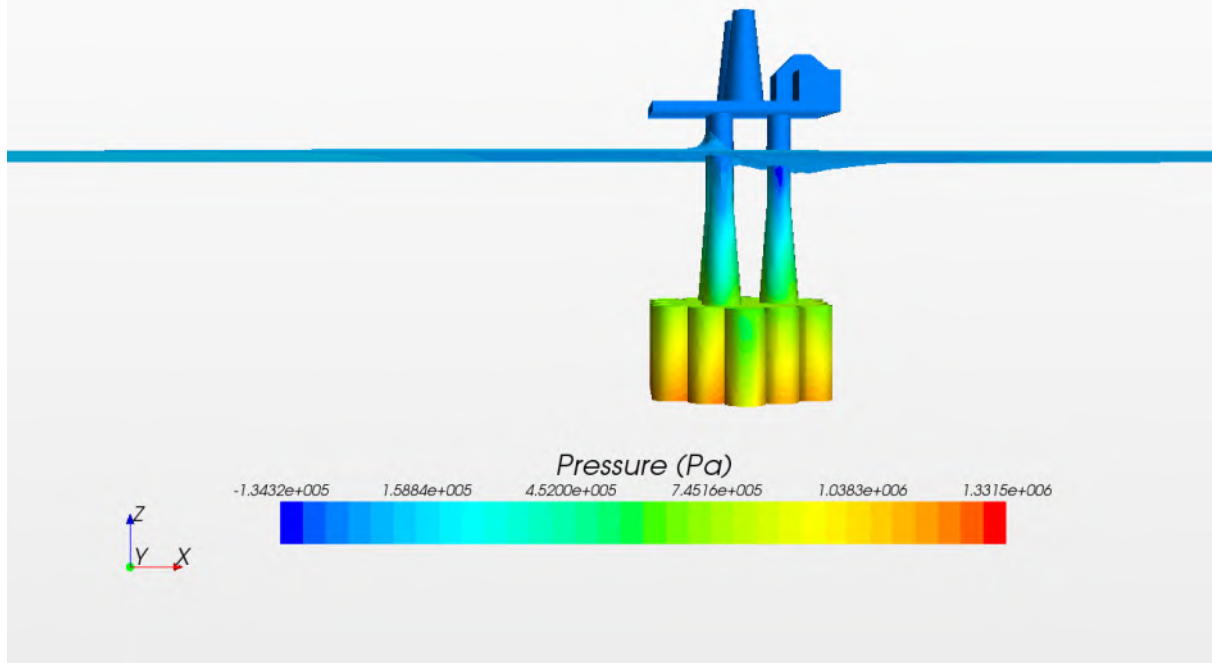


Figure59:Pressure Results in 6th second

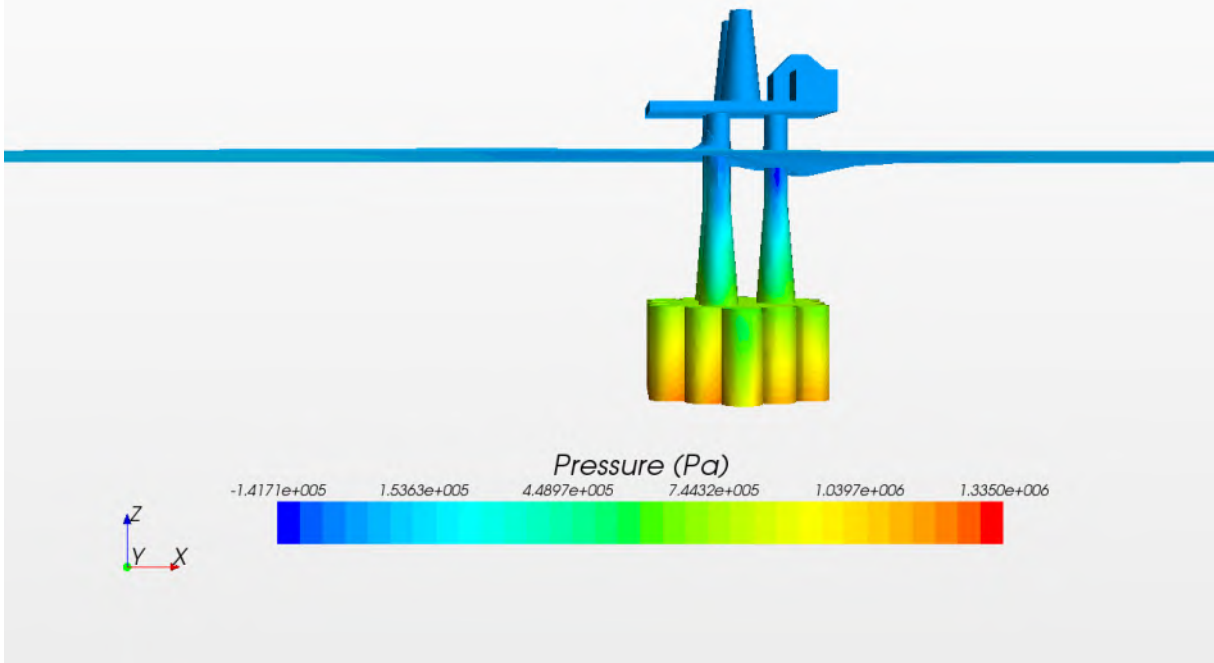


Figure60:Pressure Results in 7th second

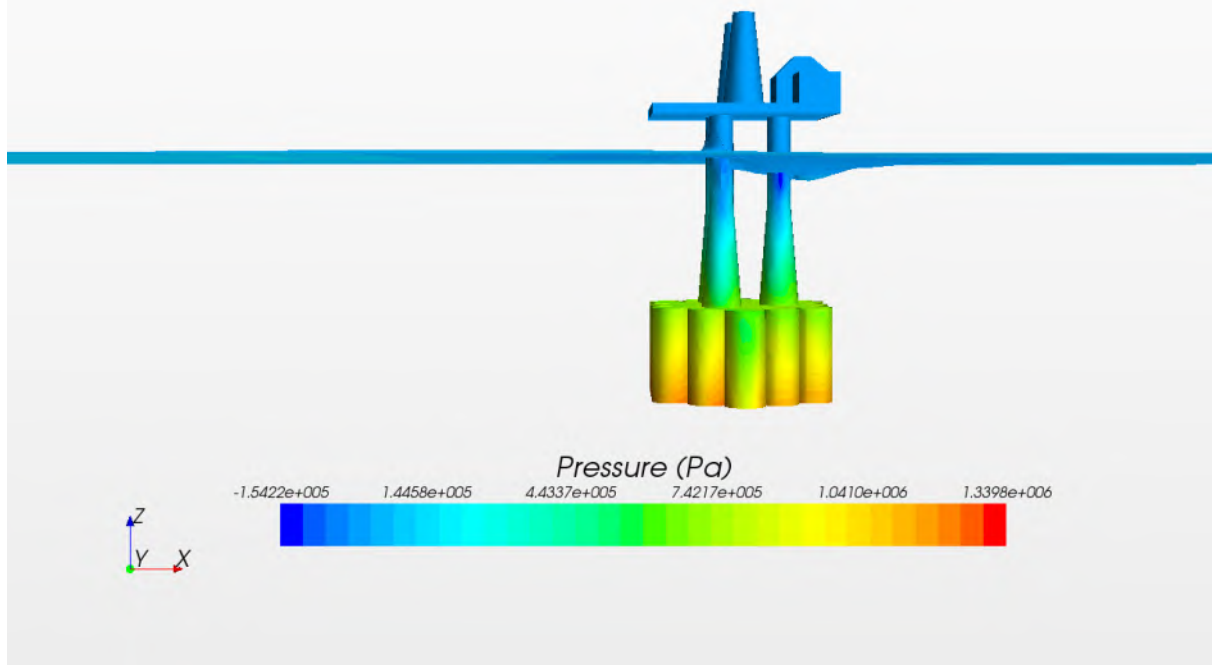


Figure61:Pressure Results in 8th second

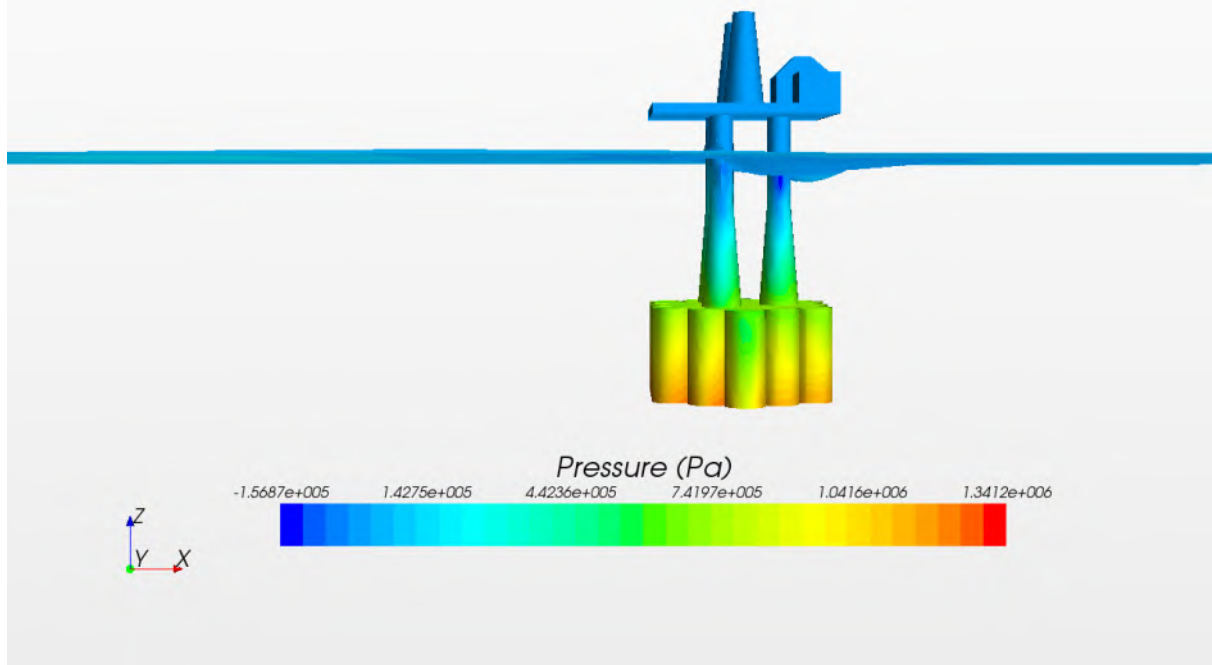


Figure62:Pressure Results in 9th second

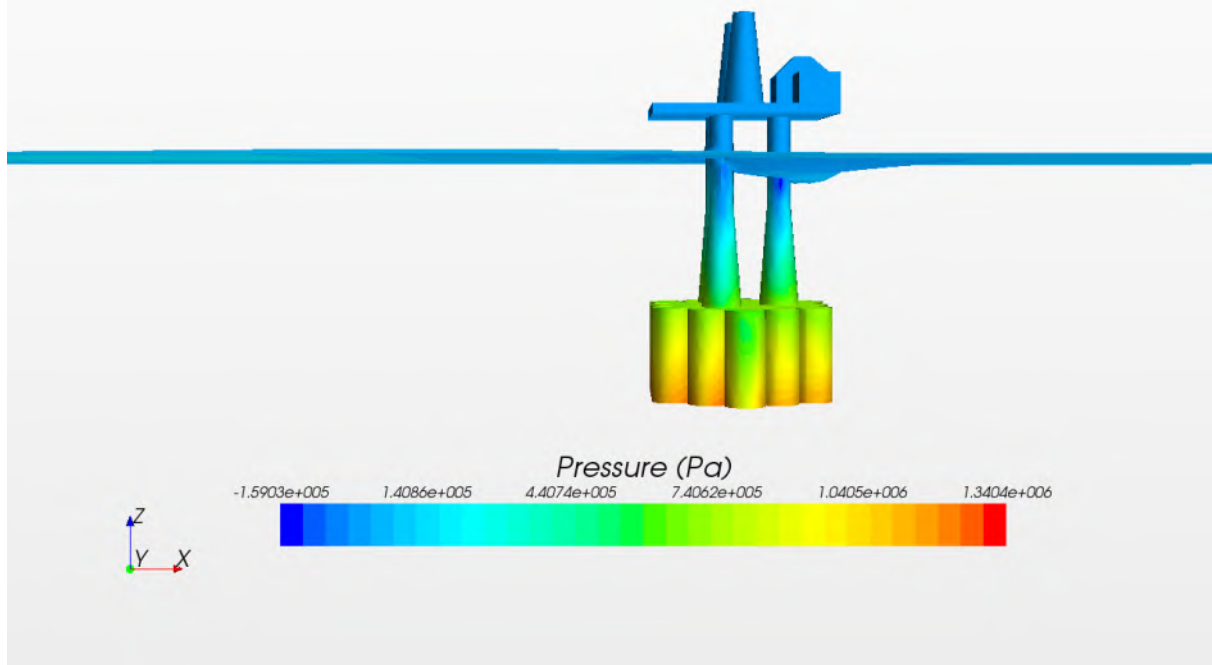


Figure63:Pressure Results in 10th second

7.2.3. Wall Shear Stresses:

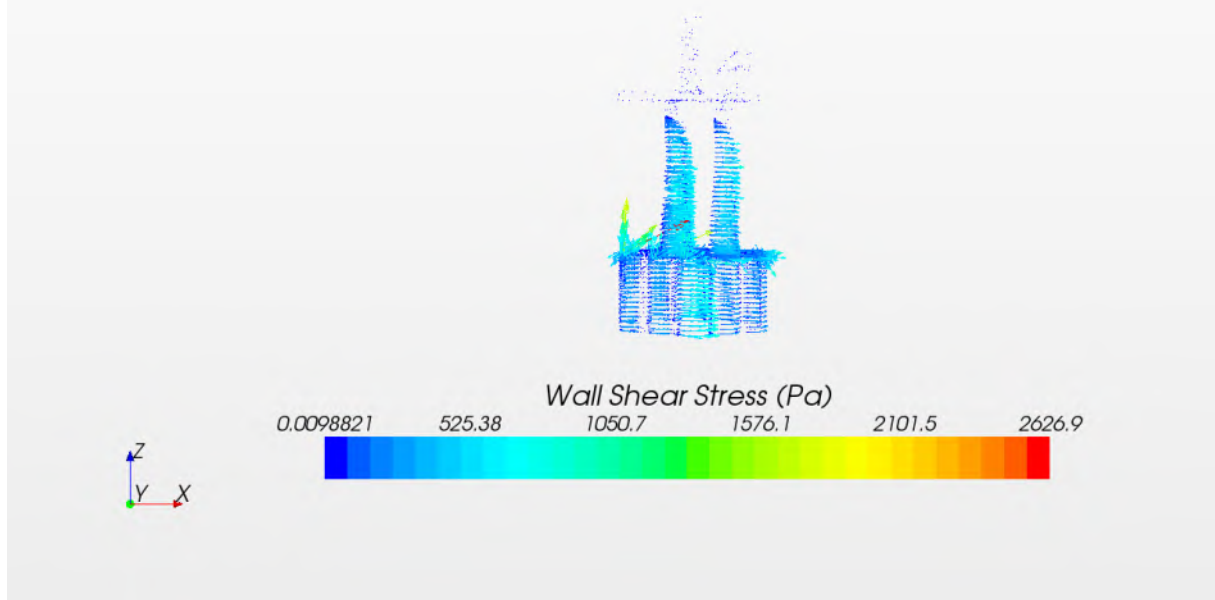


Figure64:Wall Shear Stress Results in 1st second

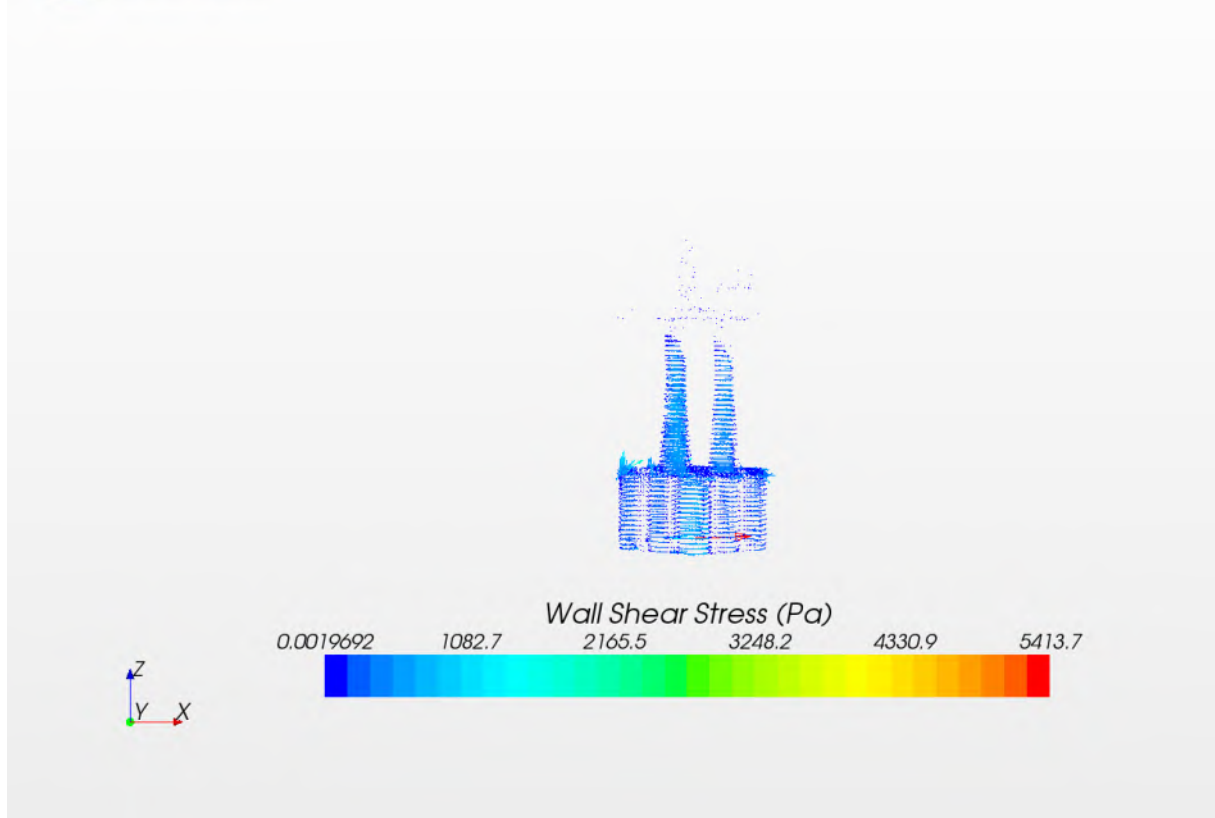


Figure65:Wall Shear Stress Results in 2nd second

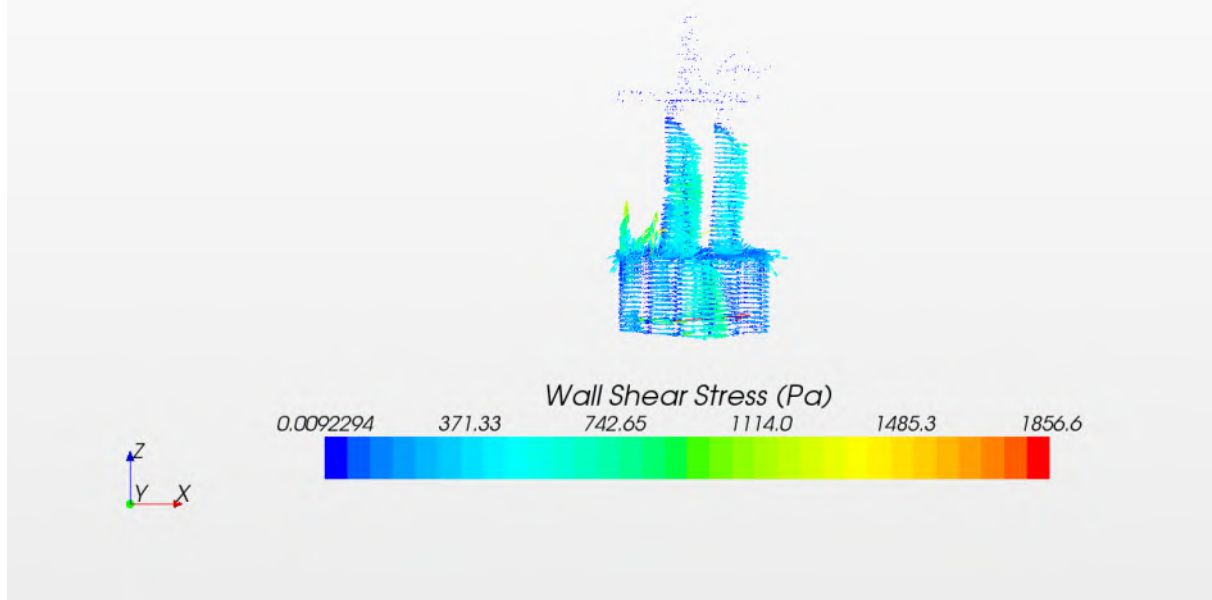


Figure66:Wall Shear Stress Results in 3rd second

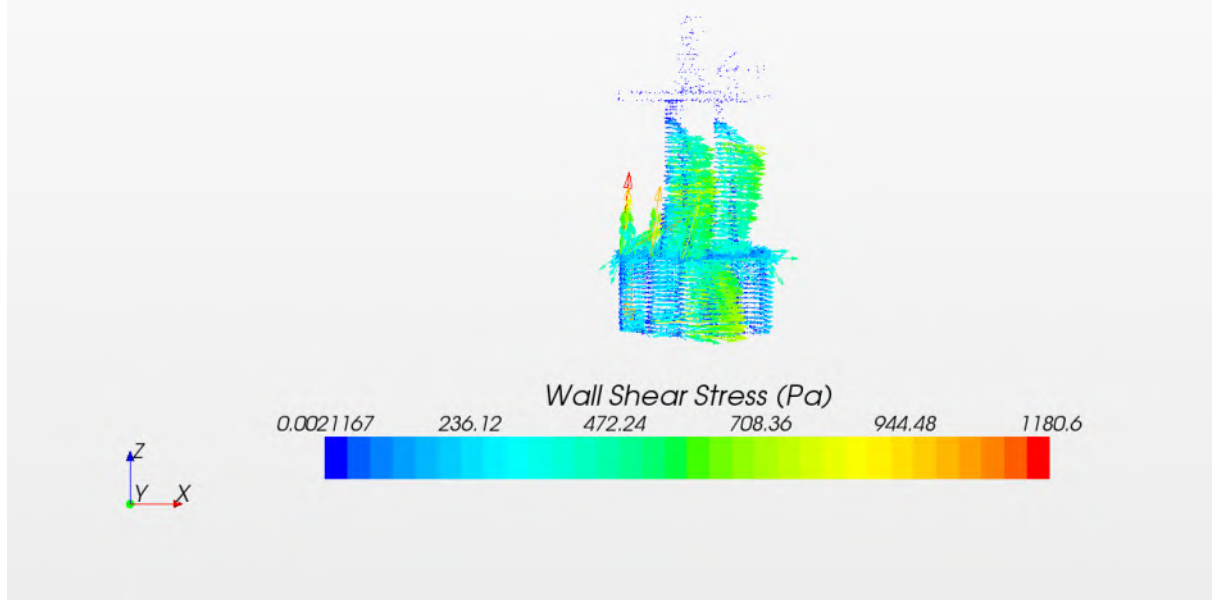


Figure67:Wall Shear Stress Results in 4th second

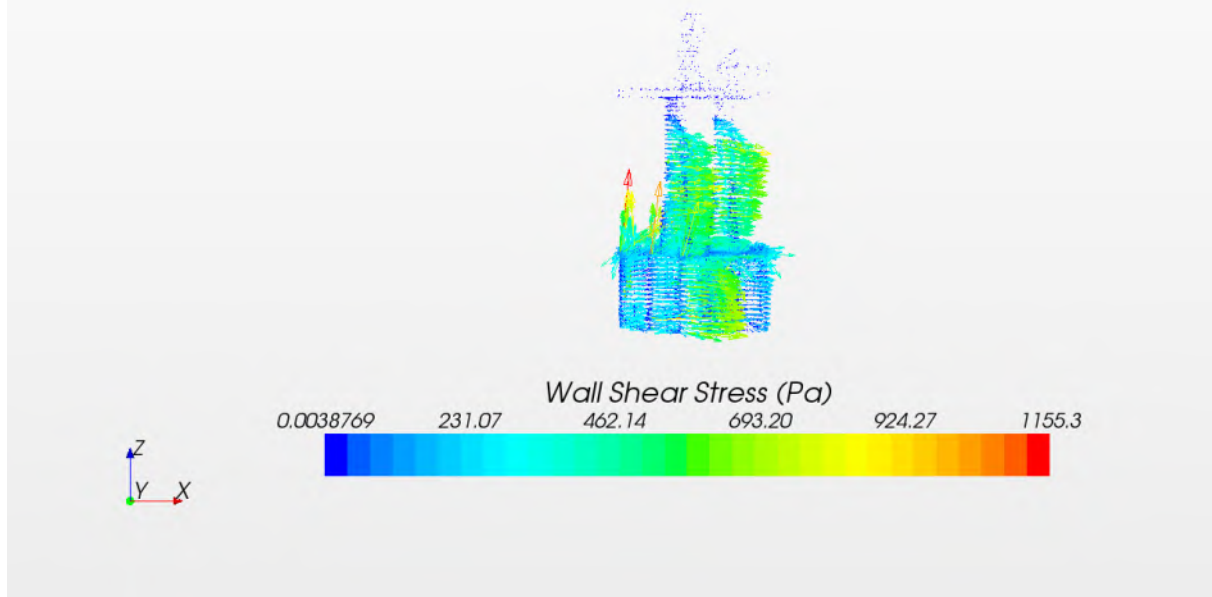


Figure68:Wall Shear Stress Results in 5th second

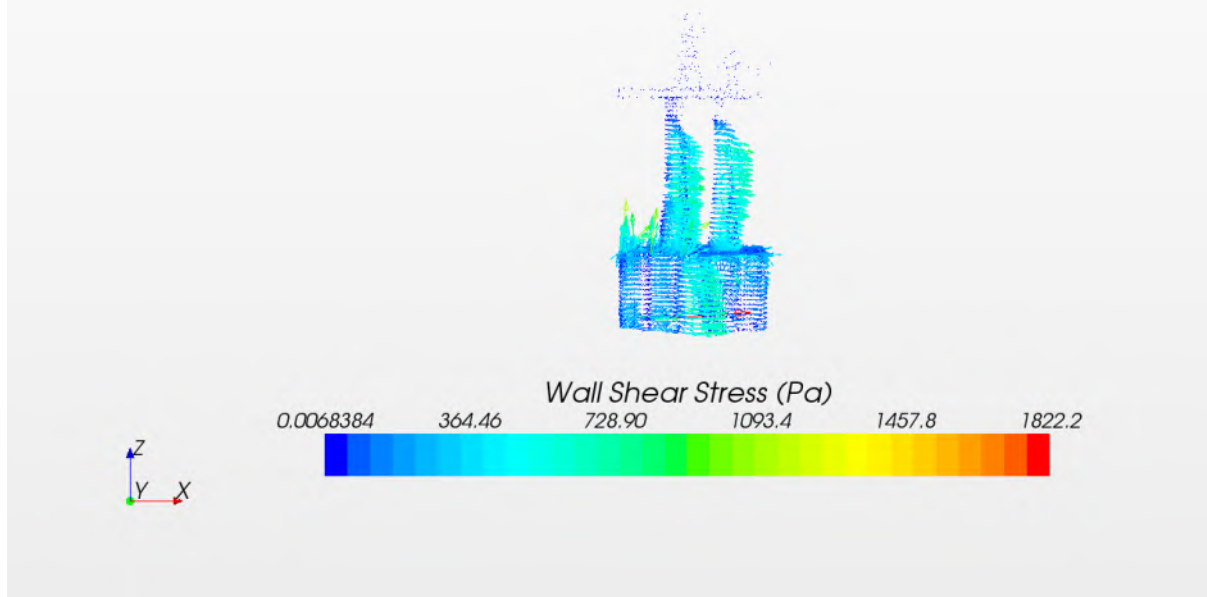


Figure69:Wall Shear Stress Results in 6th second

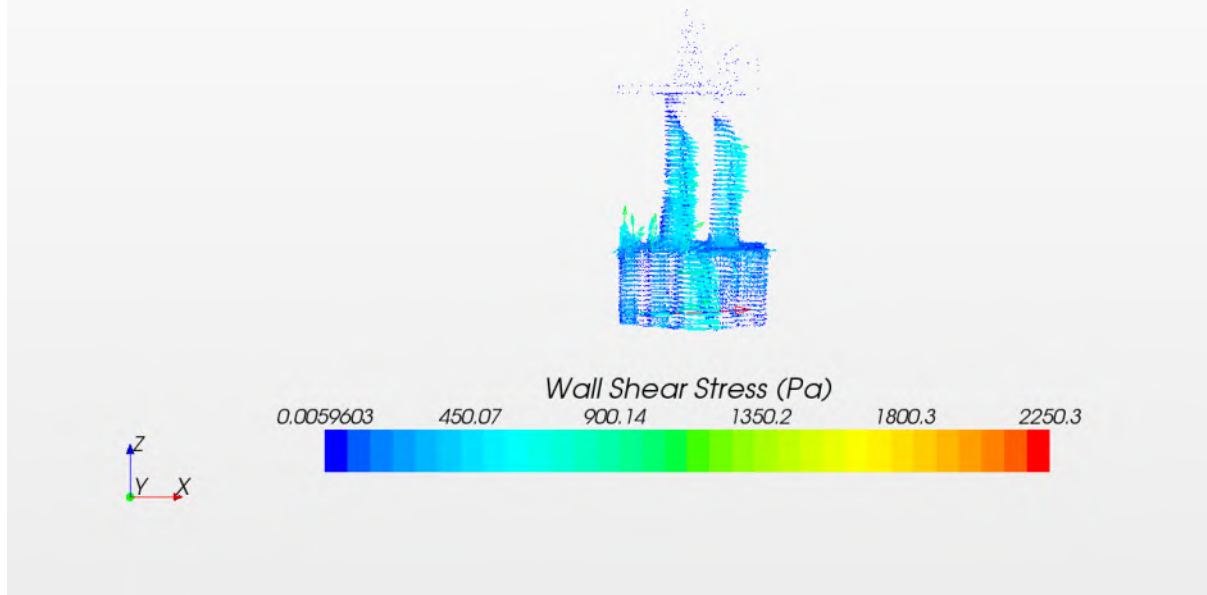


Figure70:Wall Shear Stress Results in 7th second

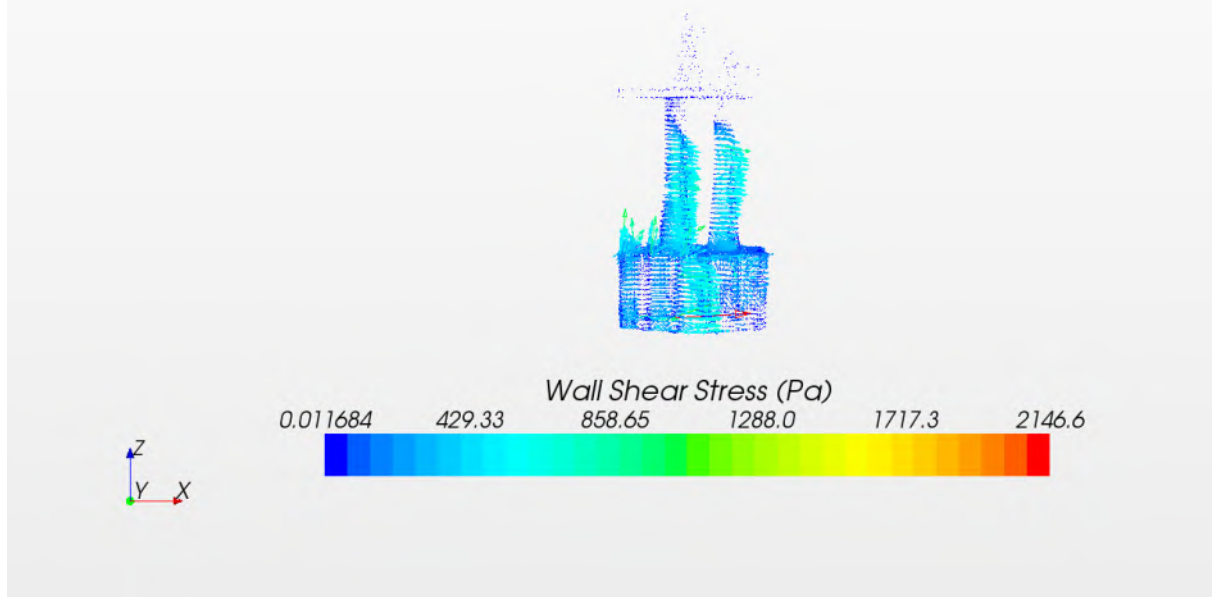


Figure71:Wall Shear Stress Results in 8th second

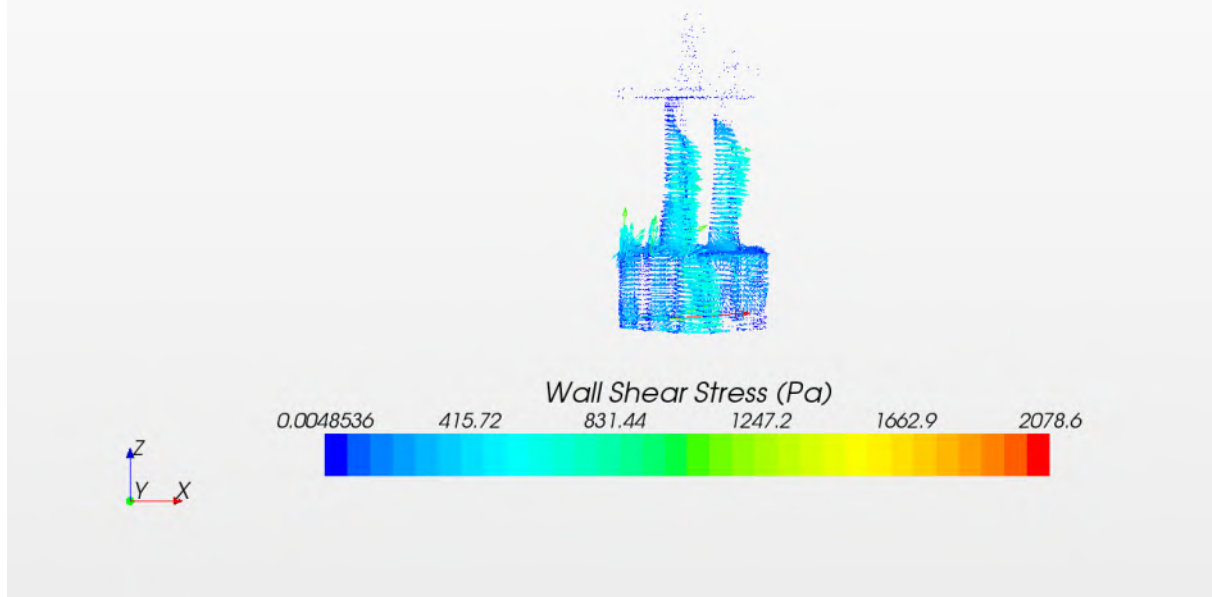


Figure72:Wall Shear Stress Results in 9th second

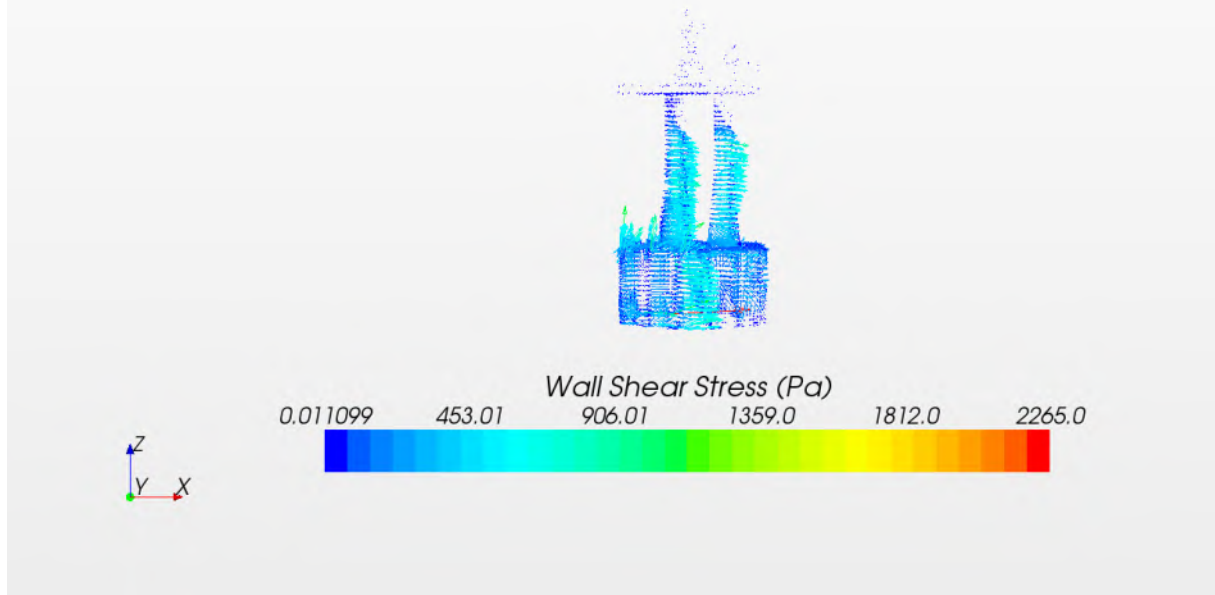


Figure73:Wall Shear Stress Results in 10th second

8. Comparing Results

8.1. Velocity

Velocity			
Time(s)	Full Model(m/s)	Symmetry Model(m/s)	Relative error %
1	30,166	30,175	0,029834913
2	30,195	30,180	0,049677099
3	30,189	30,181	0,026499718
4	30,211	30,212	0,003310053
5	30,264	30,268	0,013217024
6	30,473	30,552	0,25924589
7	31,701	31,789	0,277593767
8	32,412	32,400	0,037023325
9	31,934	31,761	0,541742344
10	31,673	31,642	0,097875162

Table2: comparison of velocity

8.2. Pressure

Pressure			
Time(s)	Full Model(E6 Pa)	Symmetry Model(E6 Pa)	Relative Error %
1	1,2792	1,2752	0,312695435
2	1,3220	1,3023	1,490166415
3	1,3263	1,3060	1,530573777
4	1,3271	1,3022	1,87627157
5	1,3296	1,3001	2,218712395
6	1,3315	1,3038	2,080360496
7	1,3350	1,3189	1,205992509
8	1,3398	1,3403	0,037319003
9	1,3412	1,3487	0,559200716
10	1,3404	1,3441	0,276037004

Table3: comparison of pressure

8.3. Wall Shear Stresses

Wall Shear Stresses			
Time	Full Model(Pa)	Symmetry Model(Pa)	Relative Error %
1	2626,9	1332,1	49,29003769
2	5413,7	1324,4	75,53613979
3	1856,6	1246,7	32,85037165
4	1180,6	997,64	15,49720481
5	1155,3	1211,8	4,890504631
6	1822,2	1523,9	16,37032159
7	2250	1185,9	47,29333333
8	2146,6	1293,4	39,74657598
9	2078,6	1295,5	37,67439623
10	2265	1044,6	53,8807947

Table4: comparison of wall shear stresses

9. Conclusion

Symmetry and Full models' gas and fluid analysis were simulated by using CFD program that is Star-CCM+.According to the these simulations, applied pressure of air and water on the platform give us these results are Wall shear stress, force, and pressure. We have compared symmetry and full models' results and it's obviously seen that there is a small difference between them.these differences are negligible.the small differences are caused by boundary conditions. Consequincely ; symmetry model is available to save you time and cost.

These results are only getting from simulation, were not experimented before. They have to be proofed in experimental. We can not trust these results. It can be only a estimation and sentiments.

10. REFERENCES

- **Tennekes, H.; Lumley, J. L. (1992).** *A first course in turbulence* (14. print. ed.). Cambridge, Mass. [u.a.]: MIT Press. ISBN 978-0-262-20019-6.
- **Hinze, J. O. (1975).** *Turbulence* (2nd ed.). McGraw-Hill. ISBN 0-07-029037-7.
- **Tennekes, H.; Lumley, J. L. (1972).** *A First Course in Turbulence*. MIT Press. ISBN 0-262-20019-8.
- **Pope, Stephen B. (2000).** *Turbulent Flows*. Cambridge University Press. ISBN 0-521-59886-9.
- **Bardina, J.E., Huang, P.G., Coakley, T.J. (1997),** "Turbulence Modeling Validation, Testing, and Development", NASA Technical Memorandum 110446.
- **Jones, W. P., and Launder, B. E. (1972),** "The Prediction of Laminarization with a Two-Equation Model of Turbulence", International Journal of Heat and Mass Transfer, vol. 15, 1972, pp. 301-314.
- **Launder, B. E., and Sharma, B. I. (1974),** "Application of the Energy Dissipation Model of Turbulence to the Calculation of Flow Near a Spinning Disc", Letters in Heat and Mass Transfer, vol. 1, no. 2, pp. 131-138.
- **Wilcox, David C (1998).** "Turbulence Modeling for CFD". Second edition. Anaheim: DCW Industries, 1998. pp. 174
- **R. S. Bisht† and A. K. Jain** Consulting Engineering Corporation, 8490 A Tyco Road, Vienna, VA 22180, U.S.A.
- <http://www.wikipedia.org/>